

THS THESIS 2 2009

LIBRARY Michigan State University

This is to certify that the thesis entitled

STABILITY OF CARBON FUSION ON ACCRETING NEUTRON STARS

presented by

PHILIPP GIRICHIDIS

has been accepted towards fulfillment of the requirements for the

M. S.	degree in	Physics and Astronomy
En	1 R	
	Major Pro	fessor's Signature
	12.11	08
		Date

MSU is an Affirmative Action/Equal Opportunity Employer

PLACE IN RETURN BOX to remove this checkout from your record. TO AVOID FINES return on or before date due. MAY BE RECALLED with earlier due date if requested.

DATE DUE	DATE DUE	DATE DUE

5/08 K:/Proj/Acc&Pres/CIRC/DateDue indd

STABILITY OF CARBON FUSION ON ACCRETING NEUTRON STARS

Ву

Philipp Girichidis

A THESIS

Submitted to
Michigan State University
in partial fulfillment of the requirements
for the degree of

MASTER OF SCIENCE

Physics and Astronomy

2008

ABSTRACT

STABILITY OF CARBON FUSION ON ACCRETING NEUTRON STARS

By

Philipp Girichidis

With observing missions like the Rossi X-ray Timing Explorer (RXTE), BeppoSAX, XMM-Newton and Chandra many thermonuclear activities on neutron stars have been observed, especially thermonuclear X-ray bursts on accreting neutron stars. Aside from frequent short type I X-ray bursts, rare and very long enduring high energetic bursts, the so-called superbursts, have been found. The large total released energy during a superburst indicates a larger ignition depth and higher ignition temperatures than it is the case for type I bursts. These ignition conditions lead to the conclusion, that unstable carbon burning triggers the thermonuclear runaway for the superburst.

This work focusses on the carbon plasma layer and its nuclear fusion stability. With numerical simulations a stability analysis of the layer has been performed, in order to find precise conditions for unstable ignitions. The numerical model used in this thesis combines a full reaction network with a complex number perturbation stability analysis, in which effects of temperature, energy flux, composition and accretion rate on the stability were examined. Furthermore, different burning regimes in the carbon burning process have been investigated in order to determine the nature of the explosion as well as the exact ignition depth. For a few sets of parameters burning oscillations were investigated. For the neutron star KS 1731-260 the stability analysis was used to determine the chemical composition of the carbon burning layer.

ACKNOWLEDGMENTS

Many Thanks to Dr. Edward Brown and Dr. Ralf Klessen for supporting my unconventional combination of an exchange year, a German diploma thesis and the MSU masters program. Dr. Brown's patience and constant availablility made it easy for me to find my way through the neutron star theory and the computational methods. I thank Dr. Klessen for his help with all the fomality concerning my stay abroad and my external diploma thesis.

Thanks to my committee members Dr. Edward Brown, Dr. Hendrik Schatz and Dr. Brian O'Shea.

Thanks to all my office mates for the very good company and for helping me with all my language questions and uncertanties.

Thanks to Debbie Barratt for helping me with all the paperwork before and during my time at the Michigan State University.

Thanks to Dr. Wolfgang Bauer for encouraging me to come to the United States and the Michigan State University.

Thanks to the Studienstiftung des deutschen Volkes for supporting me throughout my studies in Heidelberg and especially during my time at MSU.

Contents

1	Intr	oduction 1
	1.1	Neutron Stars in Binary Systems
	1.2	X-ray Bursts
	1.3	Superbursts
		1.3.1 Observations
		1.3.2 Theoretical Conclusions
	1.4	Consequences of an Unstable Ignition
	1.5	Previous Studies on Superbursts
	1.6	Goal of this Study
2	Intr	oduction to Neutron Stars 7
	2.1	General Properties
	2.2	Structure
		2.2.1 Atmosphere
		2.2.2 Ocean
		2.2.3 Crust
		2.2.4 Core
	2.3	Schematic Thermal Profile
3	Strı	acture of the Outer Layers 13
_	3.1	Accretion
	3.2	Equations of Hydrostatic Equilibrium
	3.3	Equation of State (EOS)
		3.3.1 A Polytropic Gas
		3.3.2 Numerical Fit of the EOS
		3.3.3 Coupling Parameter
	3.4	Thermodynamics
		3.4.1 Heating
		3.4.2 Cooling
	3.5	Thermal Structure Equations
4	Nuc	clear Processes 27
_	4.1	Triple- α Process
	4.2	Rapid-Proton Process (rp-process)
	4.3	Carbon Burning and Advanced Burning Stages
	4.4	Released Energy

	4.5 4.6	Electron Capture	33 34
	4.7	Electron Screening	37
5	Nui	merical Methods	41
	5.1	Basic Numerical Concepts	41
	5.2	General Properties of the Code	42
6	Ste	ady State Solution	45
•	6.1	·	45
	0.1	6.1.1 Temperature	45
		6.1.2 Flux	46
		6.1.3 Density	47
		6.1.4 Sensitivity of the Boundary Conditions	47
	6.2	Carbon Boundary Conditions	48
	6.3	Steady State Results	49
	0.0	6.3.1 Composition	49
		6.3.2 Properties of the Material	50
	6.4	Electron Capture	51
	6.5	Validating the Calculations	56
	6.6	Influence of Heavy Elements	57
	6.7	Influence of Temperature	63
		•	
7	Line	ear Stability Analysis	66
	7.1	Linear Perturbation Equations	66
	7.2	Stability and Overstability	C7
	–	Stability and Stability	67
	7.3	Application to the Stellar Model	68
	7.3	Application to the Stellar Model	68
	7.3 7.4	Application to the Stellar Model	68 69
	7.3 7.4 7.5	Application to the Stellar Model	68 69 69
	7.3 7.4 7.5 7.6	Application to the Stellar Model	68 69 69 73
	7.3 7.4 7.5 7.6	Application to the Stellar Model	68 69 69 73 75
	7.3 7.4 7.5 7.6	Application to the Stellar Model Perturbation Function Calculation Procedure Discretization and Computing Time Results of the Linear Stability Analysis 7.7.1 Stability Flux 7.7.2 Influence of heavy elements 7.7.3 Influence of the Temperature	68 69 69 73 75
	7.3 7.4 7.5 7.6	Application to the Stellar Model	68 69 69 73 75 75
	7.3 7.4 7.5 7.6	Application to the Stellar Model Perturbation Function Calculation Procedure Discretization and Computing Time Results of the Linear Stability Analysis 7.7.1 Stability Flux 7.7.2 Influence of heavy elements 7.7.3 Influence of the Temperature	68 69 69 73 75 75 76 77
	7.3 7.4 7.5 7.6 7.7	Application to the Stellar Model Perturbation Function Calculation Procedure Discretization and Computing Time Results of the Linear Stability Analysis 7.7.1 Stability Flux 7.7.2 Influence of heavy elements 7.7.3 Influence of the Temperature 7.7.4 Influence of the Accretion Rate	68 69 69 73 75 75 76 77
	7.3 7.4 7.5 7.6 7.7	Application to the Stellar Model Perturbation Function Calculation Procedure Discretization and Computing Time Results of the Linear Stability Analysis 7.7.1 Stability Flux 7.7.2 Influence of heavy elements 7.7.3 Influence of the Temperature 7.7.4 Influence of the Accretion Rate Burning Regimes	68 69 69 73 75 75 76 77 77
8	7.3 7.4 7.5 7.6 7.7	Application to the Stellar Model Perturbation Function Calculation Procedure Discretization and Computing Time Results of the Linear Stability Analysis 7.7.1 Stability Flux 7.7.2 Influence of heavy elements 7.7.3 Influence of the Temperature 7.7.4 Influence of the Accretion Rate Burning Regimes 7.8.1 Direct and Delayed Bursts 7.8.2 Overstable Modes	68 69 69 73 75 76 77 77 79 79
8	7.3 7.4 7.5 7.6 7.7	Application to the Stellar Model Perturbation Function Calculation Procedure Discretization and Computing Time Results of the Linear Stability Analysis 7.7.1 Stability Flux 7.7.2 Influence of heavy elements 7.7.3 Influence of the Temperature 7.7.4 Influence of the Accretion Rate Burning Regimes 7.8.1 Direct and Delayed Bursts 7.8.2 Overstable Modes	68 69 69 73 75 75 76 77 79 79 79
8	7.3 7.4 7.5 7.6 7.7 7.8	Application to the Stellar Model Perturbation Function Calculation Procedure Discretization and Computing Time Results of the Linear Stability Analysis 7.7.1 Stability Flux 7.7.2 Influence of heavy elements 7.7.3 Influence of the Temperature 7.7.4 Influence of the Accretion Rate Burning Regimes 7.8.1 Direct and Delayed Bursts 7.8.2 Overstable Modes Dilication Neutron stars in quiescence	68 69 69 73 75 75 76 77 79 79 79
8	7.3 7.4 7.5 7.6 7.7	Application to the Stellar Model Perturbation Function Calculation Procedure Discretization and Computing Time Results of the Linear Stability Analysis 7.7.1 Stability Flux 7.7.2 Influence of heavy elements 7.7.3 Influence of the Temperature 7.7.4 Influence of the Accretion Rate Burning Regimes 7.8.1 Direct and Delayed Bursts 7.8.2 Overstable Modes	68 69 69 73 75 75 76 77 79 79 79
8	7.3 7.4 7.5 7.6 7.7 7.8 Apr 8.1 8.2	Application to the Stellar Model Perturbation Function Calculation Procedure Discretization and Computing Time Results of the Linear Stability Analysis 7.7.1 Stability Flux 7.7.2 Influence of heavy elements 7.7.3 Influence of the Temperature 7.7.4 Influence of the Accretion Rate Burning Regimes 7.8.1 Direct and Delayed Bursts 7.8.2 Overstable Modes Dilication Neutron stars in quiescence	68 69 69 73 75 75 76 77 79 79 79

В	Column Depth	92
\mathbf{C}	Elements in the Reaction Network	94

List of Figures

2.1	Schematic structure of a neutron star	11
2.2	Schematic profile of an accreting neutron star	12
3.1	Fit functions to the EOS	20
3.2	Gravitational flux	22
3.3	Error in equation 3.39 due to an idealized specific heat	26
4.1	Sample rates for some important reactions	31
4.2	Rate Ratio of producing $p+{}^{23}\mathrm{Na}$ and ${}^{4}\mathrm{He}+{}^{20}\mathrm{Ne}$	31
4.3	Element chart of included isotopes	37
6.1	Abundances with pure accreted helium	49
6.2	Coupling parameter	50
6.3	Ignition depth for different accretion rates	51
6.4	Ignition density for different accretion rates	52
6.5	Released energy for different accretion rates	52
6.6	Thermal profile for $F_0 \frac{m_u}{\dot{m}} = 0.076 \mathrm{MeV/nuc}, T_8 = 4.0, \dot{m} = 0.2 \dot{m}_{\mathrm{Edd}}$	
	and an initial composition of 50% carbon	53
6.7	Thermal profile for $F_0 \frac{m_u}{\dot{m}} = 1.0 \mathrm{MeV/nuc}, T_8 = 4.0, \dot{m} = 0.2 \dot{m}_{\mathrm{Edd}}$	
	and an initial composition of 50% carbon	54
6.8	Energy level for electron capture on ²³ Na	56
6.9	Thermal conductivity for different compositions	58
6.10	Thermal profile for ¹² C and ¹⁶ O	59
6.11	Thermal profile for ¹² C and ⁵⁶ Fe	60
6.12	Thermal profile for ¹² C and ¹⁰⁴ Ru	61
6 13	Ignition density for different heavy elements	62

6.14	Released energy for different heavy elements	62
6.15	Ignition depth for different temperatures	64
6.16	Ignition density for different temperatures	64
6.17	Released energy for different temperatures	65
6.18	Released energy for different temperatures	65
7.1	Perturbation function	70
7.2	Example for a stable and an unstable solution for ω	72
7.3	Growth time of the perturbation	74
7.4	Influence of heavy elements on the stability	76
7.5	Influence of the temperature on the stability	77
7.6	Influence of the accretion rate on the stability	78
7.7	Direct and delayed bursts for an accretion rate of $\dot{m}=0.2\dot{m}_{\mathrm{Edd}}$ and	
	a composition of 12 C: 56 Fe = 1:1	80
7.8	Direct and delayed bursts for an a temperature of $T_8 = 4.0$ and a	
	composition of ^{12}C : $^{56}\text{Fe} = 1:1\ldots\ldots\ldots\ldots$	80
7.9	Direct and delayed bursts for an a temperature of $T_8=4.0$ and an	
	accretion rate of $\dot{m}=0.2\dot{m}_{\mathrm{Edd}}$	81
7.10	Appearance pattern of the oscillation	82
7.11	Disappearance pattern of the oscillation	83
7.12	Appearance and disappearance of the oscillation	84
8.1	Thermal profile for KS 1731-260	86
8.2	Stability flux as a function of composition for KS 1731-260	87
R 1	Relation between column depth and density	93

List of Tables

1.1	Superburst sources and properties	3
3.1	Parameters for the EOS fit function	19
4.1	Reaction types used in the nuclear network	35
C.1	List of elements	95

Chapter 1

Introduction

1.1 Neutron Stars in Binary Systems

Neutron stars have been observed in binary systems with other neutron stars, white dwarfs or non-degenerate stars. These systems can be divided into two different types: systems without mass flow and systems with mass flow from the companion star onto the neutron star. Many of the accreting neutron stars erupt in high luminous thermonuclear bursts every few hours to days. These events are known as type I X-ray bursts or simply as X-ray bursts. These flares, which have been discovered independently by Grindlay et al. [1] and Belian et al. [2], have been observed by the Rossi X-ray Timing Explorer (RXTE), the BeppoSAX, the XMM-Newton and the Chandra mission. Since the launch of BeppoSAX and RXTE in 1996, the sky has been monitored with high sensitivity and frequency in the X-ray band. This capability has opend the discovery space for bursts with longer recurrence time in the order of years, which were missed by previous missions. Cornelisse et al. [9] observed the first so-called superburst, a rare long lasting burst event with a total energy some orders of magnitude higher than in a type I X-ray burst, in the familiar type I burster 4U 1735-44.

On a neutron star with a typical mass of $1.4M_{\odot}$ and a radius of $10\,\mathrm{km}$, where the gravitaional energy per accreted baryon is $\sim 200\,\mathrm{MeV}$, it perhaps does not seem obvious that nuclear burning with a total energy release of a few MeV per nucleon plays an important role in the burst evolution and energy release. However, large amounts of unburned accumulated fuel that undergo explosive burning exceed the gravitational energy release by a lot and determine the luminosity profile of the star. What is to be determined is which nuclear reactions under what circumstances come into consideration as trigger mechanisms for these unstable ignitions. The total released energy during a burst, the recurrence time and the time evolution of these explosive events give information about the structure in the neutron stars layers below the atmoshere.

1.2 X-ray Bursts

The luminosities during a type I X-ray burst are many times larger than the persistent value of $10^{36} - 10^{38} \,\mathrm{ergs\,s^{-1}}$. Typical type I bursts exhibit rise times of several seconds, last from tens to hundreds of seconds and release a total energy of $10^{39} - 10^{40} \,\mathrm{ergs}$ (e.g. Strohmayer & Bildsten [11]). These events are caused by unstable ignition of accreted hydrogen and helium on the surface of the neutron star in constrast to type II bursts that are ignited by sudden accretion events (Lewin et al. [14]) The accumulated H/He mixture is compressed and heated in the atmosphere of the neutron star, forming a layer of layer of several meters thickness. After an hour of compression the temperture and density are high enough for the H/He to ignite and burn via the *hot* carbon-nitrogen-oxygen (CNO) cycle. If the temperature and density are high enough to trigger unstable H/He burning all the available fuel is converted to heavier elements within a few seconds which is known as the type I X-ray burst.

Source	4U 1820-30	4U1735-44	KS 1731-260
Duration [hr]	3	7	12
$L_{ m pers}\left[L_{ m Edd} ight]$	≈ 0.1	≈ 0.25	≈ 0.1
$kT_{f max}[{ m keV}]$	pprox 3	pprox 2.6	≈ 2.4
$L_{ m peak}[10^{38}{ m ergs/s}]$	3.4	1.5	1.4
$E_{ m burst}$ [$10^{38}{ m ergs}$]	> 1.4	> 0.5	≈ 1
References	S00, SB02	C00	K02
Source	4U 1636-53	Ser X-1	GX 3+1
Duration [hr]	> 2 - 3	pprox 4	> 3.3
$L_{ m pers}\left[L_{ m Edd} ight]$	≈ 0.1	pprox 0.2	pprox 0.2
$kT_{ m max}[{ m keV}]$?	≈ 2.6	~ 2
$L_{ m peak} [10^{38} { m ergs/s}]$	1.2	1.6	0.8
$E_{ m burst}$ [10 ³⁸ ergs]	0.5 - 1	≈ 0.8	> 0.6
References	W01, SM02	C02	K02

Table 1.1: Superburst sources and properties (after Kuulkers et al. [6]). Reference abbreviations: S00 (Strohmayer [4]), SB02 (Strohmayer & Brown [5]), C00 (Cornelisse et al. [3]), K02 (Kuulkers et al. [6]), W01 (Wijnands [7]), SM02 (Strohmayer & Markwardt [8]), C02 (Cornelisse et al. [9]), K02b (Kuulkers [10])

1.3 Superbursts

1.3.1 Observations

Shortly after the discovery of superbursts by Cornelisse et al. [3] six more superbursts, lasting 3-5 hours from previously known X-ray bursters have been reported: 4U 1820-30 (Strohmayer [4], Strohmayer & Brown [5]), KS 1731-260 (Kuulkers et al. [6]), 4U 1636-53 (Wijnands [7], Strohmayer & Markwardt [8]), Ser X-1 (Cornelisse et al. [9]) and GX 3+1 (Kuulkers [10]). From the neutron star 4U 1636-53 two bursts were observed, separated by a recurrence time of 4.7 years (Wijnands [7]). An overview of the superburst properties can be found in table 1.1. These flares show all hallmarks of thermonuclear explosions; they have thermal spectra which soften with time. Superbursts show a similar shape in rise and decline of the luminosity, but are roughly 1000 time more energetic and last much longer, typically several hours. The recurrence times are much longer, in the order of years, which makes

them rare events. The amount of released energies during a superburst is in the order of $10^{42} \, \mathrm{ergs} \, \mathrm{s}^{-1}$.

As neutron stars are dense objects the relatively large gravitational redshift z in comparison to other stars influences the observational measurements of temperature, luminosity and radius and can therefore not be neglected. Defining the gravitational radius as $r_g = 2GM/c^2$ the measured quantities at infinity, indicated by the ∞ subscript, are related to the actual values on the neutron stars surface as

$$L_{\infty} = L\left(1 - \frac{r_g}{R}\right),\tag{1.1}$$

$$T_{\text{eff},\infty} = T_{\text{eff}} \left(1 - \frac{r_g}{R} \right)^{1/2}, \tag{1.2}$$

$$R_{\infty} = R \left(1 - \frac{r_g}{R} \right)^{-1/2}. \tag{1.3}$$

1.3.2 Theoretical Conclusions

The similar spectral evolution and the much larger duration time and energy scales suggest that the origin of the ignition is in much larger depth and that the thermonuclear runaway is triggered by carbon burning processes. The frequent type I X-ray bursts as well as the steady state burning via the rapid proton (rp) process typically produce a significant amount of heavy ashes, so that the accumulated fuel in this deeper layer only consists of a small fraction of carbon. The ashes from former rp processes are in the range of the maximum binding energy per nucleon, so they do not undergo themonuclear reactions and therefore do not contribute to the total released energy. However, these heavy elements have much lower thermal conductivities which results in larger temperature gradients and allow the ignition of bursts with much less accumulated fuel than it would be the case for pure carbon.

1.4 Consequences of an Unstable Ignition

An unstable ignition of a parcel of hot plasma results in an immediate burning of the fuel to heavier elements, in this first step the immediate products of the reaction. Depending on the total released energy during the process and the resulting temperture of the plasma right after this nuclear conversion, further reactions of the freshly created products can be triggert and can start a nuclear runaway. Having reached the most bound state of baryons in the nuclei, the thermonuclear burning stops, which corresponds to an Iron group elements. In the case of an unstable carbon detonation the resulting upward-propagating shockwave is sufficiently strong to reach freshly accreted material and trigger unstable He burning (Weinberg & Bildsten [15]). Finally, a carbon explosion convertes all the material above the ignition layer to maximum bound nuclei like iron and even heavier material (Schatz et al. [39]).

1.5 Previous Studies on Superbursts

Many years before the first superburst was observed in 2000, unstable carbon ignition has been proposed as an explanation for the burst activities of 4U 1820-30. Following the theoretical ideas of thermonuclear instability for H/He burning by Hansen & van Horn [28], Taam & Picklum [29] extended the calculations to higher temperatures and densities which led to the conclusion of a instability in a carbon rich environment being a probable cause for the observed bursts. Due to the lack of computing power, these calculations were done with many simplifications, particularly with only a few combined reaction rates and simple instability assumptions. In a very broad study about the ocean and crust properties of accreting neutron stars Brown & Bildsten [12] included more reaction rates to their stellar evolution code, giving a detailed composition of layers below the H/He burning region. By balancing heating and cooling and calculating the effects of compression on the He burning ashes, mostly

carbon, they confirmed the previous suggestion of carbon as an igniter of superbursts and made precise predictions on the circumstances of high energetic flares. The instability criterion that was used in this and many other studies on unstable nuclear burning, e.g. nova ignition (Shen & Bildsten [32]), was, that the heating rate is greater than the cooling rate (Fujimoto et al. [31])

$$\frac{d\epsilon_{\text{nuc}}}{dT} > \frac{d\epsilon_{\text{cool}}}{dT}.$$
(1.4)

In 2003 Narayan & Heyl [25] investigated burning stabilites by studying the evolution and consequences of small perturbations applied to the burning processes and the thermal structure equations for H/He burning in the very outer layers. This perturbation calculations require complex number arithmetics which increases the computational effort by a lot and restricted their study again to a simplified reaction network. More detailed work on stability analysis, e.g. Narayan & Cooper [30], follow the perturbation method, but concentrate on type I X-ray bursts.

1.6 Goal of this Study

In this thesis the structure of the neutron star layer where unstable carbon ignition occurs as well as a detailed instability conditions for carbon burning were investigated. This was done with numerical calulations combining a full reaction network and the complex number based perturbation instability analysis. The parameter study covers the influence of the temperature, the energy flux, the accretion rate and the composition of the ignited layer on the stability of the burning process. Goal of this thesis was to find precise conditions under which a steady state shell burning switches from a stable process to an unstable explosion, resulting in a superburst. In addition to that a more detailed study on where and when in the burning process the instability occurs is determined.

Chapter 2

Introduction to Neutron Stars

2.1 General Properties

Neutron stars (NS) are very compact stars which consist in average of a large fraction of neutrons in their interior. The density in such a star exceeds several times the nuclear density. With typical masses of $1.4M_{\odot}$ and typical radii of about 10 km (Haensel [17]) neutron stars are the densest stars known. The large mass in comparison to the very small volume $(10^{-15}V_{\odot})$ results in an enormous surface gravity.

$$E_{\rm grav} \approx \frac{GM^2}{R} \approx 5 \times 10^{53} \, {\rm ergs} \approx 0.2 Mc^2$$
 (2.1)

$$g \approx \frac{GM}{R^2} \approx 2 \times 10^{14} \,\mathrm{cm} \,\mathrm{s}^{-2}$$
 (2.2)

The mean density of a typical neutron star is

$$\overline{\rho} = \frac{3M}{4\pi R^3} \approx 7 \times 10^{14} \,\mathrm{g \, cm^{-3}} \approx 2 - 3\rho_0,$$
 (2.3)

where G is the gravitational constant, c is the speed of light and ρ_0 is the mass density in heavy atomic nuclei.

2.2 Structure

The interior structure of a neutron star can be separated into four main layers: the very thin atmosphere, followed by a liquid ocean, the crust and the core. The crystalized crust below the ocean can be divided in the outer and inner crust, as well as the core which is remarkably large in comparison to other stars.

2.2.1 Atmosphere

The photosphere of a neutron star is a very thin plasma layer whose thickness varies from 10 cm in a hot neutron star with a surface temperature of 3×10^6 K down to a few millimeter in a cold neutron star with a surface temperature of 3×10^5 K. Very cold neutron stars can even have liquid or solid surfaces without a plasma atmosphere. The emitted radiation of this layer formes a spectrum of thermal electromagnetic radiation. Current models assume temperatures of $T_s \leq 10^6$ K and very strong magnetic fields ($B \geq 10^{11}$ G). This temperature is sufficiently high in order to start nuclear burning processes, so most of the accreted hydrogen is burned into helium in this outer layer of the neutron star. At the surface the flux is therefore large enough for the radiation force to exceed the very strong gravitational force which leads to a turbulent and unstable material convection and a strong plasma outflow. In hot unmagnetized stars where the radiative force is evoked by Thomson scattering the radiation force equals the gravitational force when the luminosity exceeds the Eddington limit

$$L_{\rm Edd} = 4\pi c G M m_p / \sigma_\tau \approx 1.3 \times 10^{38} \left(\frac{M}{M_s}\right) {\rm ergs \, s^{-1}}, \tag{2.4}$$

where m_p is the proton mass and σ_{τ} is the Thomson cross section. As the atmosphere is very unstable and sensitive to the neutron star's properties the actual models are not yet completed.

2.2.2 Ocean

The ocean is often defined as the region below the hydrogen and helium burning layer, where the accreted matter is decelerated from its free-fall velocity, and above the depth at which the material crystallizes. The ocean is typically $\sim 100 \,\mathrm{m}$ thick (Brown & Bildsten [12]) and ranges from densities of $10^5 - 10^9 \,\mathrm{g}\,\mathrm{cm}^{-3}$. The fully ionized plasma is liquid under these conditions (see calculations in this thesis). As the accreted matter is already decelerated, the gravitational settling and the corresponding released gravitational energy can be neglected in comparison to the much higher nuclear energy release.

2.2.3 Crust

Outer Crust The outer crust which is about several hundred meters thick consists of ions and free electrons. Its bottom is defined as the layer at which neutrons start to drip out from nuclei forming a free neutron gas at a density of $\rho \approx \rho_{\rm ND} \approx 4 \times 10^{11}\,\mathrm{g\,cm^{-3}}$. The pressure in the outer crust is mainly provided by electrons. The thin surface layer can be up to a few meters thick in hot stars and contains a non-degenerate electron gas. In deeper layers the electrons that are highly degenerate and ultrarelativistic at a densitity $\rho \gg 10^6\,\mathrm{g\,cm^{-3}}$ form an almost ideal gas. At densities larger than $10^4\,\mathrm{g\,cm^{-3}}$ the atoms are fully ionized by electron pressure. In deep layers of the crust the ions form a strong coupled Coulomb system, which can be liquid or solid. The deeper the layer the larger is the fraction of solidified matter. As the electron Fermi energy rises with growing density beta captures in the atomic nuclei occur and enrich nuclei with neutrons.

Inner Crust The inner crust spans the density range $\rho_{\rm ND} < \rho < 0.5 \rho_0$ corresponding to a thickness of about one kilometer. The matter consists of electrons, neutron rich nuclei and free neutrons with a rising fraction of free neutrons for higher densi-

9

.

ties. The neutralization processes via β -capture softens the equation of state. The deeper the layer the more important are the n-n-interactions. At the bottom layer where the density reaches values of $1/3-1/2\rho_0$ the nuclei change into a non-sperical structure and disappear at the crust core interface. In the inner crust free neutrons and nucleons that are confined in nuclei can become superfluid.

2.2.4 Core

Outer Core The outer core is several kilometers thick and extends from a density of $\approx 0.5\rho_0$ up to $\approx 2\rho_0$. The matter consists mainly of neutrons with a small fraction of protons, electrons and muons and is also called the $npe\mu$ layer. This $npe\mu$ plasma is strongly degenerate. While the electrons and muons form an almost ideal Fermi gas the neutrons and protons interact via the strong nuclear force and form a Fermi liquid which can be superfluid.

Inner Core The inner core at densities from $\rho \gtrsim 2\rho_0$ up to a central density of $\sim 4\rho_0$ has a radius of several kilopmeters and does not occurs in low-mass neutron stars. The composition and equation of state is very model dependent. Eventually strange matter condensates can be found in that layer. The main four theories of the neutron star central structure are:

- Hyperonization of matter: appearance of hyperons, mostly Σ^- and Λ hyperons
- Pion condensation: boson condensate od pion-like excitations
- Kaon condensation: BEC of Kaon-like excitations, "strange" matter
- Phase transition to quark matter, mainly u, d and s quarks with only a small admixture of electrons or even no electrons.

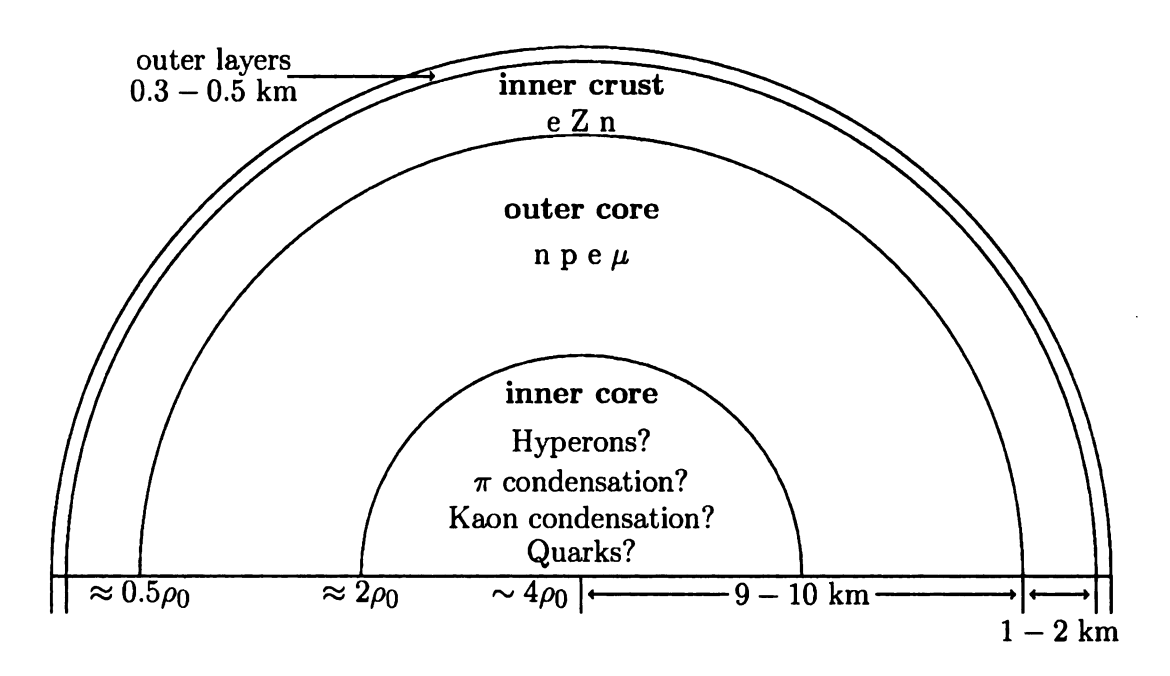


Figure 2.1: Schematic structure of a neutron star

2.3 Schematic Thermal Profile

The thermal profile of an accreting neutron star follows a characteristic scheme. An illustration of the structure can be seen in figure 2.2. Starting with a rising temperature at the outer boundary due to gravitational energy flux and nuclear burning of the accreted matter and a constant outgoing flux the temperature reaches a maximum where the energy flux switches from a net outgoing to an inward directed flux. The temperature below that layer is getting cooler and reaches a fairly cold, nearly constant core temperature. In the region where the temperature is dropping the flux value is estimated to be $F\frac{m_u}{m} \sim -0.5 \text{MeV/nuc}$ (Brown & Cumming [19]), where m_u denotes the nucleon mass and \dot{m} the accretion rate per unit area.

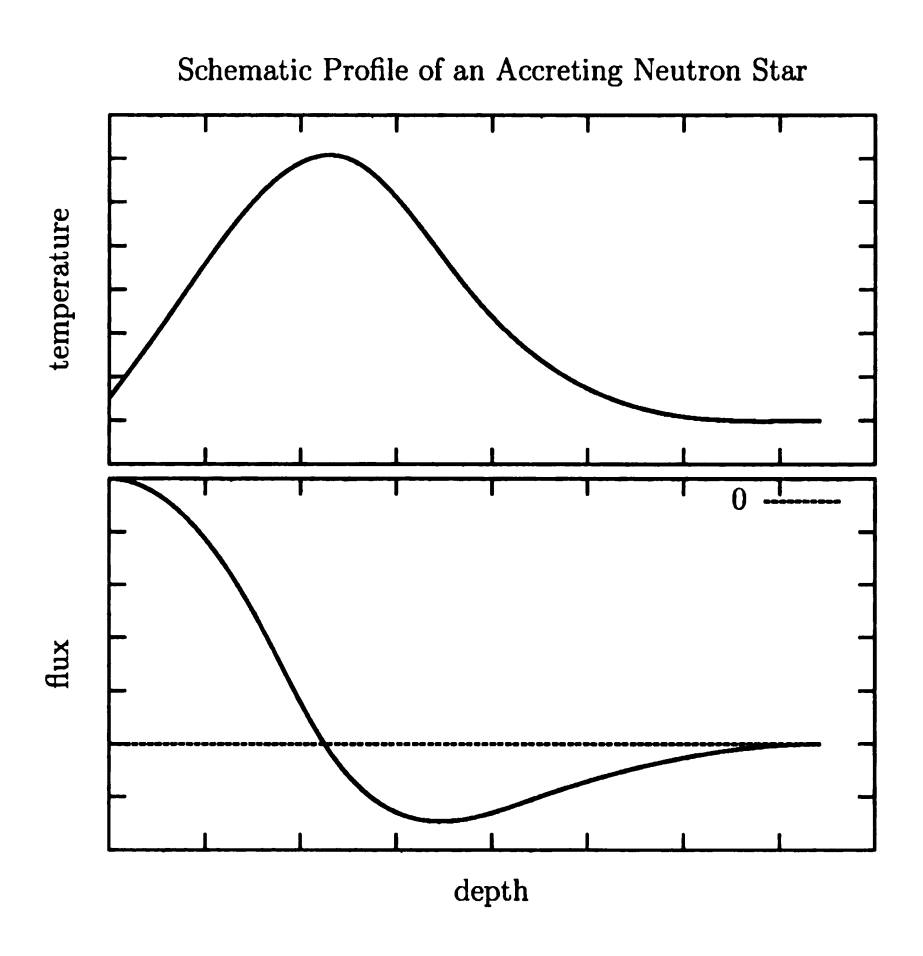


Figure 2.2: Schematic profile of an accreting neutron star

Chapter 3

Structure of the Outer Layers

3.1 Accretion

Neutron stars in binary systems can accrete material from a nearby non-compact companion star. The composition of the accreted material depends on the type of the companion, but is typically a mixture of hydrogen and helium. The amount of accreted material ranges from $10^{-10} - 10^{-8} M_{\odot}$ and results in local influx on the surface of $10^4 - 10^5 \,\mathrm{g\,cm^{-2}\,s^{-1}}$ under the assumption that the material is accreted across the entire surface area. This accretion rate is on the order of 10 - 30% of the Eddington limit $\dot{M}_{\rm Edd}$ which denotes the mass accretion rate at which the accretion luminosity is equal to the Eddington luminosity. The permanent accretion of light elements like hydrogen and helium is essential to provide a steady state composition in the outer envelope which is the basis for the investigation of carbon burning in the way it is done in this thesis. Although the accretion rate is on the order of 1/10 of the Eddington limit the total accreted mass in comparison to the neutron star's mass is fairly small. The mass impact of the material on the star can therefore be neglected which means that the assumption of hydrostatic equilibrium is still valid.

As the accretion flow onto the neutron star is in general asymmetric it is more

convenient to use the local accretion rate, defined as the mass accreted per unit area.

The local Eddington rate is defined as

$$\dot{m}_{\rm Edd} = \frac{\mu_e m_u c}{\sigma_T R} = 7.5 \times 10^4 \,\mathrm{g \, cm^{-2} \, s^{-1}} \,\mu_e \left(\frac{10 \,\mathrm{km}}{R}\right),$$
 (3.1)

where σ_T is the Thomson cross section, c is the speed of light, R is the radius of the star, m_u is the atomic mass unit and the number density of electrons is $\rho/(\mu_e m_u)$.

3.2 Equations of Hydrostatic Equilibrium

As neutron stars are very dense and massive one needs to take effects of general relativity into account. A very important coefficient is the compactness parameter r_g/R where R is the Schwarzschild radius. Typical values of the compactness parameter are very high for netron stars: 0.2 - 0.4. All other stars have values much smaller than one, i.e. white dwarfts ($\approx 10^{-4}$) or main sequance stars ($\approx 10^{-6}$). The metric that is used to describe the space around the neutron star is

$$ds^{2} = c^{2}dt^{2}e^{2\Phi} - e^{2\lambda}dr^{2} - r^{2}(d\theta^{2} + \sin^{2}\theta d\phi^{2}), \tag{3.2}$$

where t and r are the time and space coordinates, θ and ϕ are the polar and azimutal angle and Φ and λ are the curvature parameter that are described in detail below. The angular geometry with respect to θ , ϕ is the same in flat and curved space-time because of the spherical symmetry. However the space-time is curved along the time or space dimension. This space-time curvature is evoked by massive stars. For a flat space-time the curvature parameter are zero $(\Phi(r) = \lambda(r) = 0)$. For a curved space-time λ determines the curvature in radial direction which leads to a change in

length

$$l = \int_0^r e^{\lambda} dr'. \tag{3.3}$$

For many calculations it is more convenient to use the mass as a function of radius m(r) instead of the curvature parameter $\lambda(r)$. This transformation can be done with the following equation

$$e^{-\lambda} = \sqrt{1 - 2Gm/(rc^2)}, \qquad (3.4)$$

where m represents the gravitational mass inside a sphere of radius r. In neutron stars the gravitational mass is smaller than the baryon mass ("rest mass") due to the gravitational mass defect.

The parameter Φ corresponds to the time curvature and influences the proper time $d\tau=e^{\Phi(r)}dt$. It describes the gravitational redshift. Assuming a periodic signal with a frequency ν , an observer at infinity will measure a modified frequency $\nu_{\infty}=\nu(r)e^{\Phi(r)}$ or a redshift of

$$z(r) = \frac{\nu(r)}{\nu_{\infty}} - 1 = e^{-\Phi(r)} - 1. \tag{3.5}$$

Making the assumption that a neutron star's matter is a perfect fluid (all stresses are zero except for isotropic pressure), there are four functions of r that have to be solved: the two metric functions $\Phi(r)$, $\lambda(r)$, the pressure P(r) and the mass density $\rho(r)$. With the Einstein equation

$$R_{ik} - \frac{1}{2}g_{ik}R = \frac{8\pi G}{c^4}T_{ik} \tag{3.6}$$

we get three relativistic equations for hydrostatic equilibrium for a spherically sym-

metric neutron star

$$\frac{dP}{dr} = -\frac{G\rho m}{r^2} \left(1 + \frac{P}{\varepsilon} \right) \left(1 + \frac{4\pi P r^3}{mc^2} \right) \left(1 - \frac{2Gm}{c^2 r} \right)^{-1},$$

$$\frac{dm}{dr} = 4\pi r^2 \rho,$$

$$\frac{d\Phi}{dr} = -\frac{1}{\varepsilon} \frac{dP}{dr} \left(1 - \frac{P}{\varepsilon} \right)^{-1},$$
(3.7)

where the first one is the Tolman-Oppenheimer-Volkoff equation (TOV) of hydrostatic equilibrium. In order to solve these equations they have to be supplemented by an equation of state. As the first two equations do not depend on the third one, they can be solved separately. In quasi-Newtonian form the TOV can be written as

$$\frac{dP}{dr} = -g\rho, \qquad g(r) = \frac{Gm}{r^2\sqrt{1 - 2Gm/(rc^2)}},\tag{3.8}$$

where g(r) denotes the local gravitational acceleration. In the stellar interior applies $P>0,\ dP/dr<0$ with the bounardy conditions $P(r\geq R)=0,\ \rho(r\geq R)=0$ and $m(r\geq R)=M$ where M is the total gravitational mass.

As it is more convenient the column density is used as the independent parameter of the differential equations instead of the radius. The column density is defined as

$$y = \int_{r}^{\infty} \rho dr \qquad \Leftrightarrow \qquad \frac{dy}{dr} = -\rho. \tag{3.9}$$

The equations of hydrostatic equilibrium (equations. 3.7) can then be transformed to the following ones

$$\frac{dP}{dy} = \frac{Gm}{r^2} \left(1 + \frac{P}{\varepsilon} \right) \left(1 + \frac{4\pi P r^3}{mc^2} \right) \left(1 - \frac{2Gm}{c^2 r} \right)^{-1}, \tag{3.10}$$

$$\frac{dm}{dv} = -4\pi r^2,\tag{3.11}$$

$$\frac{d\Phi}{dy} = -\frac{1}{\varepsilon} \frac{dP}{dy} \left(1 - \frac{P}{\varepsilon} \right)^{-1}. \tag{3.12}$$

3.3 Equation of State (EOS)

In order to examine the interior properties of a neutron star one has to solve the equations of hydrostatic equilibrium. These have to be supported by an equation of state that relates the pressure of the material to the actual density. The basic assumption to make in order to find an EOS is local thermodynamic equilibrium (LTE). This assumption holds for a large range of the star because the particle-particle and particle-photon mean free paths are very short and the collision rates very rapid in comparison to other stellar lengths or times. Typically the LTE breaks down in the stellar atmosphere, but this layer is not of interest in this thesis. The typical length scale in which the surrounding conditions change significantly is the pressure scale height

$$\lambda_p = -\left(\frac{\partial \ln P}{\partial r}\right)^{-1} = \frac{P}{g\rho},\tag{3.13}$$

which is many orders of magnitude higher than the mean free path. With an equation of state one normally integrates starting from the center of the star to the surface. As the interior of a neutron star, espacially the EOS of the neutron star's core is not known very well, examinations of the outer envelopes, especially the ocean, start with integrations from the surface to deeper layers.

3.3.1 A Polytropic Gas

In the outer envelopes the plasma can be considered as a polytropic gas with index n. The pressure depends on the density like $P \propto \rho^{1+1/n}$. In hydrostatic balance the density can be described as a function of radius by the following equation (Brown & Bildsten [12])

$$\rho = \rho_0 \left(1 - \frac{r}{\lambda} \right)^n, \qquad \lambda = \frac{g\rho_0}{(n+1)P_0}, \tag{3.14}$$

where λ ist the total height of the polytropic atmosphere and n is the polytropic index, which is about 4/3. The constants with subscript 0 are the values for r = 0. Inserting λ in the density equation gives

$$\rho = \rho_0 \left(1 - \frac{r(n+1)P_0}{g\rho_0} \right)^n. \tag{3.15}$$

For a given minimum and maximum density (ρ_{\min} , ρ_{\max}) at the beginning and end of the ocean region the fraction P_0/ρ_0 can be calculated with

$$\frac{P_0}{\rho_0} = \frac{g\left(\left(\frac{\rho_{\text{max}}}{\rho_{\text{min}}}\right)^{1/n} - 1\right)}{(n+1)\left(\left(\frac{\rho_{\text{max}}}{\rho_{\text{min}}}\right)^{1/n} r_{\text{out}} - r_{\text{in}}\right)}$$
(3.16)

and

$$\rho_0 = \rho_{\min} \left[1 - \frac{r_{\text{out}} \left\{ \left(\frac{\rho_{\text{max}}}{\rho_{\text{min}}} \right)^{1/n} - 1 \right\}}{\left(\frac{\rho_{\text{max}}}{\rho_{\text{min}}} \right)^{1/n} r_{\text{out}} - r_{\text{in}}} \right]^{-n}, \tag{3.17}$$

where r_{out} , r_{in} are the outer and inner radius of the integration. The transformation to column depth finally yields

$$y = \int_{r}^{\infty} \rho(r')dr' = \frac{\rho_0^2 g \left(1 - \frac{(n+1)P_0 r}{g\rho_0}\right)^{n+1}}{P_0(n+1)^2}.$$
 (3.18)

3.3.2 Numerical Fit of the EOS

For stars EOSs are usually tabulated and subsequently interpolated between mesh points. But in order to do analytical calculations it is of great interest to have an analytical function for the EOS. There are several models for the EOS in deeper layers that differ slightly for high densities above $\rho = 10^{12} \,\mathrm{g \, cm^{-3}}$. As the densities

i	a_i .	i	a_i .
1	6.22	10	11.8421
2	6.121	11	-22.003
3	0.006004	12	1.5552
4	0.16345	13	9.3
5	6.50	14	14.19
6	11.8440	15	23.73
7	17.24	16	-1.508
8	1.065	17	1.79
9	6.54	18	15.13

Table 3.1: Parameters for the EOS fit function

in the carbon burning layer are much lower the differences in the EOS between these models can be neglected. For densities above $10^5 \,\mathrm{g\,cm^{-3}}$ numerical approximation with a one-parametric function works well, for lower densities that can be found in the atmosphere the EOS also depends on the temperature and therefore cannot be described as a one-parametric function any more. The fit function consists of several fractional-polynomial parts, matched together by using the function

$$f_0(x) = \frac{1}{e^x + 1}. (3.19)$$

The EOS as well as the fit function differ between rotating and non-rotating stars. All the calculations in this thesis were made with the non-rotating equations. For the EOS it is instructive to describe the pressure as a function of density. Using the two abbreviations $\xi = \log \rho$ and $\zeta = \log P$ where the density and pressure are given in g cm⁻³ and dyn cm⁻², respectively, the parameterized function is

$$\zeta = \frac{a_1 + a_2 \xi + a_3 \xi^3}{1 + a_4 \xi} f_0 \left[a_5 (\xi - a_6) \right] + (a_7 + a_8 \xi) f_0 \left[a_9 (a_{10} - \xi) \right]$$

$$+ (a_{11} + a_{12} \xi) f_0 \left[a_{13} (a_{14} - \xi) \right] + (a_{15} + a_{16} \xi) f_0 \left[a_{17} (a_{18} - \xi) \right].$$
 (3.20)

The fitting coefficients a_i can be found in table 3.1 (Haensel & Potekhin [33]).

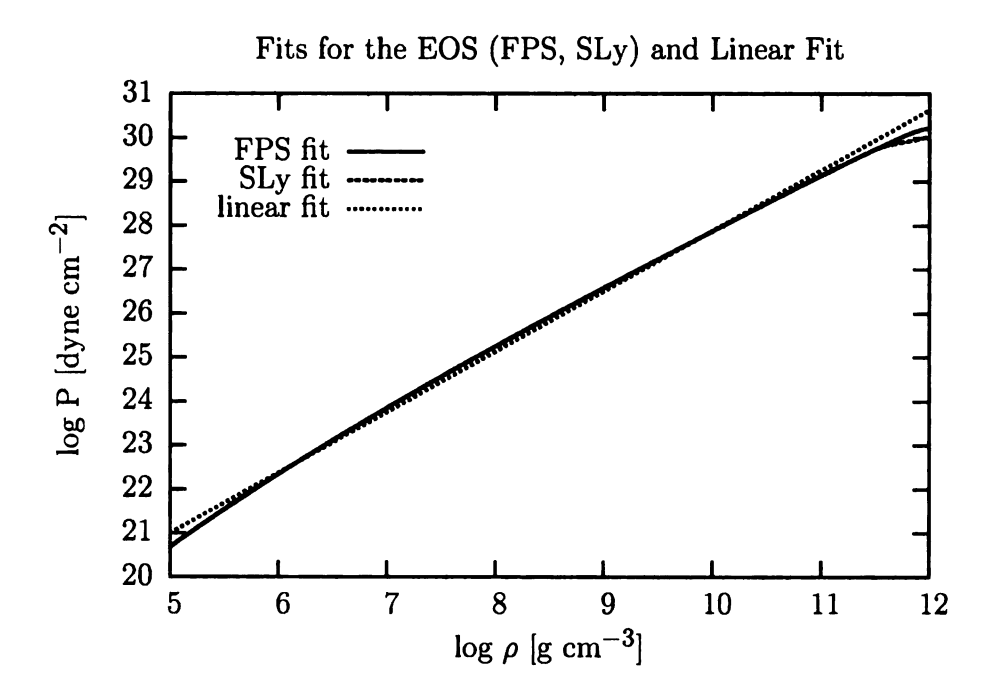


Figure 3.1: Fit functions to the EOS. The abbreviations FPS and SLy correspond to the Friedman-Pandharipande-Skyrme and the Skyrme Lyon effective interaction model (Pandharipande & Ravenhall [34] and Douchin & Haensel [35]).

As the EOS in the outer layers of a neutron star is primarily determined by degenerate electrons, the pressure can be described using a simple power law as a function of density, and the temperature dependence can be neglected. The pressure of a non-relativistic degenerate electron gas scales as $P_e \propto \rho^{5/3}$, for the relativistic case $P_e \propto \rho^{4/3}$. Including coulomb corrections the EOS can be fitted very well to the complex fit function mentioned above by the following simple power law (figure 3.1)

$$\zeta = (1.378 \pm 0.004)\xi + (14.10 \pm 0.03),$$
 (3.22)

$$P = 1.259 \times 10^{14} \,\rho^{1.378},\tag{3.23}$$

$$\rho = 5.858 \times 10^{-11} \, P^{0.7257}. \tag{3.24}$$

3.3.3 Coupling Parameter

In real gases the interactions between the particles have to be taken into account. A measure of the interaction energy between ions is the Coulomb potential between two charged particles. An ionic charge of Z for both particles separated by a distance a results in a Coulomb potential of Z^2e^2/a . Electromagnetic interactions are expected to become important when the electrostatic energy is comparable to the thermal energy kT. The ratio of electrostatic and thermal energy

$$\Gamma_C = \frac{\langle Z \rangle^2 e^2}{akT} \tag{3.25}$$

is the so-called *coupling parameter*, where $\Gamma_C=1$ is the rough demarcation at which Coulomb effects become important. The mean distance a between the ions is chosen such that

$$\frac{4}{3}\pi a^3 = \frac{1}{n_I} = \frac{\langle A \rangle}{\rho N_A},\tag{3.26}$$

where $\langle A \rangle$ denotes the mean ionic mass number and N_A is Avogadro's constant. The relation between the thermal and electrostatic energy can also be used to descibe the phase of the material. In the range of $1 \lesssim \Gamma_C \lesssim 170$ the plasma is in a liquid phase. For very low values $\Gamma_c \ll 1$ the gas can be considered as an ideal gas, values above $\sim 170-180$ cause the material to crystalize.

3.4 Thermodynamics

3.4.1 Heating

The two main heating processes in the outer layers are compressional heating due to gravitational energy of the accreted material and the energy release due to nuclear

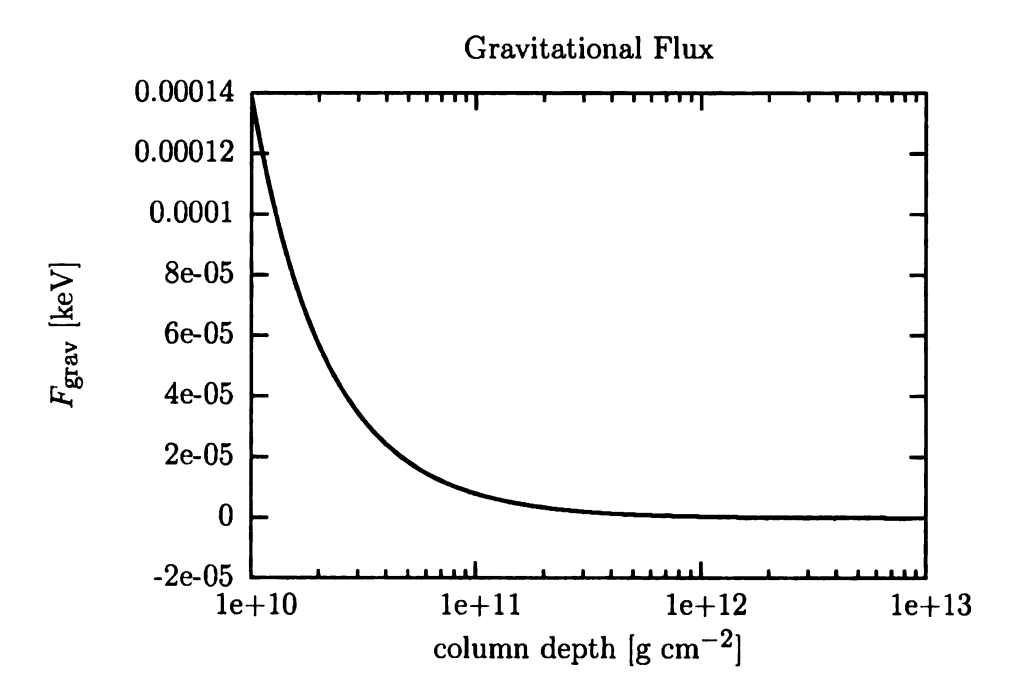


Figure 3.2: Gravitational flux

burning. With a typical radius of 10km and a mass of $1.4 M_{\odot}$ an accreted proton can release

$$\epsilon_{\rm grav} \approx \frac{GMm}{r} \approx 3 \times 10^{-4} \, {\rm ergs} \approx 200 \, {\rm MeV},$$
 (3.27)

which is much higher than the net energy relaesed in nuclear fusion from a proton to a helium nucleus (6.4 MeV per nucleon). The temperature profile of the atmosphere is therefore strongly influenced by the gravitational heating of the accreted material. However, in deeper layers where carbon ignites the contribution of the gravitational settling to the energy flux can be neglected in comparison to the nuclear burning energy of roughly 0.5 MeV/nuc (see figure 3.2).

3.4.2 Cooling

The cooling is provided by several different processes, namely the heat transport by radiation, by thermal conduction and by emission of neutrinos. The neutrino energy release at the given temperatures can be neglected and not included in the calculations.

Considering the thermal transport through the outer envelope the amount of energy taken away from this layer is determined by the energy flux **F** which obeys Fick's law and can be written as

$$\mathbf{F} = -K\nabla T,\tag{3.28}$$

where T denotes the temprature and K the thermal conductivity. Heat transport is given by both radiative (mainly Thomson scattering and free-free absorption) and conductive (electron-electron and electron-ion scattering) processes. The thermal conductivity is then

$$K = \frac{4ac}{3\rho\kappa_{\rm rad}}T^3 + K_{\rm conduction},\tag{3.29}$$

where $\kappa_{\rm rad}$ is the radiative opacity and $K_{\rm conduction}$ the electron conduction contribution.

Radiative Opacities The radiative opacities are determined by electron scattering and free-free absorption.

Conductivity The conductivity can be written as (Wiedemann-Franz law)

$$K_{\text{conduction}} = \frac{\pi^2 k_B^2 T n_e}{3m_e^* \nu_e},\tag{3.30}$$

where $m_e^* = m_e \sqrt{1 + x^2}$ is the effective mass of an electron and x is the relativistic parameter given by

$$x = \frac{p_F}{m_e c} \approx 1.009 \left(\rho_6 \frac{\langle Z \rangle}{\langle A \rangle} \right)^{1/3}. \tag{3.31}$$

 $\nu_e = \nu_{ei} + \nu_{ee}$ is the effective electron collision frequency, where the index ei denotes the electron-ion and ee the electron-electron collisions, respectively. The first one can be described (Yakovlev & Urpin [22]) by

$$\nu_{ei} = \frac{4m_e^* Z e^4}{3\pi\hbar^3} L \tag{3.32}$$

with L being the Coulomb logarithm, a slowly varying function of the density and temperature. After (Potekhin et al. [23]) the Coulomb logarithm can be calculated by

$$L = \int_0^{2k_F} dq \frac{q^3 S(q) F^2(q) R(q)}{q^4 \epsilon(q)} \left(1 - \frac{\beta^2 q}{4k_F^2} \right), \tag{3.33}$$

where $\beta = x/\sqrt{1+x^2}$, $k_F = p_F/\hbar$, $\epsilon(q)$ is the static longitudinal dielectric function of electrons, F(q) is the nuclear form factor and R(q) is a non-Born correction factor.

The effective electron-ion collision frequency can be expressed by

$$\nu_{ee} = \frac{3\beta^2}{2\alpha} \frac{(k_B T)^2}{\hbar m_e^* c^2} J(x, y). \tag{3.34}$$

 $y=\sqrt{3}T_{\rm pe}/T$, where $T_{\rm pe}=\hbar\omega_{\rm pe}/k_B$ is the plasma temperature determined by the plasma frequency $\omega_{\rm pe}=\sqrt{4\pi e^2n_e/m_e^*}$. α is the fine structure constant and again $\beta=x/\sqrt{1+x^2}$. J(y) can be calculated using the fit function by Yakovlev & Urpin [21]

$$J(x,y) \approx \left(1 + \frac{6}{5x^2} + \frac{2}{5x^4}\right) \times \tag{3.35}$$

$$\left[\frac{y^3}{3(1+0.07414y)^3}\ln\left(1+\frac{2.81}{y}\right) - \frac{0.81}{y}\frac{v_{\rm F}^2}{c^2}\right]. \tag{3.36}$$

3.5 Thermal Structure Equations

Having discussed the heating and cooling mechanisms the differential equations that allow to integrate the thermal structure of the neutron star shell can be defined. The entropy equation is given by

$$T\frac{ds}{dt} = -\frac{1}{\rho}\nabla \cdot \mathbf{F} + \epsilon,\tag{3.37}$$

where **F** is the flux and ϵ is the sum of all sources and sinks of energy. Using the equation of hydrostatic balance, the flow velocity of the accreted material $v = \dot{m}/\rho$ and the thermodynamic relation

$$\left(\frac{\partial s}{\partial P}\right)_{T} = -\left(\frac{\partial T}{\partial P}\right)_{s} \left(\frac{\partial s}{\partial T}\right)_{P} \tag{3.38}$$

equation 3.37 and the flux equation from Fick's law (3.28) can be transformed to the more useful forms

$$\frac{\partial F}{\partial y} = c_P \left(\frac{\partial T}{\partial t} + \dot{m} \frac{\partial T}{\partial y} \right) - \frac{c_P T \dot{m}}{y} \nabla_{\text{ad}} - \epsilon, \tag{3.39}$$

$$\frac{\partial T}{\partial y} = \frac{F}{\rho K}. ag{3.40}$$

Here c_P denotes the specific heat at constant pressure and

$$\nabla_{\rm ad} \equiv \left(\frac{\partial \ln T}{\partial \ln P}\right)_{s} \tag{3.41}$$

is the adiabat. The specific heat in general has contributions from the ions, the electrons and the radiation.

$$c_P = \left(\frac{\partial \epsilon}{\partial T}\right)_{\text{ions}} + \left(\frac{\partial \epsilon}{\partial T}\right)_{\text{electrons}} + \left(\frac{\partial \epsilon}{\partial T}\right)_{\text{radiation}}$$
 (3.42)

$$= \left(\frac{3N_A k}{2\langle A \rangle}\right) + \left(\frac{\pi^2 k^2}{x \, m_e c^2} \frac{N_A \langle Z \rangle T}{\langle A \rangle}\right) + \left(\frac{4aT^3}{\rho}\right),\tag{3.43}$$

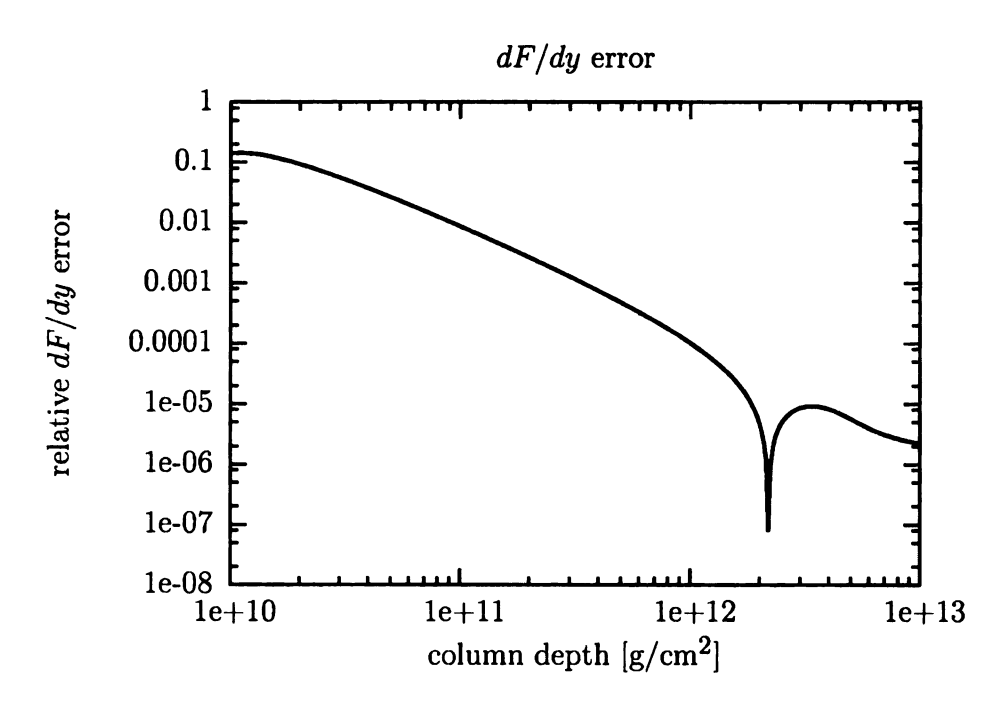


Figure 3.3: Error in equation 3.39 due to an idealized specific heat

where x is the relativity parameter $x = p_F/(mc)$. In the specific heat above an ideal gas is assumed. For the polytropic gas there are corrections that are neglected here. The internal energy of a Coulomb liquid can be fitted by the function (Hansen [37])

$$u_i = \Gamma^{3/2} \left[\frac{A_1}{\sqrt{A_2 + \Gamma}} + \frac{A_3}{1 + \Gamma} \right],$$
 (3.44)

where $A_3 = -\sqrt{3}/2 - A_1/\sqrt{A2}$, $A_2 = 0.62954$, $A_1 = -0.9070$ (Chabrier & Potekhin [36]) and Γ is the coupling parameter. The specific heat derived from that fit function differs by a factor of a few in comparison to the ideal gas specific heat. As the contribution of the terms with specific in equation 3.39 are very small relative to the released energy ϵ the relative error to dF/dy is small (see figure 3.3). The feature at a column depth of $\approx 2 \times 10^{12} \, \mathrm{g \, cm^{-2}}$ is due to an electron capture on 23 Na (see section 6.4).

Chapter 4

Nuclear Processes

4.1 Triple- α Process

In contrast to the hot CNO cycle in the triple- α process

$${}^{4}\text{He} + {}^{4}\text{He} + {}^{4}\text{He} \rightarrow {}^{12}\text{C}$$
 (4.1)

there is no lack of neutrons, so weak interactions are not needed, which accelerates the process, because the weak interaction coupling strength ($\alpha \sim 10^{-5}$) is much smaller than the coupling strength for strong interactions ($\alpha_{\rm s} \sim 1$). On the other hand helium is inhibited by the fact that there are no exothermic two-body reactions in which only ⁴He is involved. The simplest reaction would be ⁴He + ⁴He \leftrightarrow ⁸Be but the mass of ⁸Be is 92 keV higher than the mass of the ⁴He nucliei, so the ⁸Be decays with a lifetime of $\tau = 1 \times 10^{-16}\,\rm s$ back to ⁴He+⁴He. With a density of $\rho \sim 10^5\,\rm g\,cm^{-3}$ and a thermal energy of $kT \sim 10\,\rm keV$ the abundance of ⁸Be is very tiny

$$\frac{n_{\rm 8Be}}{n_{\rm 4He}} \sim 10^{-9}$$
. (4.2)

Using this small abundance it is possible to produce ¹²C through the reaction

$$^{4}\text{He} + ^{8}\text{Be} \rightarrow ^{12}\text{C} + \gamma,$$
 (4.3)

which is an exothermal reaction with a released energy of $Q=7.366\,\mathrm{MeV}$. Because of the small $^8\mathrm{Be}$ abundance the $^{12}\mathrm{C}$ production is very small. However this rate can be increased if $^{12}\mathrm{C}$ has an excited state $^{12}\mathrm{C}^*$ at a similar energy level. This excited state has an energy of 7654 keV above the $^{12}\mathrm{C}$ ground state, 283 keV above $^4\mathrm{He}+^8\mathrm{Be}$ and decays mostly via an α decay returning the original $^8\mathrm{Be}$ nucleus. Nevertheless a fraction of 10^{-3} of the $^{12}\mathrm{C}^*$ decay results in stable $^{12}\mathrm{C}$ in the ground state. The irreversible production of $^{12}\mathrm{C}$ finally proceeds through

$$3^{4}\text{He} \rightarrow {}^{4}\text{He} + {}^{8}\text{Be} \rightarrow {}^{12}\text{C}^{*} \rightarrow {}^{12}\text{C} + \gamma + \gamma.$$
 (4.4)

4.2 Rapid-Proton Process (rp-process)

For high temperatures and accretion rates at the surface of the neutron star the accreted H/He mixture does not burn in separate layers from H to He and then via the triple alpha process to carbon, but via the rapid proton process from H/He to very heavy elements beyond the iron group, $A \sim 60 - 100$ (Schatz et al. [39]). In this fusion chain the rate of capturing protons is larger than the β -decay rate, which leads to neutron poor isotopes as fusion products, located above the valey of stability in the chart of nuclei. The larger the accretion rate and the proton capture rate to the nuclei, the fewer neutrons the isotopes have in comparison to their stability valey isotope.

At high accretion rates the temperature at the ignition depth of the fuel exceeds $T \gtrsim 8 \times 10^7 \,\mathrm{K}$. The accreted material burns via the hot CNO cycle and reaches He ignition conditions before the H is fully consumed, which leads to helium fusion

in an hydrogen rich environment (Lamb & Lamb [38], Taam & Picklum [29]). For subsolar metallicities and accretion rates of $10^{-10}\,M_\odot\,\mathrm{yr}^{-1}\lesssim\dot{M}\lesssim10^{-8}\,M_\odot\,\mathrm{yr}^{-1}$ the burning is unstable and results in a type I burst. If the accretion rate is high enough for stable burning the helium is fused within 20 min. The enhancement of CNO seed nuclei combined with a so-called breakout from the CNO cycle leads to a rapid hydrogen burning via the rp-process. In that case the helium ignition acts as a trigger for rapid hydrogen burning. At an accretion rate of $m\approx\dot{m}_{\rm Edd}$ the final carbon abundance is $\approx4.1\%$ by mass (Schatz et al. [39]).

4.3 Carbon Burning and Advanced Burning Stages

After the irreversible ignition of helium to carbon the carbon burning processes can occur. The exothermic reaction

$$^{4}\text{He} + ^{12}\text{C} \rightarrow ^{16}\text{O} + \gamma, \qquad Q = 7.162 \,\text{MeV}$$
 (4.5)

competes with the triple- α process because its reaction rate is linear in the ⁴He concentration while the triple- α rate is proportional to the third power of the ⁴He concentration. The helium burning stage thus generates a mixture of ¹²C and ¹⁶O. In addition to that two more exothermic carbon burning reactions, namely

$$^{12}C + p \rightarrow ^{13}N + \gamma$$
 $Q = 1.943 \,\text{MeV}$ (4.6)

$$^{12}C + \alpha \rightarrow ^{15}O + n$$
 $Q = 7.162 \,\text{MeV}$ (4.7)

take place. The first of these two reaction rates is many orders of magnitude higher than than any helium reaction. However this reaction is strongly suppressed by the low number of available protons in the composition at that stage. The second one is very low and only comes into play at temperatures around 10⁹ K.

Although the reaction rates of the above processes cannot be neglected, in the stellar interior the triple- α can convert most of the helium to carbon before further burning branches can fuse $^{12}\text{C}+^4\text{He}$. That results in high carbon abundances before the temperature and density reaches high enough values to ignite carbon and burn it to heavier elements. The amount of produced oxygen, however is a priori not small. But the fact that at temperatures above 3.5×10^8 K the destruction rate for oxygen via

$$^{4}\text{He} + ^{16}\text{O} \rightarrow ^{20}\text{Ne} + \gamma \qquad Q = 4.73 \,\text{MeV}.$$
 (4.8)

is higher than the production rate (equation 4.7) burnes most of the produced oxygen to neon which results in a remarkable neon abundance.

A comparison of the reaction rates of the main burning processes can be found in figure (4.1). Note that these are only the reaction rates. These have to be multiplied by the abundances of the input isotopes which affects the branching ratio of the products.

As the composition resulting from nuclear burning is dominated by carbon the reactions in which only carbon is involved play an important role. The two main reactions in a carbon rich environment are

$$^{12}C + ^{12}C \rightarrow p + ^{23}Na \qquad Q = 2.242 \,\text{MeV}$$
 (4.9)

$$^{12}\text{C} + ^{12}\text{C} \rightarrow ^{4}\text{He} + ^{20}\text{Ne} \qquad Q = 4.621 \,\text{MeV}$$
 (4.10)

Comparing the reaction rates for 23 Na and 20 Ne shows that the ratio of the two rates does not vary very strongly in the temperature range of 10^8-10^9 K and is roughly one. That means that roughly for every four consumed carbon one of each p, 23 Na, 4 He and 20 Ne is produced. The ratio of both reaction rates can be seen in figure 4.2



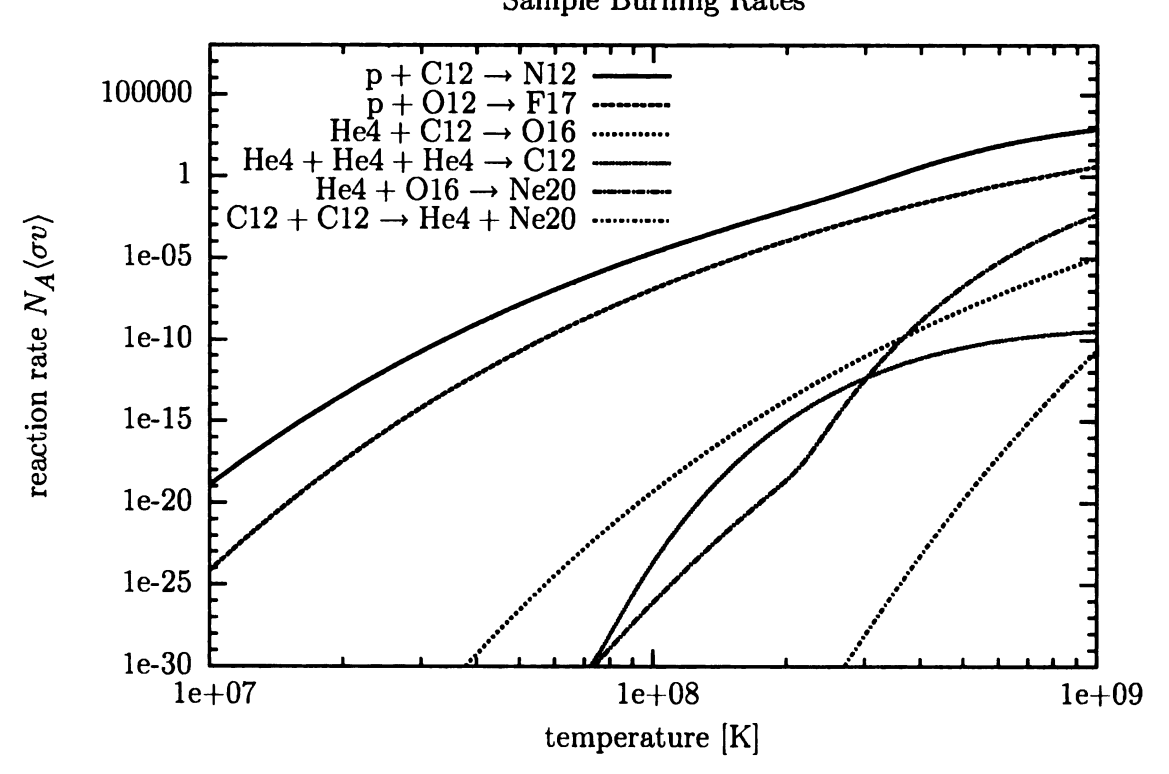


Figure 4.1: Sample rates for some important reactions

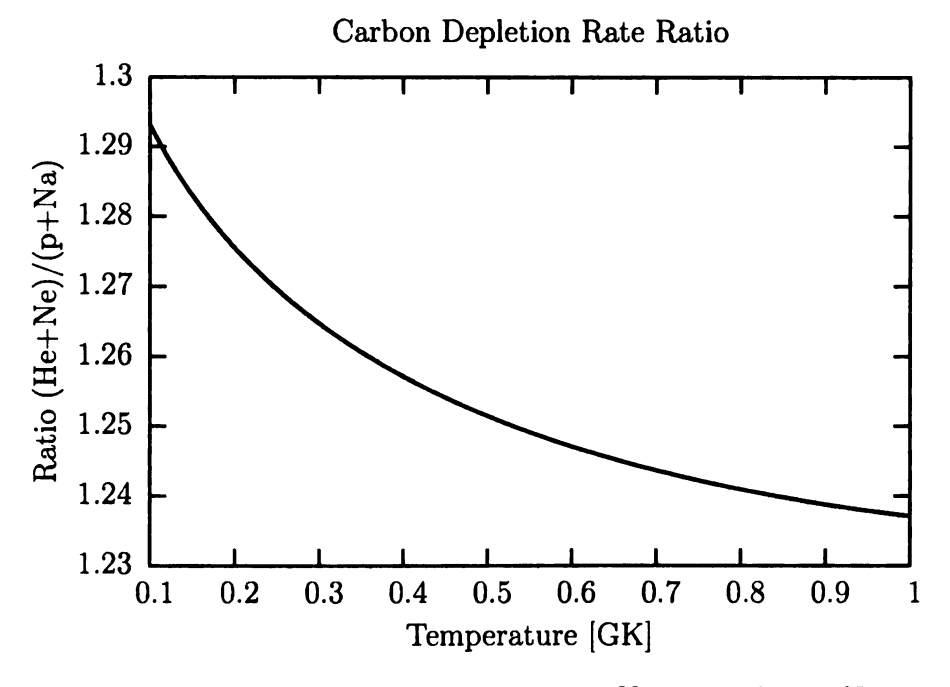


Figure 4.2: Rate Ratio of producing $p + {}^{23}\mathrm{Na}$ and ${}^{4}\mathrm{He} + {}^{20}\mathrm{Ne}$

4.4 Released Energy

The energy that is released in nuclear fusion is because of the slightly lower mass of the products relatively to the reactants. The Q value is given by

$$Q = \Delta E = \Delta mc^2. (4.11)$$

This released energy, which is due to the different binding energy of the nucleus, can be described by the Weizsäcker mass formula

$$M(Z,A) = N M_n + Z M_p + Z m_e$$
 mass of the constituents
$$-a_{\rm v}A \qquad \text{volume term}$$

$$+a_{\rm s}A^{2/3} \qquad \text{surface term}$$

$$+a_{\rm c}\frac{Z^2}{A^{1/3}} \qquad \text{Coulomb term}$$

$$+a_{\rm a}\frac{(N-Z)^2}{4A} \qquad \text{asymmetry term}$$

$$+\frac{\delta}{A^{1/2}} \qquad \text{pairing term}$$

where the coefficients a_v , a_s , a_c and a_a depend on the range of masses for which they are optimised. One possible set of parameters is (Povh [18])

$$a_{\rm v} = 15.67\,{\rm MeV} \tag{4.13}$$

$$a_{\rm s} = 17.23\,{\rm MeV}$$

$$a_{\rm c} = 0.714\,{\rm MeV}$$

$$a_{\rm a} = 93.15\,{\rm MeV}$$

$$\delta = \begin{cases} -11.2\,{\rm MeV} & \text{for even Z and N (even-even nuclei)} \\ 0\,{\rm MeV} & \text{for odd A (odd-even nuclei)} \\ +11.2\,{\rm MeV} & \text{for odd Z and N (odd-odd nuclei)}. \end{cases}$$

4.5 Electron Capture

The basic process that occurs during an electron capture to the nucleus is the inverse neutron decay

$$p + e^- \to n + \nu_e. \tag{4.14}$$

The reaction in an isolated environment is endothermal and therefore does not occur in a system with low density. However if the reacting proton is bound in a nucleus the reaction and the corresponding switch from a proton to a neutron influences the binding energy of the nucleus. The reaction

$$e^- + (Z, A) \to (Z - 1, A) + \nu_e$$
 (4.15)

can be endothermal or exothermal depending on the change in binding energy. The nuclear Q-value is the mass energy difference of the product and the reactant nucleus plus the captured electron's rest mass

$$Q = ([M(Z-1,A) - M(Z,A)] - m_e)c^2. (4.16)$$

The density at which an endothermic electron capture can occur can be obtained from the Q-value by expressing the electron chemical potential in terms of the relativistic parameter x_F

$$\mu_e = m_e c^2 \left[\left(1 + x_F^2 \right)^{1/2} - 1 \right]. \tag{4.17}$$

4.6 Reaction Network

In order to calculate the abundance changes and the released energy during the burning the set of differential rate equations have to be derived. The continuity equation

$$\partial_t n_i + \nabla \cdot (n_i v) = -d_i + p_i, \tag{4.18}$$

is determined by the destruction rates d_i and production rates p_i for each isotope i due to thermonuclear reactions. n_i is the particle density of isotope i which can be written as

$$n_i = \frac{X_i}{A_i} N_A \rho \equiv Y_i N_A \rho \tag{4.19}$$

with X_i being the mass fraction and A_i the atomic mass number. Because the number of nucleons and the density in one parcel in the star are conserved, the total particle flux in a volume dV must be 0

$$\partial_t \rho + \nabla(\rho v) = 0 \quad \Leftrightarrow \quad \sum_i X_i = 1$$
 (4.20)

with $\rho = \sum_{i} n_i A_i / N_A$. Ignoring particle diffusion, all isotopes comove $v_i = v$ and equation (4.20) can be subtracted from equation (4.18) which yields

$$\partial_t Y_i + v \cdot \nabla Y_i = \tag{4.21}$$

$$-\sum_{\mathcal{D}} \left(\rho^{p-1} N_A r(T) \prod_{k=1}^p Y_k \right) + \sum_{\mathcal{D}} \left(\rho^{p-1} N_A r(T) \prod_{k=1}^p Y_k \right). \tag{4.22}$$

For each isotope one has to sum over all the reactions that produce or destroy this isotope. The set of reactions is indicated by the index \mathcal{D} for the destruction processes and \mathcal{P} for the production processes, respectively. In each process the abundance

type	reactants		products
1	e_1	\rightarrow	e_2
2	e_1	\rightarrow	$e_2 + e_3$
3	e_1	\rightarrow	$e_2 + e_3 + e_4$
4	$e_1 + e_2$	\rightarrow	e_3
5	$e_1 + e_2$	\rightarrow	$e_3 + e_4$
6	$e_1 + e_2$	\rightarrow	$e_3 + e_4 + e_5$
7	$e_1 + e_2$	\rightarrow	$e_3 + e_4 + e_5 + e_6$
8	$e_1 + e_2 + e_3$	\rightarrow	e_4
9	$e_1 + e_2 + e_3 + e_4$	\rightarrow	e_5
10	$e_1 + e_2 + e_3 + e_4 + e_5$	\rightarrow	e_6
11	e_1	\rightarrow	$e_2 + e_3 + e_4 + e_5$

Table 4.1: Reaction types used in the nuclear network

product of the reactants has to be computed. The density appears one power less than this number. The reaction rate r(T) is only a function of temperature. Care must be taken if reactants or products appear multiple times in a reaction, i.e. ${}^4\text{He} + {}^4\text{He} + {}^4\text{He} \rightarrow {}^{12}\text{C}$, which will be discussed later in this section. The network includes the reaction types mentioned in table 4.1

In order to solve equation (4.21) it has to be linearized in time. As the system of differential equations is very stiff, an implicit integration methods has to be used, which requires the calculation of the Jacobian matrix \mathbf{J} , where $J_{ij} = \partial \dot{Y}_i/\partial Y_j$. The reaction rates are tabulated by reaction and so it makes sense to go over all the reactions and add the contribution of this reaction to the reactant and product entries in \mathbf{J} . As an example, consider a reaction of type 5: $a + b \rightarrow c + d$. This reaction makes a contribution in four abundance equations

$$\dot{Y}_{a} = \dots - Y_{a}Y_{b}\rho r(T)$$

$$\dot{Y}_{b} = \dots - Y_{a}Y_{b}\rho r(T)$$

$$\dot{Y}_{c} = \dots + Y_{a}Y_{b}\rho r(T)$$

$$\dot{Y}_{d} = \dots + Y_{a}Y_{b}\rho r(T)$$

$$(4.23)$$

and there are two factors of Y appearing on the right-hand side, so there are 8 terms in \mathbf{J}

$$J_{aa} = \dots - Y_{b}\rho r(T)$$

$$J_{ba} = \dots - Y_{b}\rho r(T)$$

$$J_{ab} = \dots - Y_{a}\rho r(T)$$

$$J_{bb} = \dots - Y_{a}\rho r(T)$$

$$J_{ca} = \dots - Y_{b}\rho r(T)$$

$$J_{cb} = \dots - Y_{a}\rho r(T)$$

$$J_{db} = \dots - Y_{a}\rho r(T)$$

$$J_{db} = \dots - Y_{a}\rho r(T)$$

in both sets of equations the ellipsis (...) indicate the contributions from other reactions.

The case of multiple reactants or products of the same isotope requires a special treatment of the reaction rate. Supposed there are N powers of one abundance on the right-hand side of the abundance time derivative. Then the reaction rate has to be devided by the statistical weight of N!. In addition to that this reaction destroys N particles of this isotope, so the rate has to be multiplied by N. This algorithm can be done easily by the following calculation procedure:

Let each rection have a number of N reactants and M poducts. Replace each reaction rate r(T) by wr(T) where w is the statistical weight. Then compute the derivatives and the Jacobian matrix without taking care of the multiplicity of the isotopes. This procedure sums up all the quantities correctly.

The reaction network includes the elements p, n, ⁴He, the isotopes shown in figure 4.3, ⁵⁶Fe and ¹⁰⁴Ru. More detailed information of the relevant element properties is listed in appendix C. The elements are connected through 68 weak and 470 strong

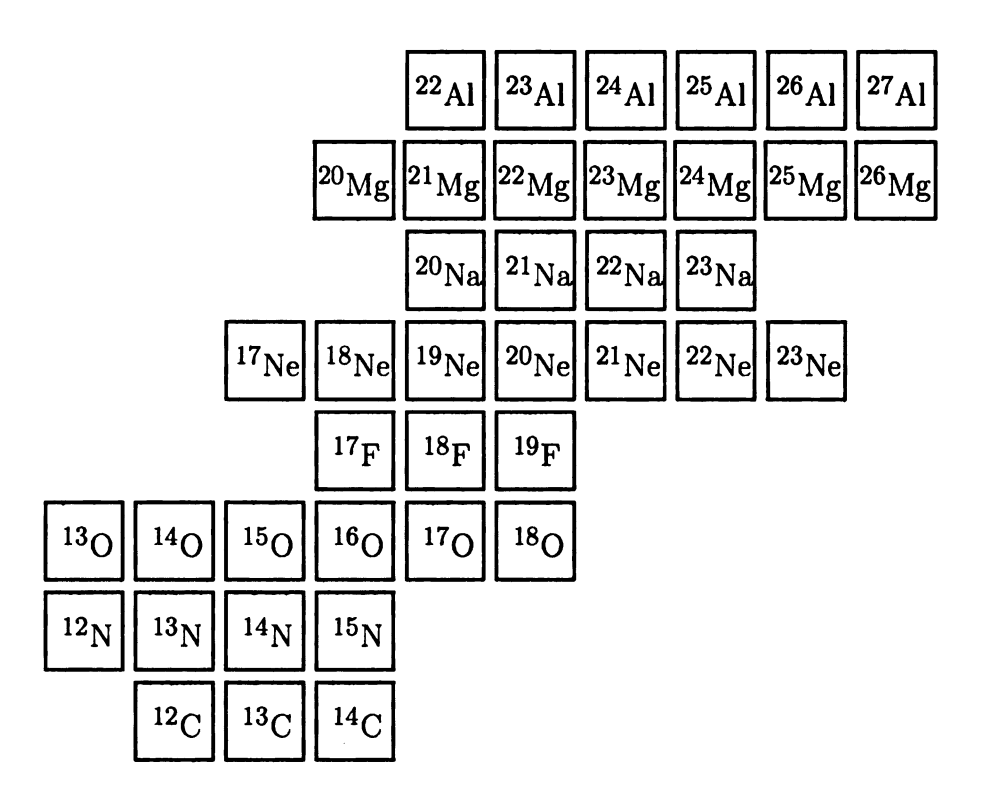


Figure 4.3: Element chart of included isotopes without p, n, ⁴He, ⁵⁶Fe and ¹⁰⁴Ru reactions, taken from the JINA reaction library (http://www.nscl.msu.edu/~nero/db/).

4.7 Electron Screening

At sufficiently high temperatures all (or practically all) of the atoms are ionized. The bare nuclei surrounded by the free electrons collide with the kinetic energy arising from the thermal motion. For the two (in some reactions even three) nuclei to undergo a nuclear transformation they have to approach each other up to a distance at which a reaction in the nucleus can take place. This distance is of the order of 10^{-13} cm, the nuclear radius. Approaching each other the repulsive Coulomb force increases strongly so that the potential energy is much larger than the thermal energy kT when the distance of the nuclei is in the order of the nuclear diameter. The important factor in the reaction is the barrier penetration factor, the probability

of the nulcei approaching sufficiently close for nuclear forces to become important.

The reaction rate r is proportional to (Salpeter [24])

$$r \propto \int_0^\infty E^{1/2} \exp\left(-\frac{E}{kT}\right) P(E) \sigma_{\text{nuc}}(E) dE.$$
 (4.25)

The first term is the Maxwell-Boltzmann distribution factor, the second (P) is the barrier penetration factor which depends strongly on the kinetic energy E and the charge of the approaching ions Z_i . σ_{nuc} is a nuclear factor which depends on the details of interaction after barrier penetration and usually varies slowly with energy.

Normally the penetration factor is calculated only with the Coulomb potential of the bare nucei with unscreened charges Z_i . In a neutron star the density is very high, the mean distance between the ions and electrons is pretty small. Even though completely ionized each ion polarizes the surrounding gas by attracting electrons and repelling neighbouring ions. The ion is then completely screened by a cloud of electrons. The radius of this cloud is in the order of the mean distance between the ions and differs depending on the ratio of the thermal energy kT and the repulsive Coulomb force. The ion takes its electron cloud with it while moving through the plasma which changes the forces and, of course, the interaction energy between two approaching ions. The total interaction energy can be written as

$$U_{\text{tot}} = \frac{Z_1 Z_2 e^2}{r_{12}} + U(r_{12}), \tag{4.26}$$

where $Z_1Z_2e^2/r_{12}$ is the unscreened Coulomb energy and $U(r_{12})$ is the screening term.

Let define E_{max} to be the energy at the classical turning point where two positive charges with kinetic energies smaller than the penetration energy have the smallest

distance:

$$E_{\text{max}} = \frac{Z_1 Z_2 e^2}{r_c}. (4.27)$$

Let furthermore a be the distance defined by the relation

$$4\pi a^3 \rho N_A = 1, (4.28)$$

where ρ is the gas density and N_A is Avogadro's number. The distance a is a measure of the interparticle distance, containing an average mass of 1/3 atomic mass units inside a sphere of radius a. Let R be the radius of the screening cloud.

Let us consider a case where the classical impact parameter r_c is much less than the the screening radius R. The barrier penetration factor mainly depends on

$$E - U(r_{12}) - \frac{Z_1 Z_2 e^2}{r_{12}}. (4.29)$$

Now $U(r_{12})$ must be a function that is small for large distances $(r_{12} \gg R)$ and becomes constant (U_0) for distances $r_{12} \ll R$. The value U_0 will be of order of $Z_1Z_2e^2/R$. From that it follows that

$$\frac{r_c}{R} \sim \frac{U_0}{E_{\text{max}}} \ll 1. \tag{4.30}$$

If this inequality is satisfied the screening potential $U(r_{12})$ can be replaced by U_0 which is independent of both E and r_{12} . Therefore the penetration factor P and the nuclear factor σ_{nuc} for energy E without screening are the same as for energy $(E + U_0)$ with screening. The reaction integral can then be replaced by

$$r_{\rm screen} \propto \int_0^\infty \left[(E + U_0)^{1/2} \exp\left(-\frac{E}{kT}\right) \exp\left(-\frac{U_0}{kT}\right) \right] P(E) \sigma_{\rm nuc}(E) dE.$$
 (4.31)

As U_0 is much smaller than $E_{\rm max}$ the term $(E+U_0)^{1/2}$ can be replaced by $E^{1/2}$ and the whole screening effect reduces to a factor $\exp(-U_0/kT)$ which the unscreened reaction rate has to be multiplied with;

$$r_{\text{screen}} = r \, \exp\left(-\frac{U_0}{kT}\right).$$
 (4.32)

Chapter 5

Numerical Methods

5.1 Basic Numerical Concepts

Concerning the stability of nuclear burning, there are two different approaches of calculation.

In one approach, one simulates the physics of the accreted material in a fully time-dependent reaction network, including a large number of different nuclear reactions and detailed thermodynamics. This kind of calculation is important for the understanding of the details of these thermonuclear explosions. A very popular example for codes like this is the FLASH program, written at Chicago. However, this method is not very convenient for parameter surveys and the comparison of theoretical predictions of bursts.

In a second approach one starts with a stellar composition in quasi-equlibrium and focuses on the thermonuclear instability that triggers the explosive burning. As the general structure of the accreted layer varies only slowly with time one first calculates a steady state solution for the composition before applying small perturbations on the system. If these perturbations grow with time, the burning process in this environment is considered to be unstable and leads in the temperature regime of a

neutron star's outer layers to a X-ray burst.

5.2 General Properties of the Code

The program that was used for this work is written in the object oriented programming language C++ and divided into two main parts. The first part is the solver for the nuclear reactions, the second part consists of the complex number based stability calculation.

The nuclear network solver is called afterburner and was written by Dr. Edward Brown. It integrates the stiff set of differential equations with an implicit Bulirsch-Stoer integrator and includes strong and weak reaction rates, as well as electron screening effects. The integrator calculates the change of the elemental abundance vector dY for a given density, temperture and burning time.

The main integration variable in all the calculation is the column depth y which is related to the burning time like

$$\frac{dy}{dt} = \dot{m} \tag{5.1}$$

for an inward moving parcel of gas in the Lagrangian coordinate system.

The second part of the program consists of two parts, the calculation procedures for the steady state solution and the complex stability analysis. Both parts integrate from outer to inner layers using the column depth as the main integration variable. The stepsize was choosen constant in logarithmic scale. The thermal structure equations do not form a set of stiff ODEs and therefore were integrated with a fixed step fourth order Runge-Kutta integrator.

The first and second part of the program are combined as follows: First the

afterburner routines determine the change of the element abundances. From that the total released energy was found by calculating total difference in mass excess of the system. With the gained energy the thermal structure including the outgoing energy flux, the temperature and the density were computed. The reason why the program was split up in these two parts is that the thermal structure equations can be changed for tests and in order to check the influence of the single terms without the need of changing the total Jacobian matrix for the implicit integrator. The following sequence shows the calculation in pseudo code:

```
for(coldepth=c0; coldepth=c1; dy)
  {
    // abundance changes
    dtime = dy/mdot
    dY = afterburner.Burn(dtime,rho,Y,T)

    // thermal structure
    dT = ...
    dF = ...
    drho = ...
    rungekutta(dT,dF,drho)
}
```

For the stability analysis the thermal structure equations are complex functions. As the perturbations applyed to the system are small the magnitude of the imaginary parts of the equations can be neglected in the abundance change calculations. The afterburner routines therefore were used with the real parts of the thermal equations.

The program first calculates the steady state solution before systematically computing the complex thermal structure for a range of complex perturbation parameters.

As input variables the program uses the temperature, the density, the inital abundances and the column depth range. The output for the steady state solution is a thermal profile as a function of column depth. The stability analysis gives the com-

plex values for temperature, density and flux at the inner boundary as output.

Chapter 6

Steady State Solution

6.1 Helium Boundary Conditions

6.1.1 Temperature

In order to find the temperature below the photospere one has to balance the net energy deposition in this layer. The outward heat flux is set by the released energy from nuclear burning below the layer and from gravitational settling. Assuming that all helium is burned to carbon the outward flux due to nuclear burning is given by

$$F_{\text{nuc}} = \frac{Q_{3\alpha}}{12m_u}\dot{m} = 0.61 \,\text{MeV}\left(\frac{\dot{m}}{m_u}\right),\tag{6.1}$$

where $Q_{3\alpha}$ is the released energy per triple- α process and \dot{m} the local accretion rate per unit area

$$\langle \dot{m} \rangle = \frac{\dot{M}}{4\pi R}.\tag{6.2}$$

With typical accretion rates of $0.1-0.3\,\dot{m}_{\rm Edd}$ the sum of the fluxes gives

$$F \sim 10^{24} \,\mathrm{ergs \, cm^{-2} \, s^{-1}}.$$
 (6.3)

The temperature can be calculated with the Stefan-Boltzmann law

$$T^4 = \frac{1}{\sigma} \left(F_{\text{grav}} + F_{\text{nuc}} \right). \tag{6.4}$$

6.1.2 Flux

As the flux value strongly influences the thermal structure of the layers below the carbon burning region, the actual value in previous studies is determined by setting inner boundary flux values and using shooting methods in order to reach the given inner constrains. Several approaches for inner boundary values have been used: Brown & Bildsten [12] set the inner flux value at the bottom of the helium burning to a range of $0.1-0.3\,\mathrm{MeV/nuc}$. Narayan & Heyl [25] integrated the stellar equations further into the stellar core, which is assumed to have a constant temperature in their calaulations, and shoot for the flux value that fulfills the desired conditions.

As the energy flux value at outer shells is set by the thermal properties like specific heat, thermal conductivity, temperature and energy release of all layers below, the exact determination of the flux requires exact models for deeper layers and precise knowledge of the central values. The energy flux therefore varies significantly with the model and the central boundaries, especially because the sum of contributions from deeper layers is large in comparison to the contribution from outer layers. The released energy during carbon burning for example is $\sim (0.3-0.4) \,\text{MeV/nuc}$, deep crustal heating in contrast releases $1.4-1.7 \,\text{MeV/nuc}$ (Haensel & Zdunik [40]). In order to avoid including all the different crust and core physics into the calculations, the outer flux value is used as a free parameter. All the quantities are therefore given for a wide flux range, which allows to switch between crust and core models and boundaries without doing the calculations for each specific constellation again.

6.1.3 Density

From an assumed coupling parameter

$$\Gamma_C = \frac{\langle Z \rangle^2 e^2}{akT} \approx 1, \qquad \frac{4}{3}\pi a^3 = \frac{\langle A \rangle}{\rho N_A}$$
 (6.5)

the following density temperature relation can be derived

$$\frac{\rho^{1/3}}{T} = \left(\frac{3\langle A \rangle}{4\pi N_A}\right) \frac{k}{\langle Z \rangle^2 e^2}.$$
 (6.6)

With pure helium and a temperature of $\sim 3 \times 10^7 \, \mathrm{K}$ the outer density is

$$\rho_0 \approx 10^5 \,\mathrm{g \, cm}^{-3}.$$
(6.7)

This surely is just a rough estimate, but as can be seen in appendix B the density and column density in the carbon burning region is very insensitive to the outer density.

6.1.4 Sensitivity of the Boundary Conditions

Before varying the outer boundary conditions it is interesting to know how sensitive the stellar structure is to these numbers. Some tests with the integrator clearly show that the system adjusts inexact values of the outer temperature and the outer density and column depth, respectively, very quickly and in any case long before the carbon burning processes come into play. In stellar physics this is also known as the radiative-zero boundary. A detailed plot of the column depth can be found in appendix B. The energy flux in contrast strongly determines the peak temperature of the stellar structure and the column depth where carbon ignites. This sensitivity supports the idea of using the flux value as a free parameter.

6.2 Carbon Boundary Conditions

From the integration through the outer layers of the star to a depth where carbon ignites one obtains a range of temperature, flux and density values that can be used for the outer carbon boundary conditions. Instead of starting the integration every time from the very outer boundary, varying these outer carbon boundary conditions and starting the integration at the maximum carbon abundance before carbon starts to burn is less time consuming and allows variations of the composition in that layer. The temperature range varies depending on the flux between

$$3 \lesssim T_8 \lesssim 6,\tag{6.8}$$

where T_8 is denotes the common abbreviation $T_8 = T/10^8 \text{K}$. The relevant integration range for the column depth was set to

$$10^{10} \,\mathrm{g \, cm^{-2}} \lesssim y \lesssim 10^{13} \,\mathrm{g \, cm^{-2}}.$$
 (6.9)

For the outer flux boundary, values in the range of

$$1 \text{ keV/nuc} \lesssim F_0 \frac{m_u}{\dot{m}} \lesssim 1 \text{ MeV/nuc}$$
 (6.10)

seem to be reasonable. The outer flux value F_0 as well as the outer temperature T in all the steady state and stability calculations is set at the outer boundary for the column depth $(y_0 = 10^{10} \,\mathrm{g \, cm^{-2}})$.

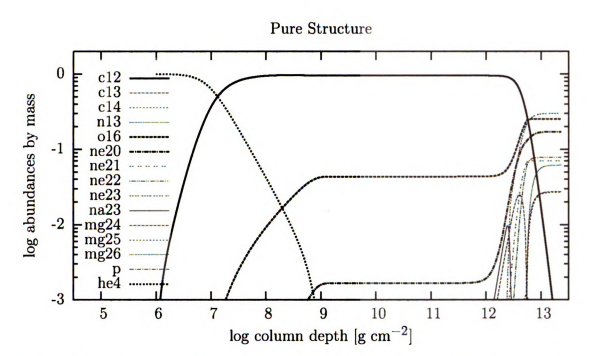


Figure 6.1: Abundances with pure accreted helium ignoring mixing with heavy ashes

6.3 Steady State Results

6.3.1 Composition

Starting with pure helium as accreted material the dominant nuclear burning process is the triple- α process which results in a very high carbon abundance of over 90% (see figure 6.1). The ¹⁶O abundance is fairly small and vaies with the initial temperature at the outer boundary. The lower the outer temperature and the resulting temperature gradient the larger is the gap between the triple- α reaction and the reaction ¹²C + ⁴He \rightarrow ¹⁶O. In this case all the available helium is already burned before the the oxygen producing reaction can ignite. In any case the fraction by mass of oxygen is smaller than 10% and can be neglected.

However, turbulent mixing in deeper layers and other heavier ashes from previous burning (bursts, rp-process) can change the composition and the maximum abundance of carbon. In this analysis the carbon abundance is also varied in order to investigate the influence of heavier elements. The ashes of bursts that are mixed

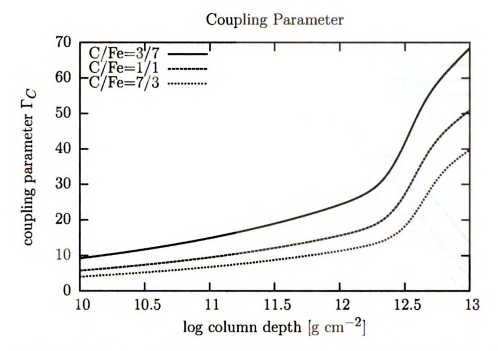


Figure 6.2: Coupling parameter for an initial temperature of 4×10^8 K and outer flux of $F_{\overline{m}}^{m} = 2.5$ MeV/nuc. The three curves correspond to different carbon abundances in the initial carbon iron mixture.

with the freshly produced 12 C are elements in the iron group with $A \approx 60$ (Woolsey et al. [26]) and elements with $A \approx 104$ (Schatz et al. [27]). The major part of the calculations is done wit a mixture of iron and carbon in varying fractions.

6.3.2 Properties of the Material

The phase of the burning material can be determined with the coupling parameter

$$\Gamma_C = \frac{\langle Z \rangle^2 e^2}{kT} \left(\frac{4\pi \rho N_A}{3\langle A \rangle} \right)^{1/3}, \qquad (6.11)$$

which can be derived from equations 3.25 and 3.26. The coupling parameter for an initial mixture of iron and carbon, an outer temperature of $T=4\times 10^8\,\mathrm{K}$ and flux value of $F_0\frac{m_u}{m}=0.25\,\mathrm{MeV/nuc}$ can be seen in figure 6.2. The values for Γ_C indicate that the material is in the liquid phase over the entire burning range. The rise at higher column depth is due to the freshly produced heavier elements with $Z\approx 10$

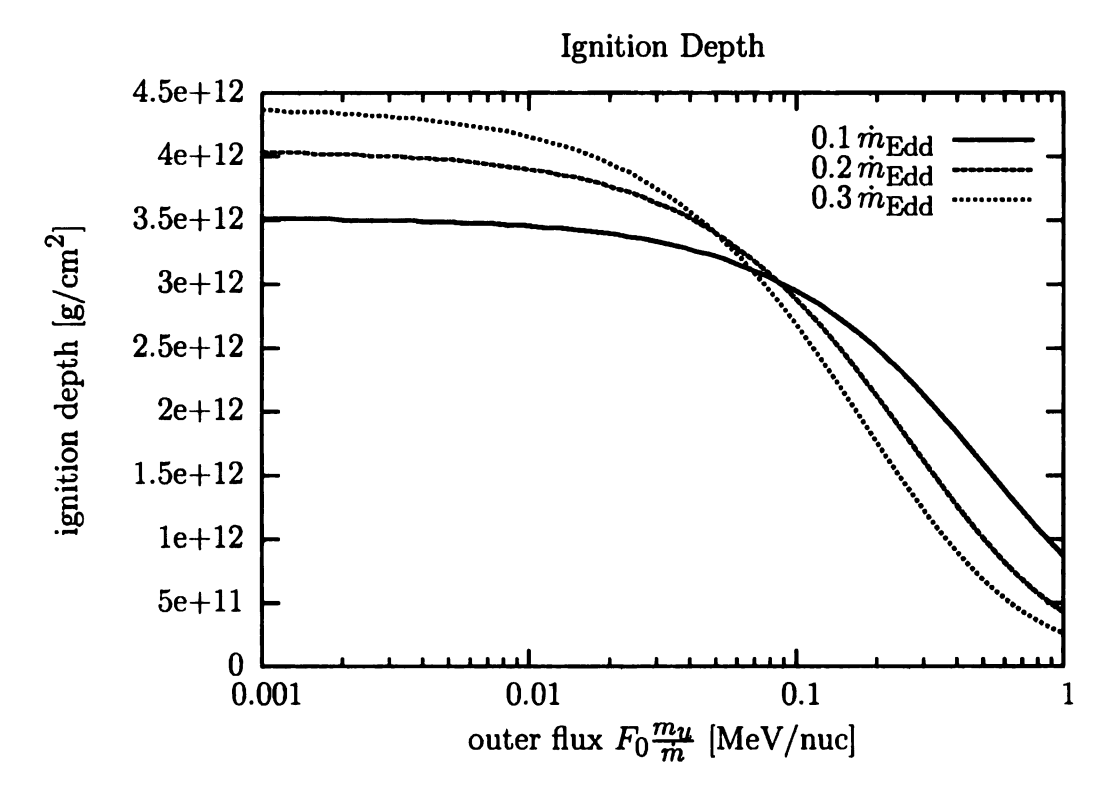


Figure 6.3: Ignition depth for different accretion rates

which increses the electrostatic energy.

6.4 Electron Capture

The ignition depth, the corresponding density and the released energy per nucleon for carbon fusion as a function of outer flux for an initial composition of each 50% 12 C and 56 Fe and an outer temperature of $T_8 = 4.0$ can be seen in figures 6.3, 6.4 and 6.5. The released energy clearly shows a strong increase for flux values above $\sim 0.2 \,\mathrm{MeV/nuc}$ which corresponds to an ignition density of roughly $1.7 \times 10^9 \,\mathrm{g\,cm^{-3}}$. A closer look at the composition as function of density shows, that at this density the main product from carbon burning switches from 23 Ne at higher ignition densities to 20 Ne at lower densities (see figures 6.6 and 6.7). This change is due to an electron capture to 23 Na.

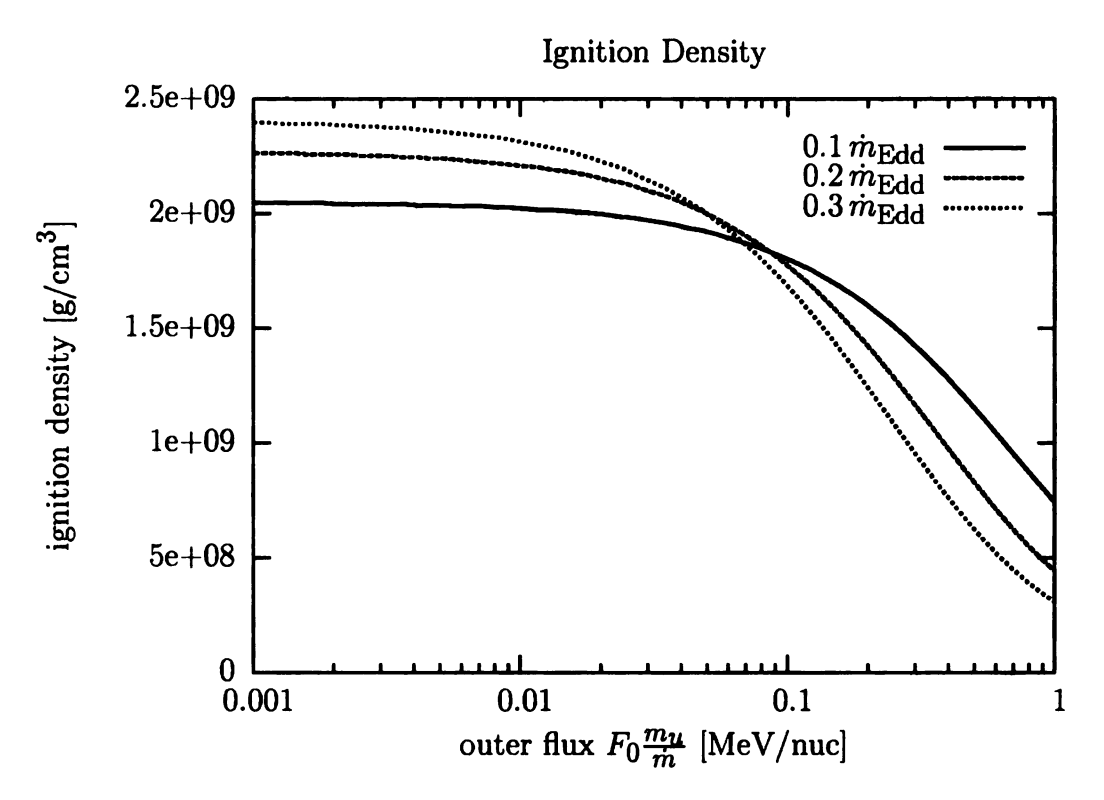


Figure 6.4: Ignition density for different accretion rates

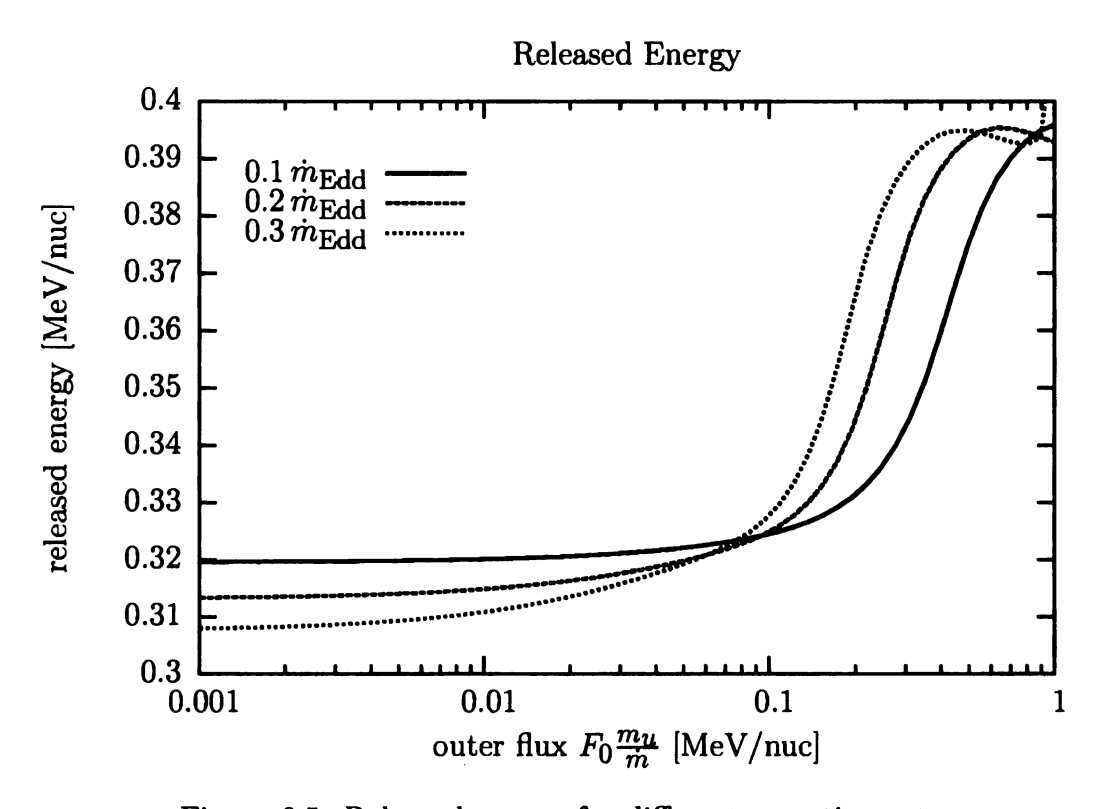


Figure 6.5: Released energy for different accretion rates

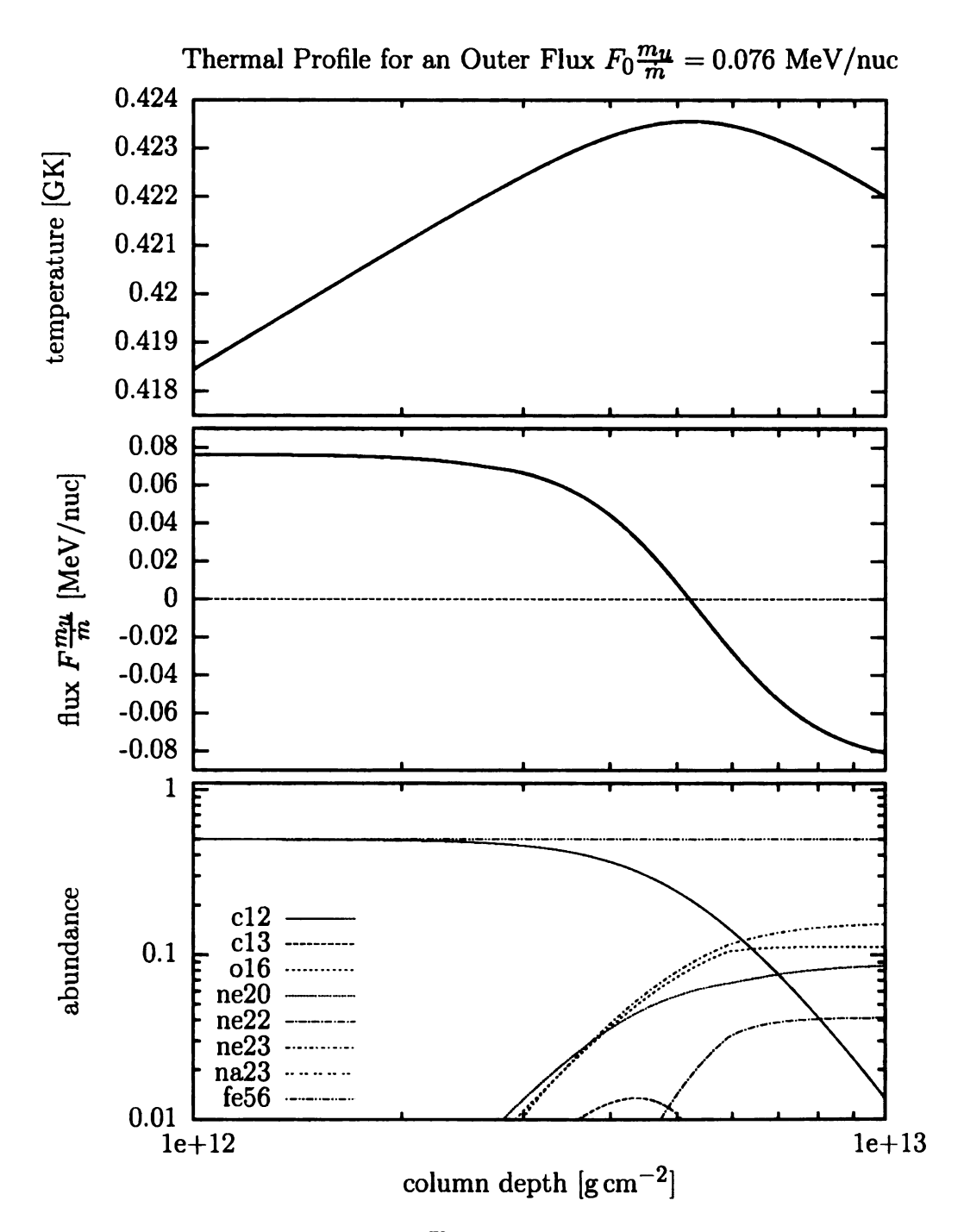


Figure 6.6: Thermal profile for $F_0 \frac{m_u}{\dot{m}} = 0.076\,\mathrm{MeV/nuc},\ T_8 = 4.0,\ \dot{m} = 0.2\,\dot{m}_\mathrm{Edd}$ and an initial composition of 50% carbon

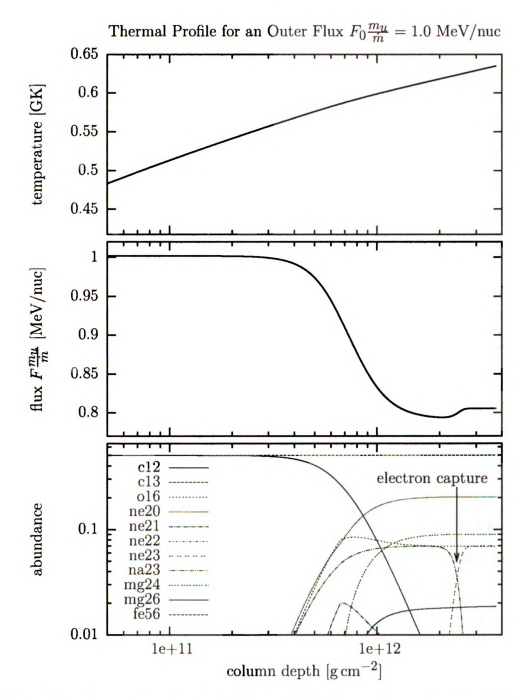


Figure 6.7: Thermal profile for $F_0\frac{m_u}{m}=1.0\,{\rm MeV/nuc},\,T_8=4.0,\,\dot{m}=0.2\,\dot{m}_{\rm Edd}$ and an initial composition of 50% carbon

In a carbon rich environment the two main processes are

$$^{12}C + ^{12}C \rightarrow p + ^{23}Na$$
 (6.12)

$$^{12}C + ^{12}C \rightarrow ^{4}He + ^{20}Ne.$$
 (6.13)

As mentioned in section 4.3 the ratio of these two reactions does not vary strongly in the temperature range between $10^8 - 10^9$ K and has a value of $(^4\text{He} + ^{20}\text{Ne})/(p + ^{23}\text{Na}) \approx 1.2$, which results in almost equal parts of produced p, ^{23}Na , ^4He and ^{20}Ne .

For lower ignition densities the most important following reaction is

23
Na + $p \to ^{4}$ He + 20 Ne. (6.14)

²⁰Ne is pretty stable at the given environment and has insignificant burning rates which explaines the high abundance at the end of the carbon burning process (see figure 6.7). At higher ignition densities the reaction rate for an electron capture on ²³Na

$$^{23}\text{Na} + e \rightarrow ^{23}\text{Ne} + \overline{\nu}_e \tag{6.15}$$

is much larger than the rate for 23 Na + $p \rightarrow ^{4}$ He + 20 Ne which turnes a high fraction of 23 Na into 23 Ne, which itself is also pretty stable at this temperture range. This finally results in an 23 Ne rich environment (see figure 6.6).

The threshold density at which the electron capture becomes important can be calculated as follows: The mass difference between 23 Ne and 23 Na is 4.887 MeV. Subtracting the captured electron's restmass of 511 keV yields an energy difference of $\mu_e = 4.376$ MeV (see figure 6.8). From the the electron chemical potential and the relativistic parameter the density in an environment with $\langle Z \rangle / \langle A \rangle = 0.5$ finally yields $\rho = 1.675 \times 10^9$ g cm⁻³ for the electron capture on 23 Na, which corresponds to

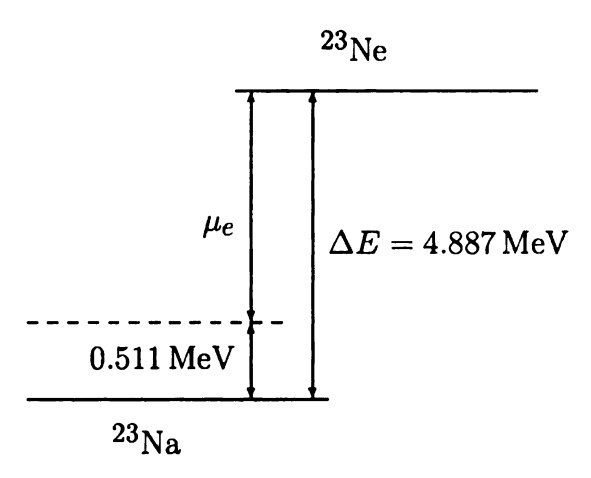


Figure 6.8: Energy level for electron capture on ²³Na

a column depth of $y=2.75\times 10^{12}\,\mathrm{g\,cm^{-2}}$ and fits exactly with the burning results (see figure 6.7).

6.5 Validating the Calculations

In order to validate the computed structure, especially the column depth and the total released energy during a superburst, the important quantity is the ignition depth. In a superburst all the material above the ignited layer is burned to heavy elements (Weinberg & Bildsten [15]), that do not contribute to further nuclear fusion.

Assuming that most of the accreted hydrogen is burned quickly to helium, the layers above the carbon burning consist of a mixture of carbon and helium. Depending on the fracation of heavy ashes the amount of burnable fuel shrinks. For a rough estimate equal parts of burnable fuel and inactive ashes are chosen, the fuel consisting mostly of carbon. The released energy per nucleon is then given by the difference in the binding energy:

$$\epsilon = \frac{1}{2} \left\{ \frac{B(^{56}\text{Fe})}{56} - \frac{B(^{12}\text{C})}{12} \right\}$$
 (6.16)

$$= \frac{1}{2} \{8.790 \,\text{MeV/nuc} - 7.680 \,\text{MeV/nuc}\} \tag{6.17}$$

$$= 0.555 \,\text{MeV/nuc.}$$
 (6.18)

The total mass above the ignition layer is simply given by the column depth. In the nuclear calculations the layer above the ignited carbon has a mass of a few $10^{12}\,\mathrm{g\,cm^{-2}}$, which gives a number of 10^{36} nucleons per square centimeter surface area. With a radius of 10 km the total released energy is $\sim 10^{42}\,\mathrm{ergs}$, which matches the values of former theoretical work and observations.

Estimating the recurrence time by assuming that at constant accretion rate the neutron star has to accumulate the same amount of material $(10^{12} \,\mathrm{g\,cm^{-2}})$, this time can be written as

$$t_{\rm rec} = \frac{y_{\rm ignition}}{\dot{m}}. ag{6.19}$$

With an accretion rate of $\dot{m}/\dot{m}_{\rm Edd} \approx 0.2$ the recurrence time is in the order of $t_{\rm rec} \approx 2\,{\rm yr}$.

6.6 Influence of Heavy Elements

As mentioned before mixing between different layers and heavy ashes from previous explosions can enrich the carbon burning layer with $A \gtrsim 60$ elements that do not take part in nuclear fusion any more. However these elements influence the thermal quantities like the specific heat and the thermal conductivity in the layer. Especially the thermal conductivity, which is much lower for heavier elements causes the ignition front to move farther out due to the more insulating character of the plasma. The thermal conductivities for layers composed of 50% carbon and 50% heavier elements (16 O, 56 Fe, 104 Ru) are plotted in figure 6.9. At a column depth of $y \sim 10^{12}\,\mathrm{g\,cm^{-2}}$ the carbon ignites. The resulting influence of the heavier reaction products on the conductivity is significant for the carbon-oxygen composition. Mixtures of carbon and iron or ruthenium do not show a remarkable change in the conductivity below the carbon burning depth. Full thermal profiles for the same compositions are shown

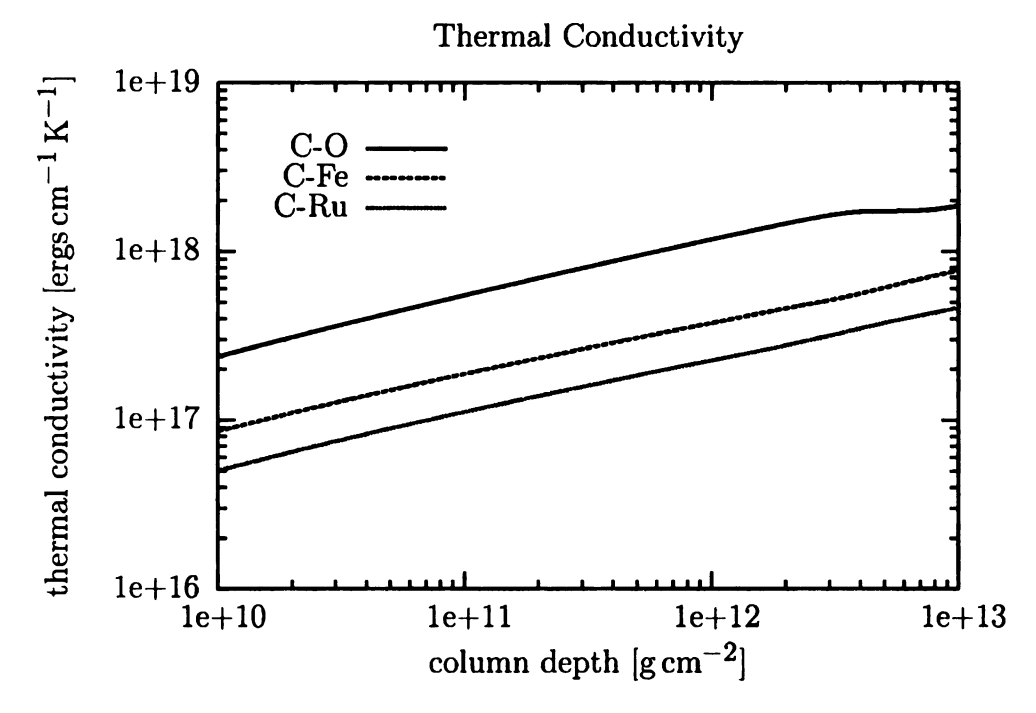


Figure 6.9: Thermal conductivity for an initial abundance of each 50% of $^{12}{\rm C}+^{16}{\rm O},$ $^{12}{\rm C}+^{56}{\rm Fe}$ and $^{12}{\rm C}+^{104}{\rm Ru}$

in figures 6.10, 6.11 and 6.12. All three profiles were computed with an outer temperature of $T_8 = 4.0$, an outer flux of $F_0 \frac{m_u}{\dot{m}} = 0.15 \,\text{MeV/nuc}$ and an accretion rate of $\dot{m} = 0.2 \, \dot{m}_{\text{Edd}}$. Figures 6.13 and 6.14 show the ignition density and the released energy for different compositions. The temperature at the outer boundary was set to $T_8 = 4.0$, the accretion rate again to $\dot{m} = 0.2 \, \dot{m}_{\text{Edd}}$.

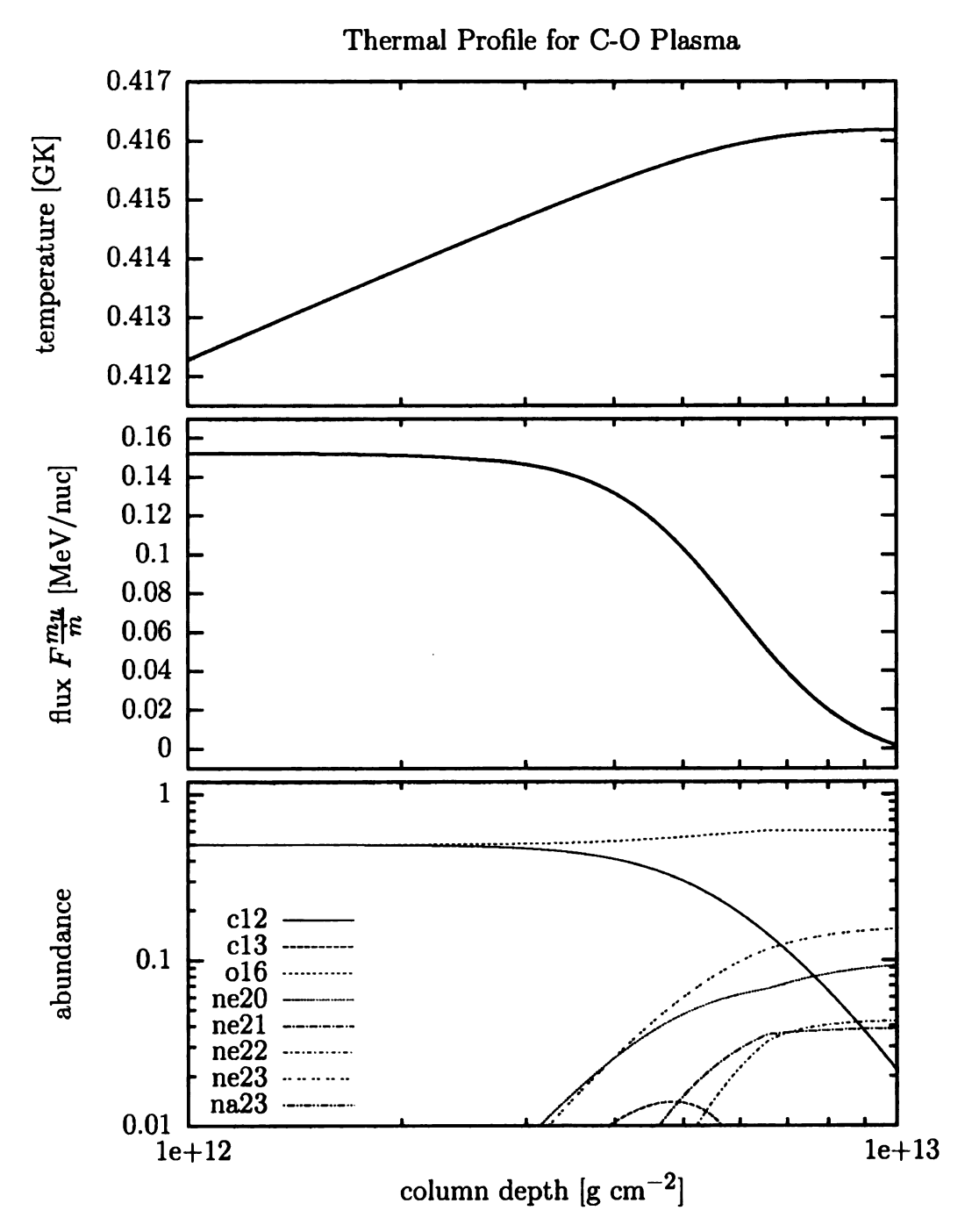


Figure 6.10: Thermal profile for an initial abundance of each 50% of 12 C and 16 O, an outer flux $F_0 \frac{m_u}{\dot{m}} = 0.15\,\mathrm{MeV/nuc}$ and an accretion rate of $\dot{m} = 0.2\,\dot{m}_\mathrm{Edd}$

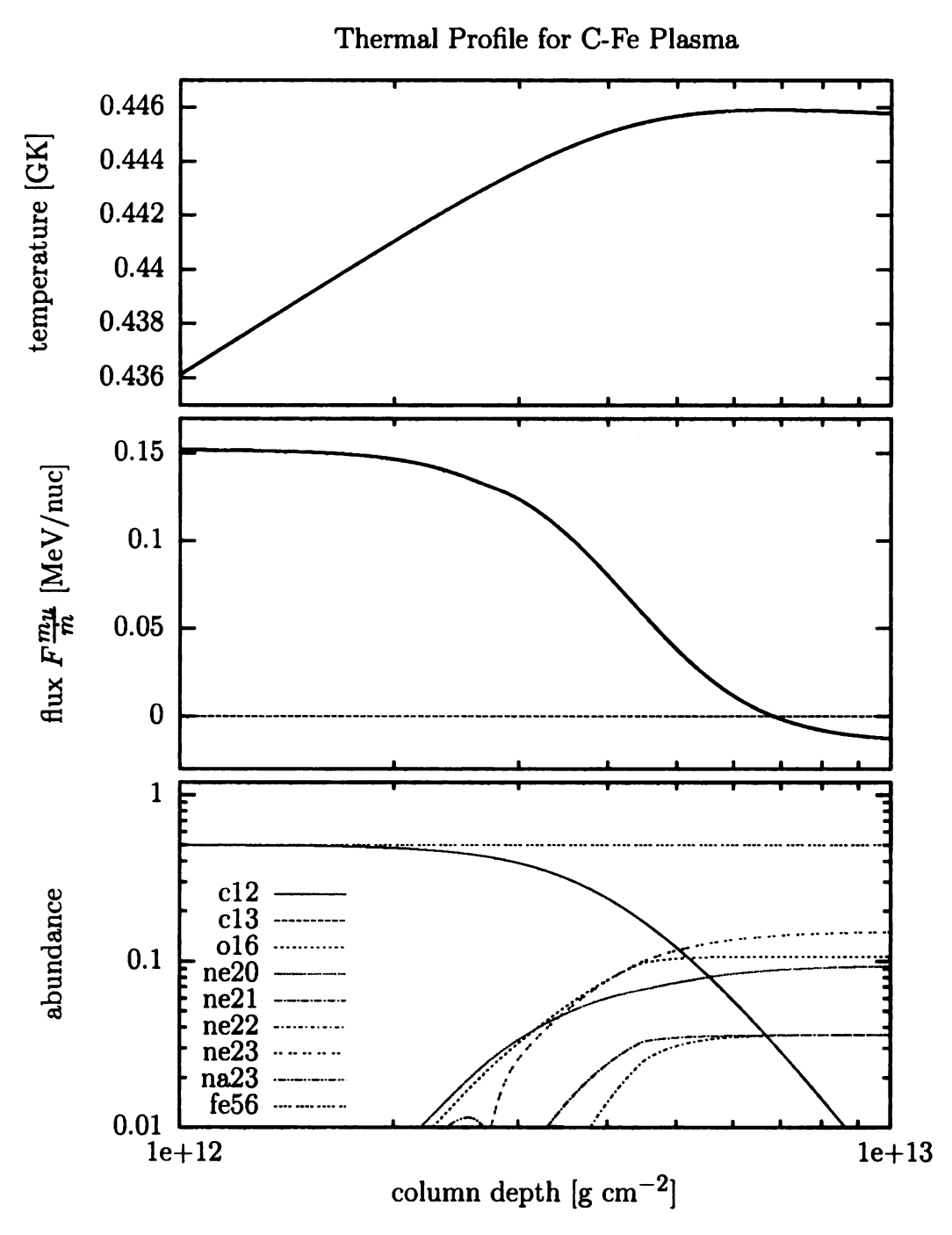


Figure 6.11: Thermal profile for an initial abundance of each 50% of $^{12}\mathrm{C}$ and $^{56}\mathrm{Fe}$, an outer flux $F_0\frac{m_u}{\dot{m}}=0.15\,\mathrm{MeV/nuc}$ and an accretion rate of $\dot{m}=0.2\,\dot{m}_\mathrm{Edd}$

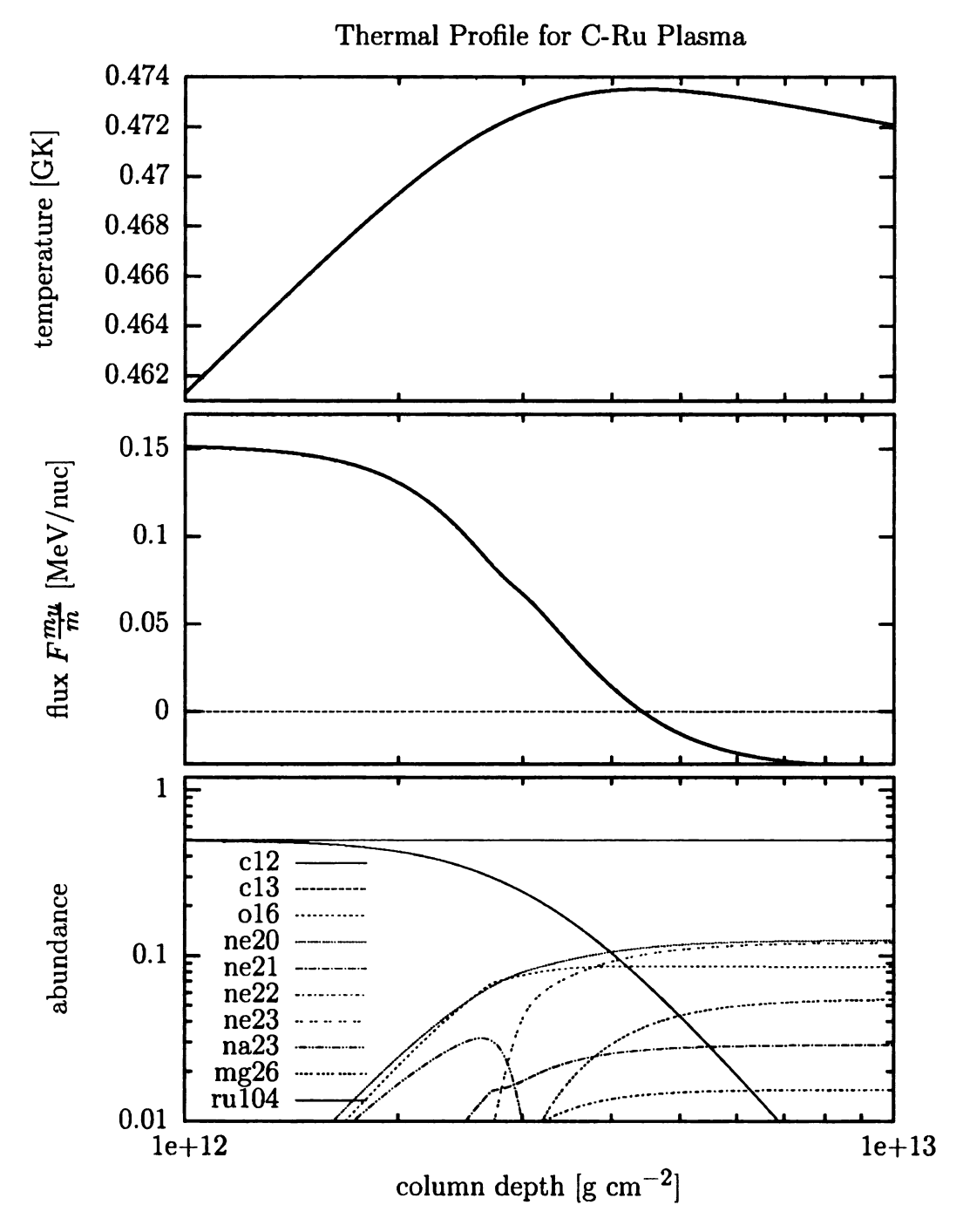


Figure 6.12: Thermal profile for an initial abundance of each 50% of $^{12}\mathrm{C}$ and $^{104}\mathrm{Ru}$, an outer flux $F_0 \frac{m_u}{\dot{m}} = 0.15\,\mathrm{MeV/nuc}$ and an accretion rate of $\dot{m} = 0.2\,\dot{m}_\mathrm{Edd}$

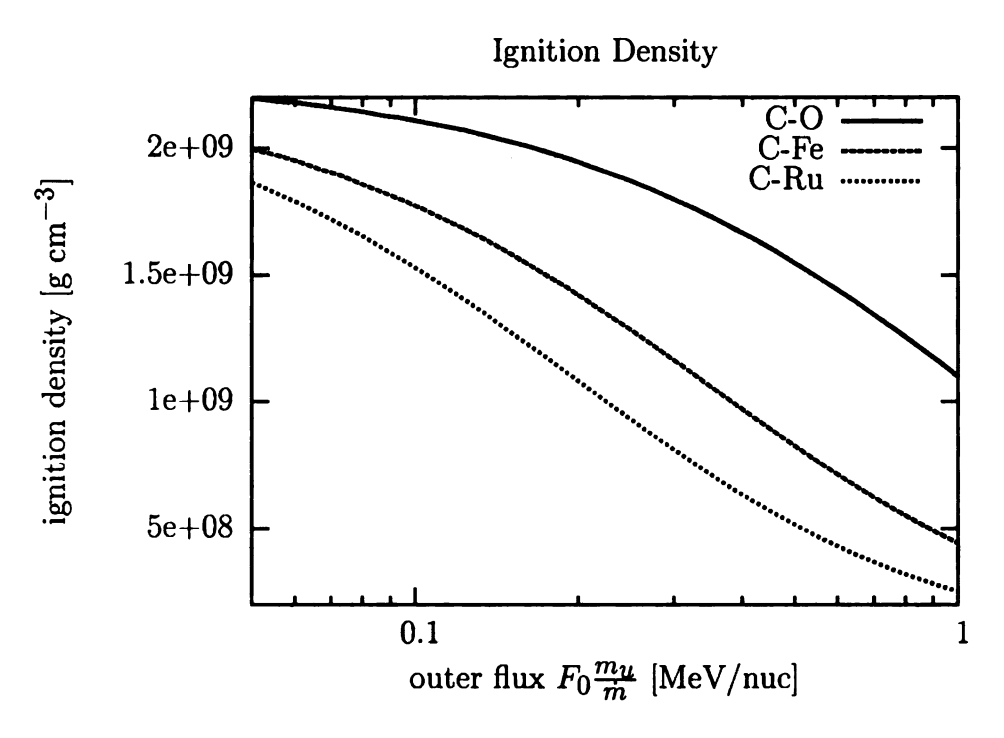


Figure 6.13: Ignition density for different heavy elements with an initial temperature of $T_8 = 4.0$ and an accretion rate of $\dot{m} = 0.2 \, \dot{m}_{\rm Edd}$

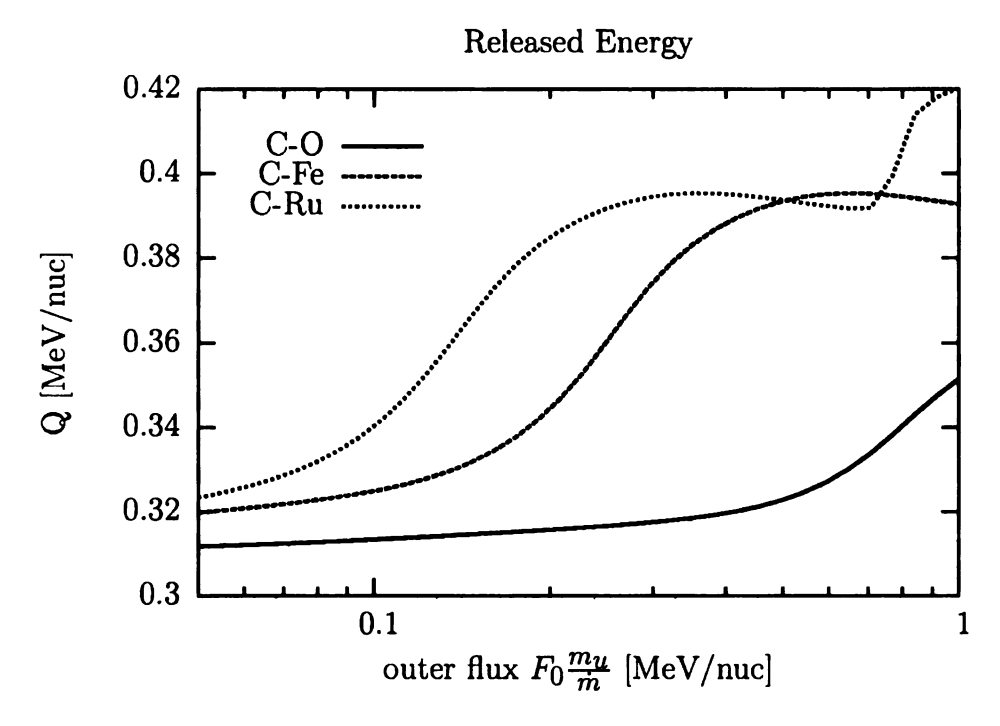


Figure 6.14: Released energy for different heavy elements with an initial temperature of $T_8=4.0$ and an accretion rate of $\dot{m}=0.2\,\dot{m}_{\rm Edd}$

6.7 Influence of Temperature

The ignition results for a fixed accretion rate of $\dot{m}=0.2\,\dot{m}_{\rm Edd}$ and a composition of 50% of each $^{12}{\rm C}$ and $^{56}{\rm Fe}$ show a strong ignition depth and density dependence on the temperature for low flux values (see figures 6.15 and 6.16). For higher flux values the curves approach each other and drop below $10^{12}\,{\rm g\,cm^{-2}}$ and $10^{9}\,{\rm g\,cm^{-3}}$, respectively. The released energy (figure 6.17) changes strongly for the three lower temperatures as a function of outgoing flux due to crossing the threshold value for electron capture (see section 6.4). For a temperature of $T_8=5.0$ the ignition depth is low enough for all flux values in the chosen range to burn all the material before the critical density for electron capture is reached. Figure 6.18 shows the density as a function of ignition density. In the overlapping ranges for different temperatures the released energy clearly shows a very small direct dependence of the Q value on the temperature.

Note that for all calculations the givien temperatures are the outer boundary values at $y = 10^{10} \,\mathrm{g\,cm^{-2}}$. The temperature at the ignition points is remarkably higher for high flux values.

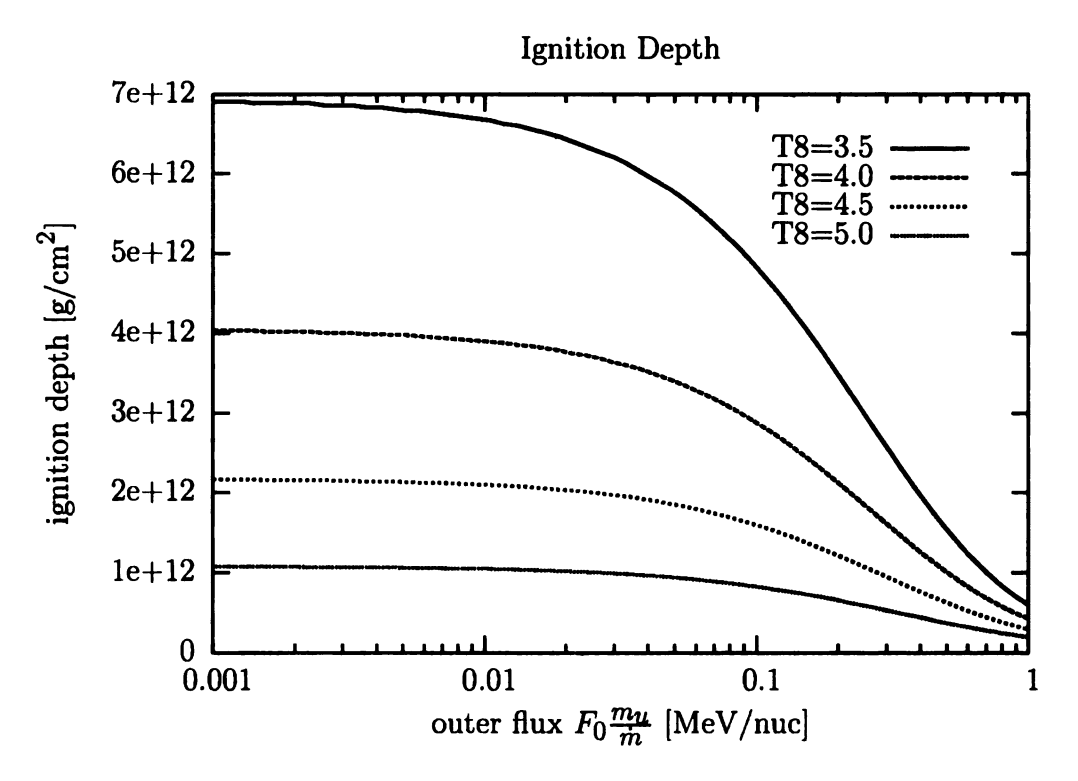


Figure 6.15: Ignition depth for different temperatures at an accretion rate of $\dot{m}=0.2\,\dot{m}_{\rm Edd}$ and a composition of 50% of each $^{12}{\rm C}$ and $^{56}{\rm Fe}$.

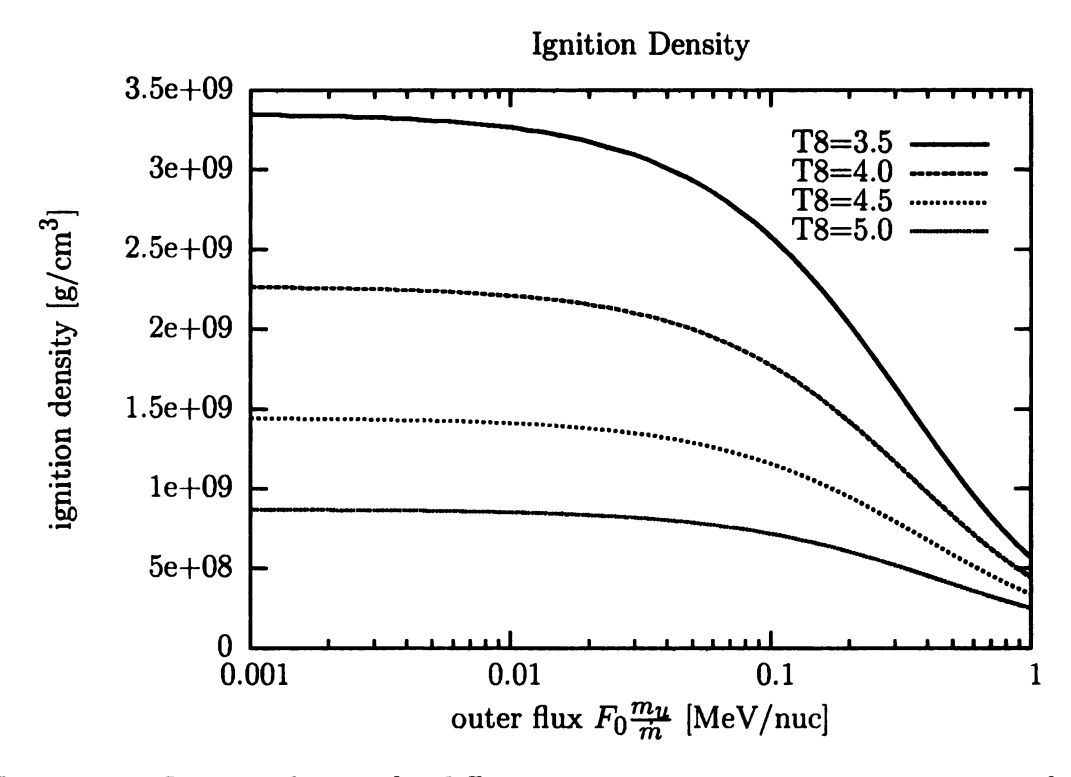


Figure 6.16: Ignition density for different temperatures at an accretion rate of $\dot{m} = 0.2 \,\dot{m}_{\rm Edd}$ and a composition of 50% of each $^{12}{\rm C}$ and $^{56}{\rm Fe}$.

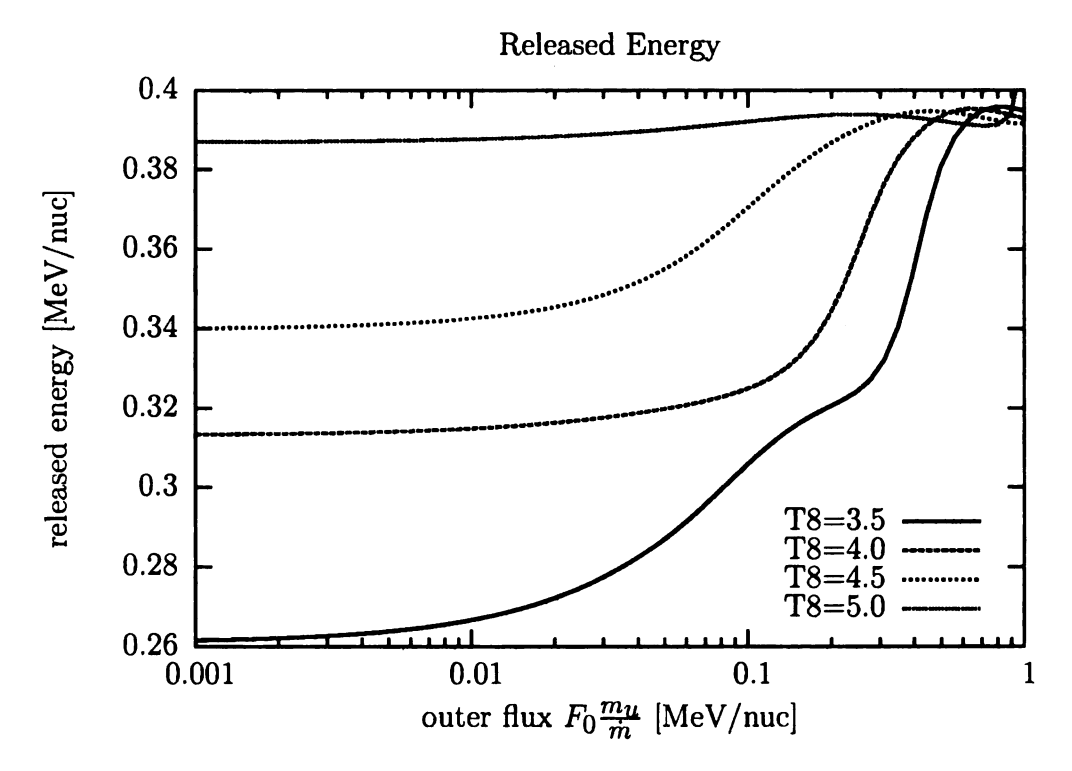


Figure 6.17: Released energy for different temperatures at an accretion rate of $\dot{m}=0.2\,\dot{m}_{\rm Edd}$ and a composition of 50% of each $^{12}{\rm C}$ and $^{56}{\rm Fe}.$

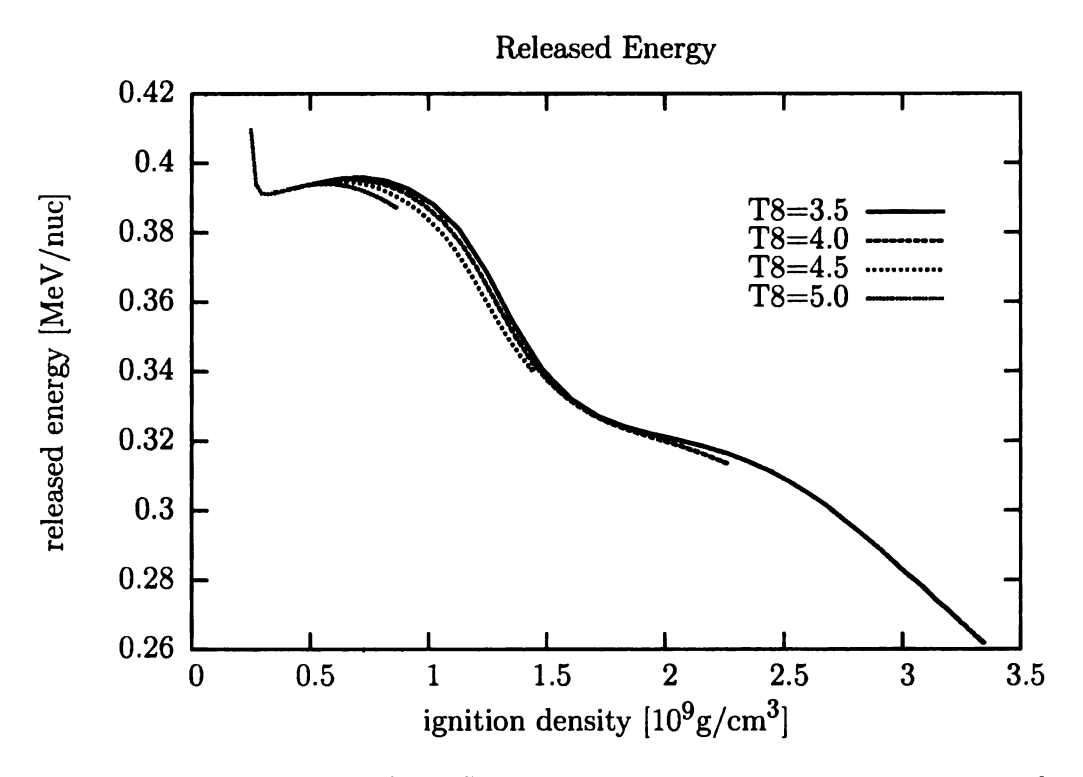


Figure 6.18: Released energy for different temperatures at an accretion rate of $\dot{m}=0.2\,\dot{m}_{\rm Edd}$ and a composition of 50% of each $^{12}{\rm C}$ and $^{56}{\rm Fe}.$

Chapter 7

Linear Stability Analysis

7.1 Linear Perturbation Equations

In order to be able to do a linear stability analysis a steady state solution is needed. Although the star's outer layers are not perfectly in steady state, the time scales at which the structure of these layers change are much larger than the burning time scale, so that the assumption of a time independent thermal structure holds for this model. For an inward moving parcel of burning plasma the Lagrangian Perturbation in its linearized form can be applied

$$\Phi(y,t) = \Phi_0(y) + \Phi'(y,t)$$
 (7.1)

where Φ_0 is the solution obtained by steady state integration and Φ' is an infinitesimal perturbation, which satisfies the condition

$$\frac{\Phi'}{\Phi} \ll 1 \tag{7.2}$$

This infinitesimal character allows to neglect terms of higher order. The important property of the Lagrangian method is that a change of the quantity Φ is computed in

a mass shell not at a given spatial position (Eulerian perturbation). The perturbation is arbitrary and can be written generally as a complex variation

$$\Phi'(y,t) = \delta\Phi(y) \exp(\omega t) \tag{7.3}$$

with the complex quantity ω which plays the role of a growth factor of the perturbation. Normalizing the amplitude to the steady state quantity Φ_0 yields

$$\Phi(y,t) = \Phi_0(y) [1 + \phi(y) \exp(\omega t)]$$
(7.4)

with a perturbation function $\phi(y)$.

7.2 Stability and Overstability

The solution is finally a complex quantity with the complex growth frequency $\omega = \omega_r + i\omega_i$. The stability of the system can be obtained from the value of this complex ω . A closer look at the exponential function shows that for positive values for ω_r the perturbation $\phi(y)$ increases with time whereas negative values cause the external impact to die out with time. The imaginary part of the frequency does not give any information about the amplitude of the perturbation. The stability criterion can therefore be summarize as follows: A found solution of the quantity is

stable if
$$\omega_r < 0$$
 (7.5)

indifferent if
$$\omega_r = 0$$
 (7.6)

unstable if
$$\omega_r > 0$$
. (7.7)

The real part of ω does not only give information about the stability, but also about the time scale of the rise and damping of the perturbation. This time is called

e-folding time, is connected to ω as

$$\tau_e = \frac{2\pi}{|\omega_r|} \tag{7.8}$$

and denotes the time for the perturbation to increase or decrease about a factor of e.

Although the imaginary part ω_i does not determine the stability, it indicates oscillations in the perturbation during the burning

$$\Phi'(y,t) = \delta\Phi(y) \exp(\omega_r t) \exp(i\omega_i t). \tag{7.9}$$

In case of a positive real part ω_r and an imaginary part unequal zero, the unstable mode is called *overstable*. The oscillation period Π is given by

$$\Pi = \frac{2\pi}{|\omega_i|}.\tag{7.10}$$

7.3 Application to the Stellar Model

The important quantities that determine the burning processes are the temperature, the density and the outcoming energy flux. The stability analysis therefore concentrates on perturbations to these quantities, namely

$$T(y,t) = T_{ss}(y) \left(1 + \theta(t) \exp(\omega t)\right), \tag{7.11}$$

$$\rho(y,t) = \rho_{\rm SS}(y) \left(1 + \zeta(t) \exp(\omega t)\right),\tag{7.12}$$

$$F(y,t) = F_{ss}(y) (1 + f(t) \exp(\omega t)), \qquad (7.13)$$

where the subscript ss denotes the steady state profile and the time t in the perturbing functions is related to the column depth like $dy/dt = \dot{m}_{\rm acc}$. The new stellar equations

are now in general complex quantities. The solution of the system of differential equations therefore yields for every complex growth frequency $\omega = \omega_r + i\omega_i$ a set of three complex functions.

7.4 Perturbation Function

The perturbation functions (θ, ζ, f) are dimensionless functions with an amplitude much smaller than one. The duration of the perturbation (t_p) should be a non negligible fraction of the total burning time. In these calculations a fraction of 25% of the total burning time was chosen and the following shape of the function was used (see figure 7.1)

$$\theta(t), \zeta(t), f(t) = A_0 \begin{cases} 1 & \text{for } \frac{t}{tp} < \frac{1}{3} \\ \frac{1}{2} \cos\left[\pi\left(\frac{3}{4}\frac{t}{tp} - \frac{1}{4}\right)\right] + \frac{1}{2} & \text{for } \frac{1}{3} \le \frac{t}{tp} \le \frac{5}{3} \\ 0 & \text{for } \frac{t}{tp} > \frac{5}{3}, \end{cases}$$
(7.14)

where A_0 denotes the amplitude of the perturbation and was set to 10^{-3} . The exact shape of the function was chosen arbitrarily. Some tests with different functions show, that smooth functions lead to less numerical noise in the solution for ω in comparison to a simple step function. The shape of the function as well as the exact duration of the perturbation do affect the values for $\epsilon_{\rm re,im}$ (see section 7.5), but do not affect the value of ω , except for very short $(t_p \lesssim 0.05\,t)$ or very long $(t_p \gtrsim 0.8\,t)$ durations of the perturbation.

7.5 Calculation Procedure

For the complex stability analysis a reasonable range of the complex growth frequency ω has to be scanned. For each value of ω the thermal structure equations have to be

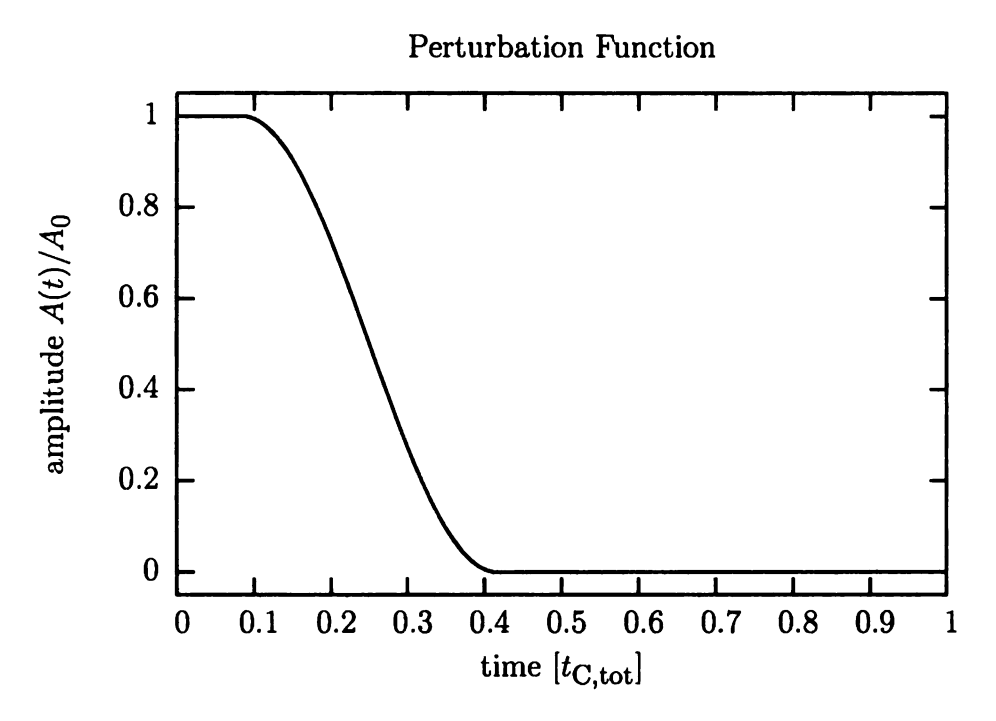


Figure 7.1: Perturbation function

solved. Among the final set of solutions $S(\omega)$ the ones have to selected, that match the inner boundary conditions of the steady state solution. These conditions are:

- The solutions for ρ, T and F must be real.
- The real parts of the complex structure equations have to match the steady state solution.

As ω has to be discretized, the solutions generally can only fit within a threshold value ϵ_{re} for the real and ϵ_{im} for the imaginary part. The numerical conditions can

be written as follows

$$\frac{\operatorname{Im}(\rho)}{|\rho|} \leq \epsilon_{\operatorname{im}},$$

$$\frac{\operatorname{Im}(T)}{|T|} \leq \epsilon_{\operatorname{im}},$$

$$\frac{\operatorname{Im}(F)}{|F|} \leq \epsilon_{\operatorname{im}},$$

$$\frac{|\operatorname{Re}(\rho) - \rho_{\operatorname{ss}}|}{|\rho|} \leq \epsilon_{\operatorname{re}},$$

$$\frac{|\operatorname{Re}(T) - T_{\operatorname{ss}}|}{|T|} \leq \epsilon_{\operatorname{re}},$$

$$\frac{|\operatorname{Re}(F) - F_{\operatorname{ss}}|}{|F|} \leq \epsilon_{\operatorname{re}},$$

where the subscript ss denotes the steady state result. The values for ε_{re} and ε_{im} vary with the region in the complex plane for ω . For large positive $\omega_r \min(\epsilon_{\rm re,im}) \lesssim$ 10^{-2} , at the transition from unstable to stable burning min($\epsilon_{\rm re,im}$) $\lesssim 10^{-4}$. The large values for very unstable burning are caused by the large grid size, that had to be chosen in order to reduce the computing time (see section 7.6). Interpolating between the grid points in the complex plane reduces the threshold values $\min(\epsilon_{\rm re,im})$ significantly, but does not change the result. Figure 7.2 shows two examples for a solution for the complex ω . Dark areas indicate the regions where the solution conditions (equations 7.15) are fulfilled. For the growth rate of the perturbation it is instructive to make comparisons to the total carbon burning time. A perturbation that grows on much larger time scales than the burning time can not affect the the burning process significantly. Growth times much smaller than the burning time are considered to cause instabilities. The total carbon burning time therefore sets a minimum for the modulus of $|\omega|$. As the initial perturbation amplitude is small (10⁻³) it is reasonable to start with a modulus of $|\omega|$ that can increase the perturbation to at least a few percent. In the following calculations the minimum value for was set

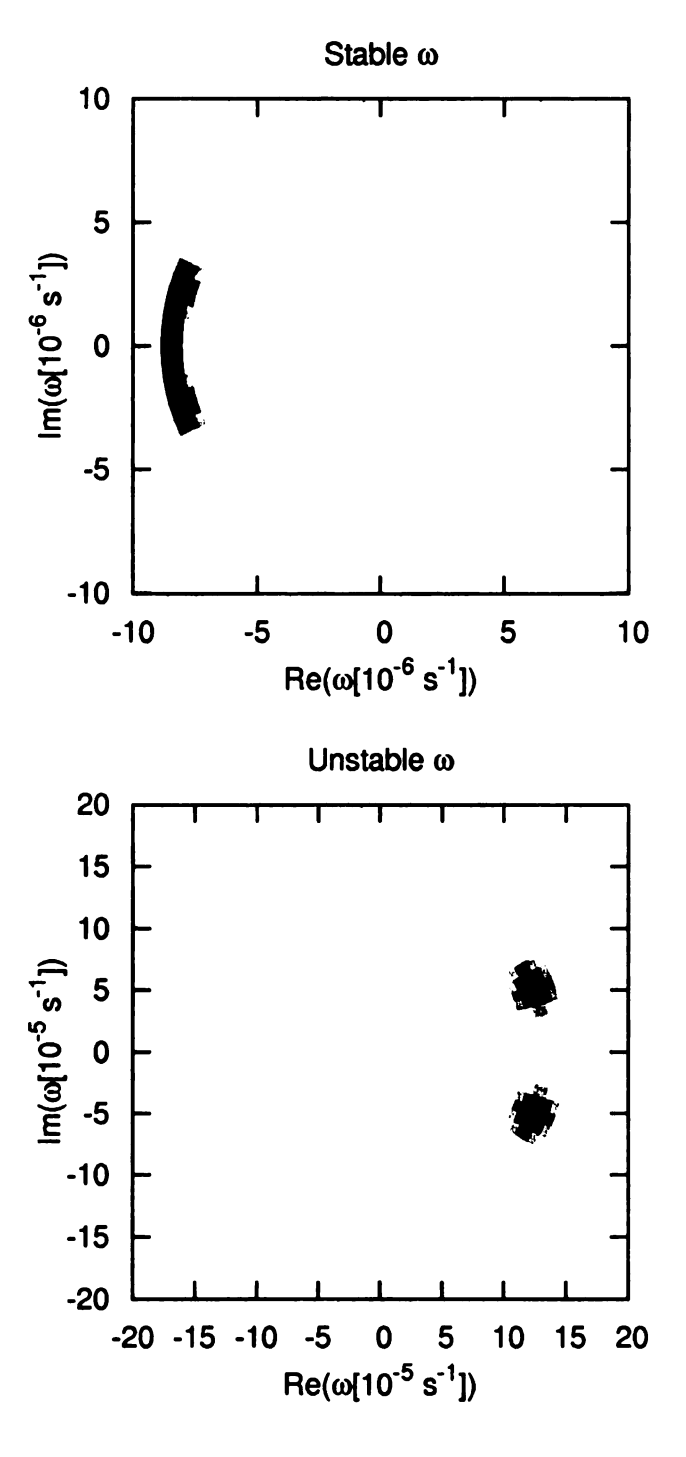


Figure 7.2: Example for a stable and an unstable solution for ω . Light gray areas correspond to values of ω , in which equations 7.15 are not fulfilled (relative differences $> \epsilon_{\rm re,im}$). Dark areas indicate solutions for all equations 7.15.

to

$$|\omega_{\min}| = \frac{3}{t_b},\tag{7.16}$$

where t_b is the total burning time and the arbitrary factor of 3 corresponds to an increase of 2%,

$$f(t=0)\exp(3) \approx 10^{-3} \cdot 20 = 0.02.$$
 (7.17)

The upper value was set to

$$|\omega_{\text{max}}| = 10|\omega_{\text{min}}| = \frac{30}{t_b},\tag{7.18}$$

which corresponds to a maximum possible growth factor of $\approx 10^{10}$.

In figure 7.3 the growth time in units of the total carbon burning time is plotted. The transition between unstable and stable burning is limited to a very narrow flux range, which gives a distinct number for the threshold value.

7.6 Discretization and Computing Time

The most intuitive way of dicretizing the ω grid in the complex plane is transforming ω to polar coordinates

$$\omega = \omega_r + i\,\omega_i = |\omega|(\cos\phi + i\,\sin\phi) \tag{7.19}$$

and discretize the radius $|\omega|$ and the angle ϕ in the complex plane. The stepsize was determined after some tests after having found the size of the solution pattern. The

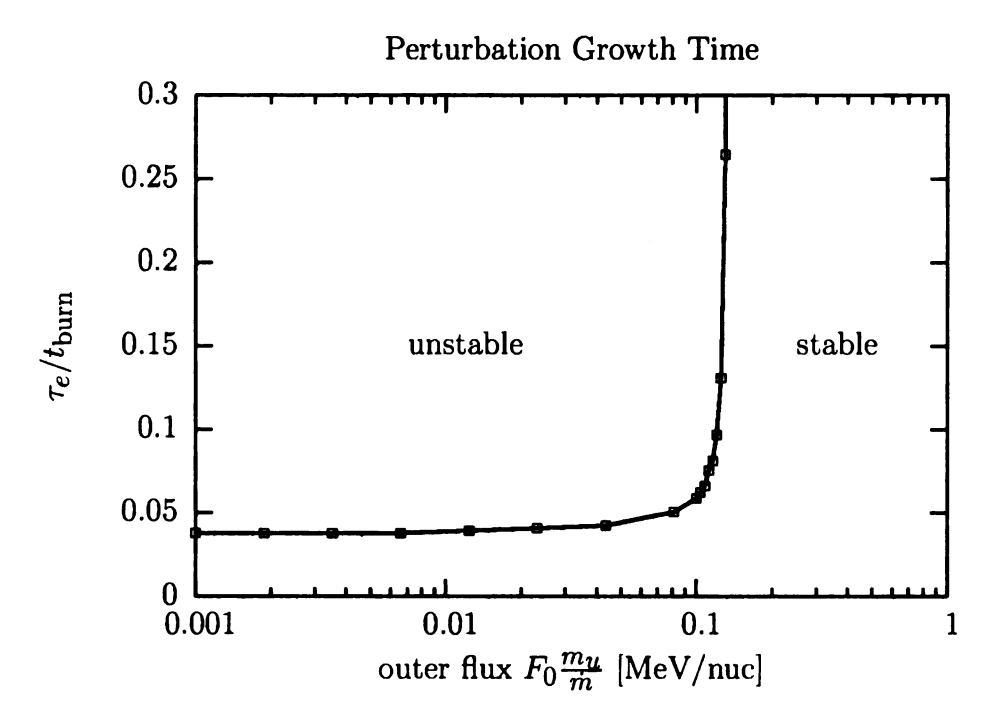


Figure 7.3: Growth time of the perturbation in units of the total carbon burning time for $T=4\times 10^8$ K, a composition of equal parts of carbon and iron and an accretion rate of $\dot{m}=0.2\dot{m}_{\rm Edd}$.

radius was divided into 30 steps

$$r_k = |\omega_{\min}| + k \frac{9|\omega_{\min}|}{29}, \qquad k = 0...29,$$
 (7.20)

for the angle ϕ 90 steps were choosen

$$\phi_k = k \frac{2\pi}{89}, \qquad k = 0...89. \tag{7.21}$$

The grid in the complex plane therefore consists of 2700 parcels. The integration time for one ω_k was roughly one second. As the Bulirsch-Stoer integrator in the reaction network uses an adaptive stepsize and the time of the fourth order Runge-Kutta integrator can be neglected, this integration time was pretty much independent of the given stepsize. The errors in the reaction network concerning the abundances ϵ_Y

with

$$\epsilon_Y = 1 - \sum_i X_i \tag{7.22}$$

were less than 10^{-15} for all test calulations. The error for the thermal structure equations in the Runge-Kutta integrator were not measurable for stepsizes above $N \approx 1000$. The total computational time in order to determine the stability for one set of parameters was therefore 45-50 minutes. In order to find the threshold flux between unstable and stable burning for a fixed accretion rate, temperature and initial composition a set of ≈ 30 stability calculations was practicable, which took roughly one day.

7.7 Results of the Linear Stability Analysis

7.7.1 Stability Flux

As mentioned in section 6.1.2 the flux value is used as a free parameter. For a fixed set of outer boundary values the flux, at which the fusion switches from an unstable to a stable burning, was determined. This flux value is called stability flux in this thesis. For all fluxes lower than this threshold the burning is unstable, for all higher values it is stable. The big advantage of determining the stability flux is, that for any given flux, determined by various models and boundary values, one can directly find out whether the carbon burning is stable or not, without doing the stability analysis again for every set of parameters. In addition to that, the computed flux value from other calculations does not only show whether stable or not, but also how close to the stability this flux is.

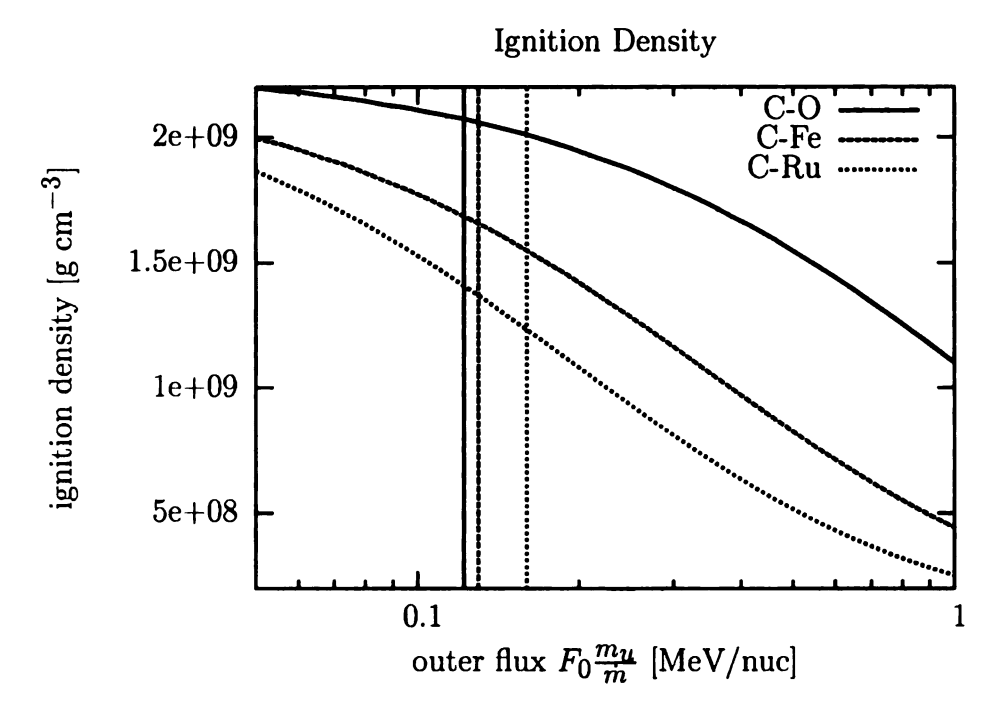


Figure 7.4: Influence of heavy elements on the stability. The vertical lines indicate the threshold flux value for stable burning. Higher flux values are stable, lower are unstable.

7.7.2 Influence of heavy elements

In figure 7.4 the ignition densities can be seen for three initial compositions, each consisting to equal parts of 12 C and the heavy element (16 O, 56 Fe, 104 Ru). The stability threshold flux is indicated by the vertical line, giving the following values for a temperature of $T_8 = 4.0$ and an accretion rate of $\dot{m} = 0.2 \, \dot{m}_{\rm Edd}$

$$^{12}\text{C} - ^{16}\text{O}$$
: $F_c = 0.12 \,\text{MeV/nuc}$ $y_c = 3.6 \times 10^{12} \,\text{g cm}^{-2}$ (7.23)
 $^{12}\text{C} - ^{56}\text{Fe}$: $F_c = 0.13 \,\text{MeV/nuc}$ $y_c = 2.65 \times 10^{12} \,\text{g cm}^{-2}$
 $^{12}\text{C} - ^{104}\text{Ru}$: $F_c = 0.16 \,\text{MeV/nuc}$ $y_c = 1.75 \times 10^{12} \,\text{g cm}^{-2}$

with strongly decreasing ignition column depth for heavier elements.

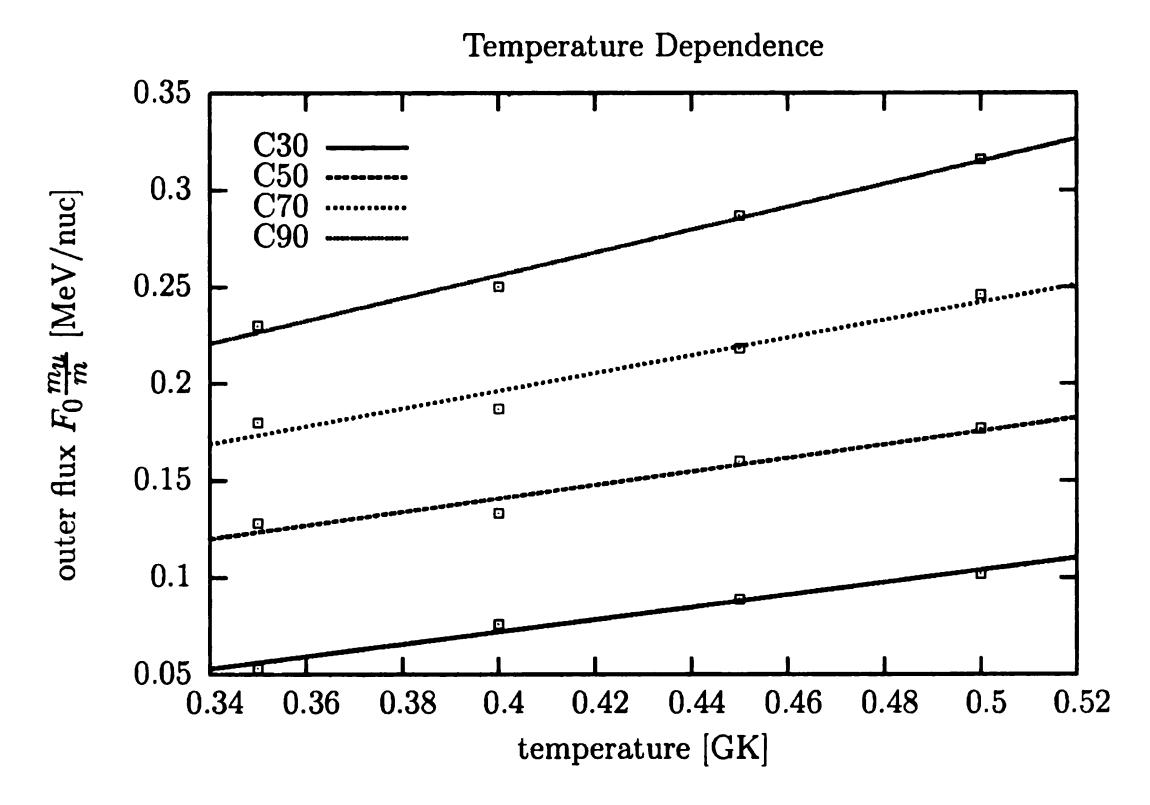


Figure 7.5: Influence of the temperature on the stability. For flux values higher than the shown curves, the burning is stable, for lower values it is unstable

7.7.3 Influence of the Temperature

The calculations for different temperatures are all set up with an initial composition of ¹²C and ⁵⁶Fe at different ratios. The results (figure 7.5) clearly show a strong temperature dependence for all compositions. Even more sensitive to the stability flux is the composition of the material. Higher carbon abundances require much higher flux values for a stable burning.

7.7.4 Influence of the Accretion Rate

The dependence of the accretion rate on the stability flux (figure 7.6) is fairly small. In the range of 10 - 30% the Eddington limit the threshold values barely increase.

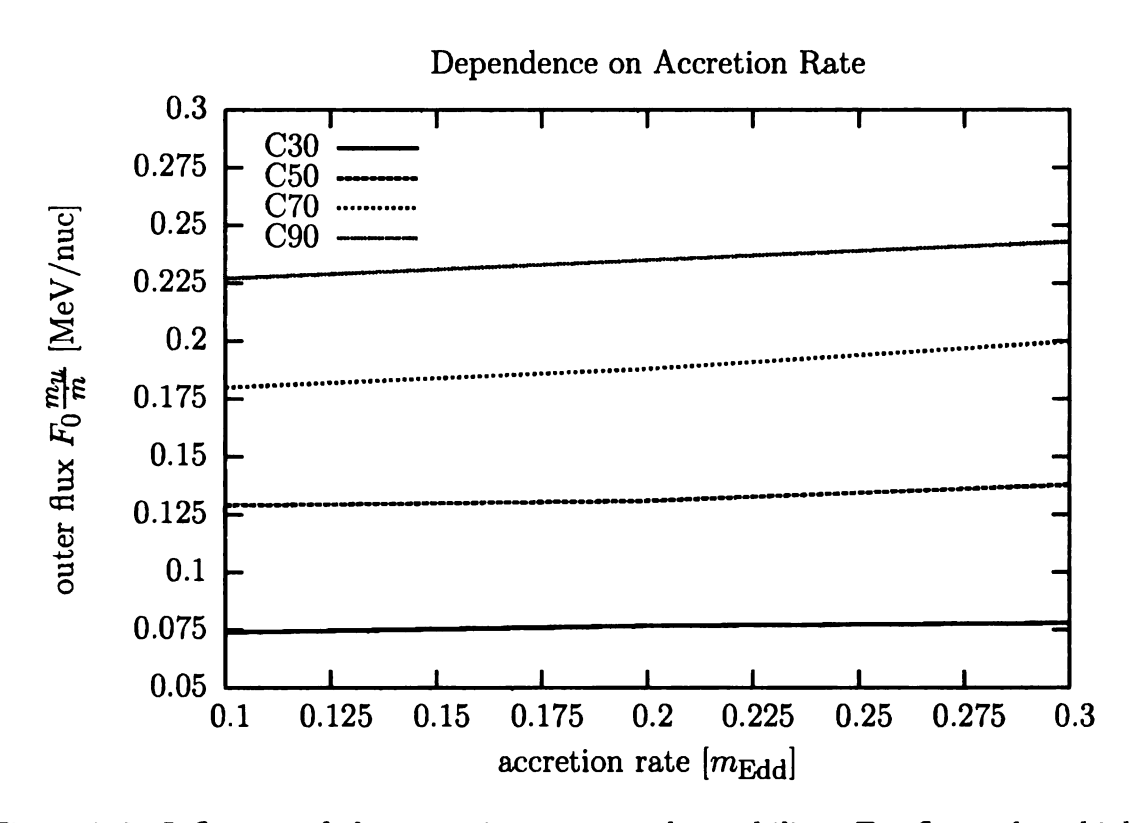


Figure 7.6: Influence of the accretion rate on the stability. For flux values higher than the shown curves, the burning is stable, for lower values it is unstable

7.8 Burning Regimes

7.8.1 Direct and Delayed Bursts

For an unstable burning regime the question arises, at what point in the carbon burning process the perturbation starts growing significantly and causes the ignition of the burst. In order to determine the ignition region, the burning process the is devided into two parts. The first part covers the burning regime from 90% to 50\% of the initial carbon abundance (hereafter region I), the second one refers to the burning region from 50% to 10% (hereafter region II). If an instability already occurs in region I the burst is called an direct burst, if region I is stable but region II is unstable the burst is called a delayed burst. In order to determine the ignition time, a complex stability analysis is done separartetly for each region. It turns out, that burning region II shows an unstable character for all flux values below the stability threshold flux, whereas burning region I is only unstable for low flux values, corresponding to deeper ignition depths, and switches to a stable mode for intermediate fluxes. That means that that for increasing fluxes the unstable ignition front moves lower carbon abundances until all the carbon is burned before reaching the unstable depth. Figure 7.7 shows the direct and delayed bursts for a fixed initial composition of equal parts of carbon and iron and an accretion rate of $\dot{m}=0.2\,\dot{m}_{\rm Edd}.$ In figure 7.9 the fraction of carbon in the initial composition is varied. The switching line from direct to delayed bursts roughly lies parallel to the threshold stability line. Figure 7.8 shows the dependence on the accretion rate for the same composition and a temperature of $T_8 = 4.0$.

7.8.2 Overstable Modes

As mentioned in section 7.2 the flame is overstable if the imaginary part of the growth frequency is unequal zero. This leads to oscillations in the increasing perturbation.

Direct and delayed bursts delayed direct threshold flux 0.32 outer flux $F_0 \frac{mu}{m}$ [MeV/nuc] stable 0.16 00000 0000 000000XX un-0.08 stable 2 0.04 0.36 0.38 0.42 0.48 0.5 0.34 0.4 0.440.460.52temperature [GK]

Figure 7.7: Direct and delayed bursts for an accretion rate of $\dot{m}=0.2\,\dot{m}_{\rm Edd}$ and a composition of $^{12}{\rm C}$: $^{56}{\rm Fe}=1:1$

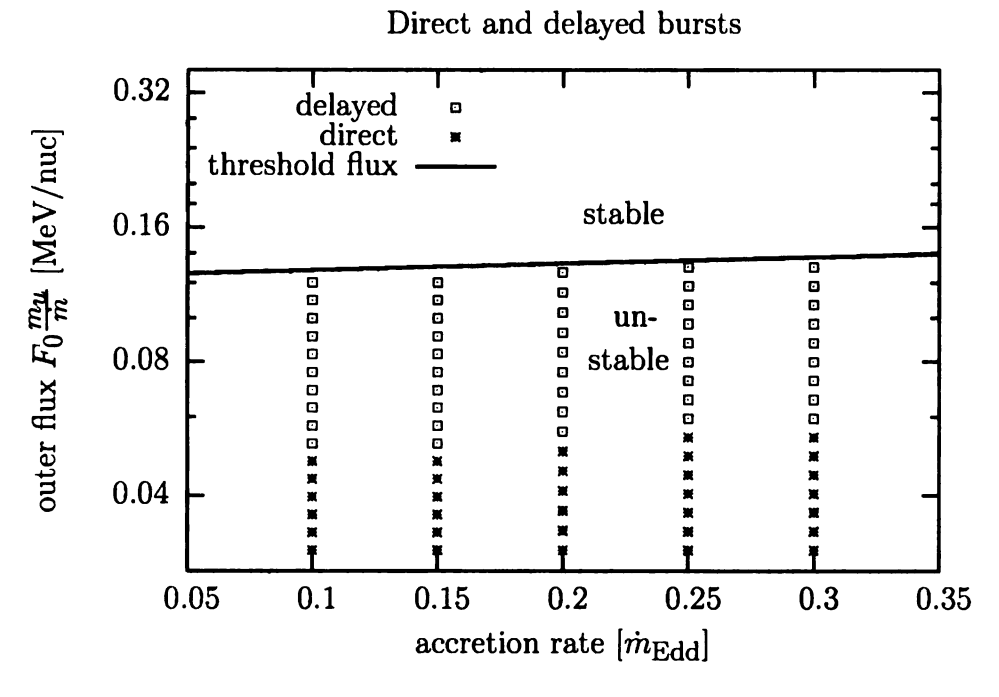


Figure 7.8: Direct and delayed bursts for an a temperature of $T_8=4.0$ and a composition of $^{12}\mathrm{C}:^{56}\mathrm{Fe}=1:1$

Direct and delayed bursts 0.384 delayed direct threshold flux outer flux $F_0 \frac{m_u}{m}$ [MeV/nuc] 0.1920 stable 00000 0.096 0.048 0.024 unstable 0.3 0.2 0.4 0.5 0.6 0.7 8.0 0.9 0.1 1 carbon fraction

Figure 7.9: Direct and delayed bursts for an a temperature of $T_8=4.0$ and an accretion rate of $\dot{m}=0.2\,\dot{m}_{\rm Edd}$

As at a given temperature, density, accretion rate and composition the flux range, within which these oscillations appear and disappear is very small, it is not possible to make a general statement about the occurence of these oscillations based on the relatively large flux steps, that were used in the stability calculations. A wider flux range, however, could be determined for high temperatures above $T_8 > 4.5$ and high carbon abundances (70%, 90%), where they were easy to detect. Focussing on this boundary values, the evolution of the oscialltions follows an interesting pattern. For very low flux values the unstable flame does not show overstable modes. At the lower threshold flux value the solution for ω undergoes a bifurcation and branches out to two overstable modes (see figure 7.10). The imaginary part increases with increasing flux up to a maximum of 60 cycles during the total C burning time. Increasing the flux a real unstable mode appears and replaces the overstable modes, see figure 7.11. In figure 7.12 the frequency in units of total carbon burning time is shown. As expected the oscillations appear in pairs with positive and negative imaginary part

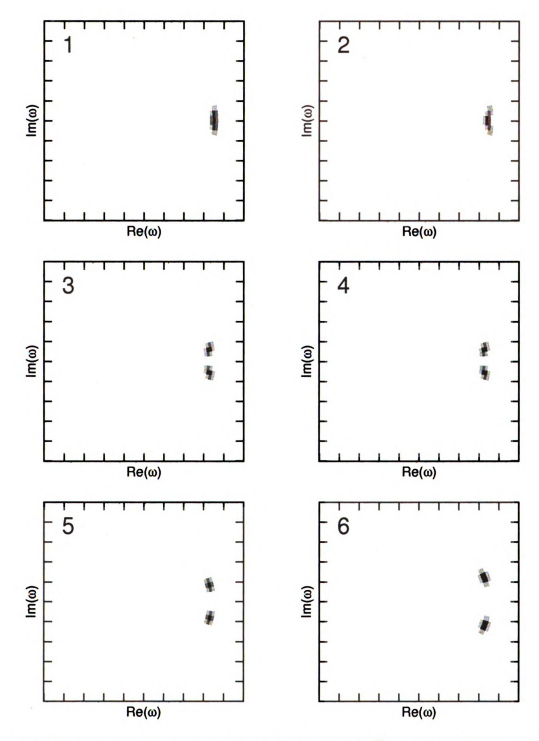


Figure 7.10: Appearance pattern of the oscillation for $F_0 \frac{m_1}{m_1} \approx 0.107\,\mathrm{MeV/nuc}$, $T_8 = 5.0$, 70% carbon. Light gray areas correspond to values of ω , in which equations 7.15 are not fulfilled (relative differences $> \epsilon_{\mathrm{re,im}}$). Dark areas indicate solutions for all equations 7.15.

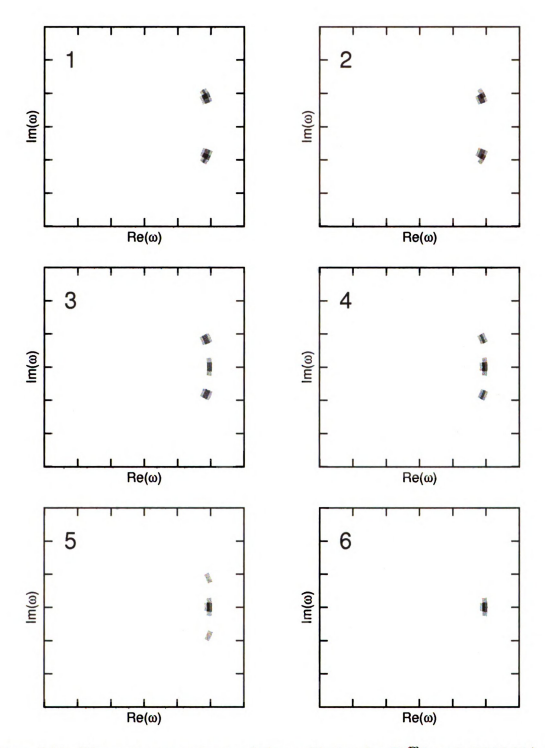


Figure 7.11: Disappearance pattern of the oscillation for $F_0 \frac{m_0}{m} \approx 0.153 \, \mathrm{MeV/nuc}$, $T_8 = 5.0$, 70% carbon. Light gray areas correspond to values of ω , in which equations 7.15 are not fulfilled (relative differences $> \epsilon_{\mathrm{re,im}}$). Dark areas indicate solutions for all equations 7.15.

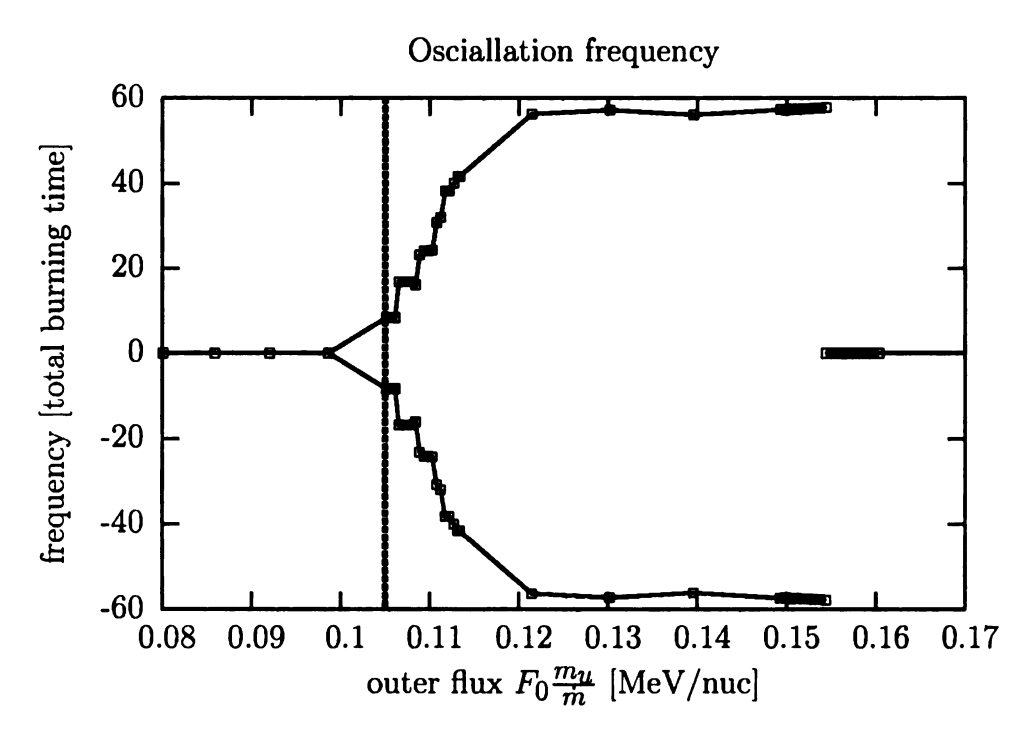


Figure 7.12: Appearance and disappearance of the oscillation for $T_8 = 5.0$ and 70% carbon.

 ω_i and the same absolute value: $\omega_i^+ = -\omega_i^-$.

A closer look at the region where these oscillations are generated shows that burning region I does not have overstable modes at all. The patterns in region II exactly match the pattern of the total burning process which leads to the conclusion, that the oscillations are driven by reactions in the region, where most of the carbon is already burned and a significant amount of the nuclear energy is already released. In all the tested cases, the flame switches from a direct to a delayed burst roughly at the flux value at which the oscillation appears. This transition is indicated by the vertical line in figure 7.12.

Chapter 8

Application

8.1 Neutron stars in quiescence

Aside from direct burst oberservation and analysis of the flare itself, the further time evolution of the neutron star during cooling gives information about the burning circumstances in the carbon burning layer. Brown & Cumming [19] found that the temperature profile of the steady state burning during accretion and the profile at the end of the outburst differ by less than 4% over the entire column depth range. Mapping the crustal heating with the observed cooling lightcurves allows to determine the temperature and flux right behind the ignition front of the steady state burning. Running a stability analysis with the given temperature and accretion rate for different compositions of the ocean before the unstable ignition gives a relation between the composition and the threshold flux values for a superburst. The mapped flux value in the ignition front sets a limit on the composition for unstable carbon burning.

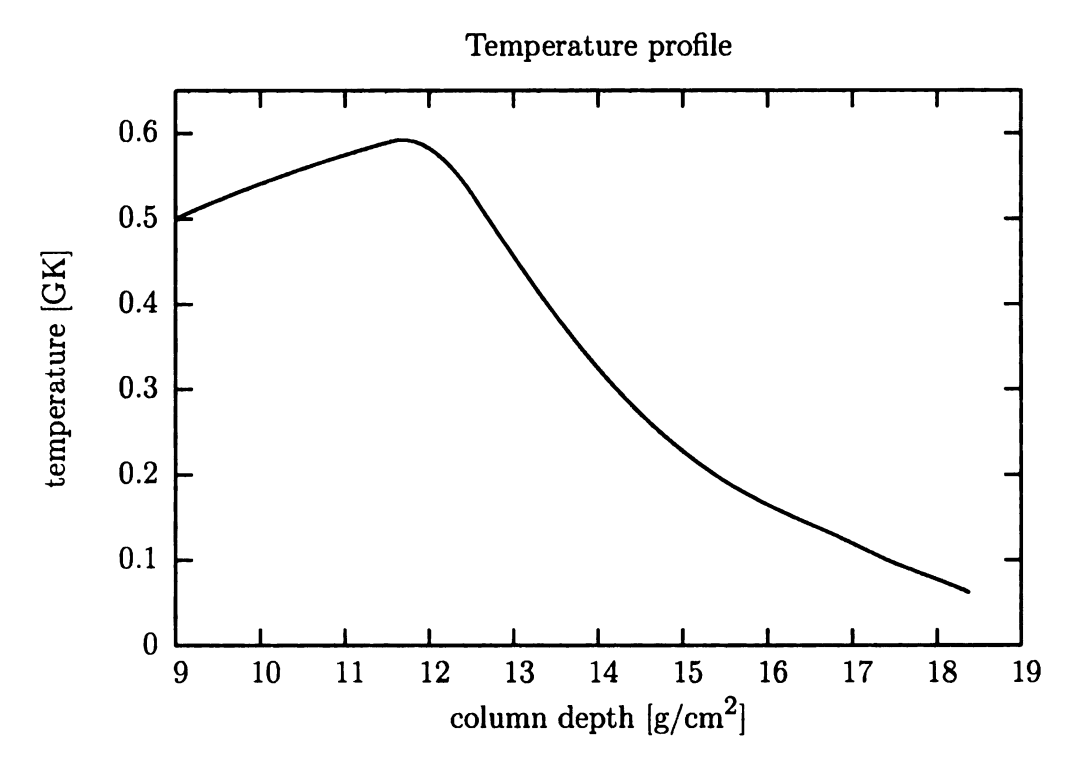


Figure 8.1: Thermal profile for KS 1731-260

8.2 The neutron star in KS 1731-260

The neutron star has been observed to cool following a 2.5 yr-long outburst (Wijnands et al. [20]). The star has a mass of $1.6\,M_\odot$ and a radius of $11.6\,\mathrm{km}$, which leads to a redshift factor of 1+z=1.32 and a surface gravity of $g=2.3\times10^{14}\,\mathrm{cm\,s^{-2}}$. The outburst accretion rate is observed to be $\dot{M}\approx10^{17}\,\mathrm{g\,s^{-1}}$, yielding an accretion rate per unit area of $\dot{m}\approx0.095\,\dot{m}_\mathrm{Edd}$. Fitting a cooling curve to the observed data the temperature behind the ignition front was determined to be $T_b=3.8\times10^8\,\mathrm{K}$ (Brown & Cumming [19]), corresponding to a peak temperature at the ignition of $T_p=6\times10^8\,\mathrm{K}$ (see figure 8.1). The flux value at the outer boudary was determined to be $0.22\,\mathrm{MeV/nuc}$. The result of the stability analysis can be seen in figure 8.2. The difference between $T=5.5\times10^8\,\mathrm{K}$ and $T=6\times10^8\,\mathrm{K}$ can be neglected. Possible compositions are indicated by the thick line, which yields a fraction of carbon of over $\approx65\%$.

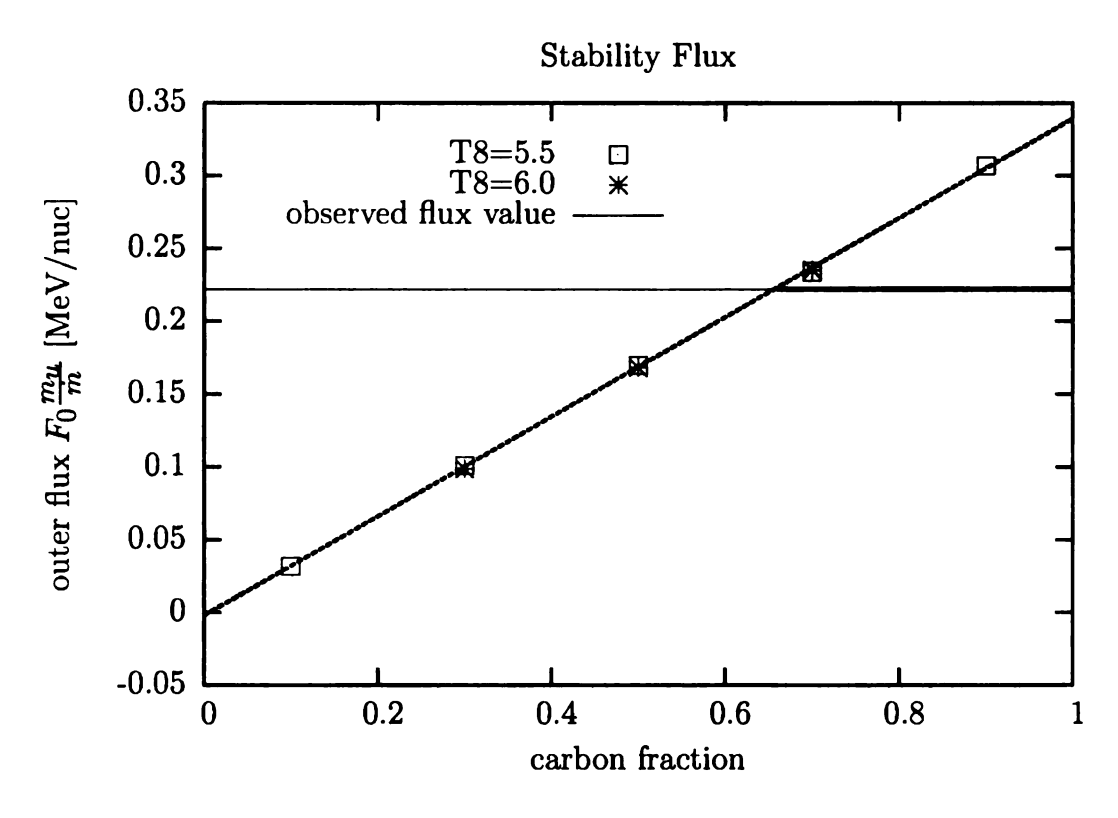


Figure 8.2: Stability flux as a function of composition for KS 1731-260

Chapter 9

Conclusion and Outlook

The work presented in this thesis is a broad theoretical parameter study of the carbon burning processes in the ocean of accreting neutron stars. The main interest focused on the conditions where the nuclear burning switches from a steady state burning to an unstable ignition, leading to a thermonuclear superburst. The study was performed with numerical simulations under the assumption of a sperically symmetric star in one radial dimension. The burning processes were calculated by a full reaction network, including the 45 most relevant isotopes, connected by over 500 weak and strong reactions. The stability analysis was based on a complex number perturbation evolution, giving precise stability threshold values for temperature, flux and accretion rate. For a more precise determination of the point in time, at which the unstable flame ignites, the burning process was not only examined as a whole, but also devided into two sub-regions, associated with direct and delayed bursts. In addition to that oscillations of the perturbation were examined for a set of parameters.

In future work the effects of rotation have to be included in the model as well as consequences of turbulent mixing between the layers. Especially if the mixing timescale is in the order or even significantly shorter than the burning timescale, the resulting heat and material transport will certainly affect the burning and therefore

the stability conditions. Strong mixing can also lead to locally very high accretion rates which are not covered in the present work. Furthermore the observed features during the rise of the flare such as millisecond oscillations are still unconnected to the nuclear burning before the unstable ignition. Concerning the ignition mechanism the influence of shocks and a possible connection to the often observed preceding helium flash before the superburst are not covered in this thesis. With a systematic inclusion of density fluctuations, the sensitivity of the flame to this perturbation has to be examined. In addition to that precise conditions for the appearance and disappearance of burst oscillations are needed as well as a detailed oscillation structure for a larger range of parameters. Finally a transformation of the stability problem with a full reaction network and a complex perturbation analysis to a three dimensional model would certainly approach the model further to the real star.

Appendix A

Thermodynamic Equations

Here a detailed derivation of the thermodynamic equations for the temperature and the flux can be found. Starting with the thermodynamic potential

$$dE = TdS + \mu dN - PdV \tag{A.1}$$

the time derivative of the energy yields

$$\frac{dE}{dt} = T\frac{dS}{dt} + \mu \frac{dN}{dt} - P\frac{dV}{dt}.$$
 (A.2)

Not changing the number of particles nor the volume, the last two terms vanish. Transforming to quantities per unit mass gives

$$\frac{de}{dt} = T\frac{ds}{dt} = T\frac{ds}{dT}\frac{dT}{dt}.$$
(A.3)

The change in energy is given by the total rate $de/dt = \epsilon$, which can be separated into heating and cooling $\epsilon_{\text{heat}}, \epsilon_{\text{cool}}$. Heating is provided by nuclear reactions, the cooling is given by thermal diffusion and neutrino emission. The contribution from thermal diffusion can be derived from the diffusion equation:

$$\frac{\partial}{\partial t}T = \frac{K}{\rho \, c_P} \nabla^2 T \tag{A.4}$$

with the total thermal conductivity K. The diffusion equation can be split up into the continuity equation

$$\frac{\partial}{\partial t}T = -\frac{1}{\rho c_P} \nabla \cdot \mathbf{F} \quad \Leftrightarrow \quad c_P \frac{\partial}{\partial t}T = -\frac{1}{\rho} \nabla \cdot \mathbf{F} \tag{A.5}$$

and Fick's law

$$\mathbf{F} = -K\nabla T \tag{A.6}$$

With the definition of the specific heat

$$c = \frac{T}{N} \frac{\partial S}{\partial T} = T \frac{\partial s}{\partial T} \tag{A.7}$$

equation A.3 can be written as

$$T\frac{ds}{dt} = T\frac{ds}{dT}\frac{dT}{dt} = c_P \frac{\partial}{\partial t}T = -\frac{1}{\rho}\nabla \cdot \mathbf{F} + \epsilon'$$
(A.8)

where ϵ' denotes the other sources and sinks of energy (nuclear heating and neutrino cooling)

Appendix B

Column Depth

The column depth is defined as the integral over the density and can be written in spherical symmetry as follows

$$y(r) = \int_{r}^{\infty} \rho(r)dr. \tag{B.1}$$

In the integration inward the star the accumulated mass above the radius r therefore varies with the initial density at the outer boundary and depends on the equation of state of the material. However, in the neutron star's ocean in the carbon burning region, where the column depths reaches values on the order of $10^{10}-10^{13} \mathrm{g \ cm^{-2}}$, the column depth can be described by an exponential function which barely depend on the initial conditions. The following diagram shows the column depth-density relation for different initial conditions.

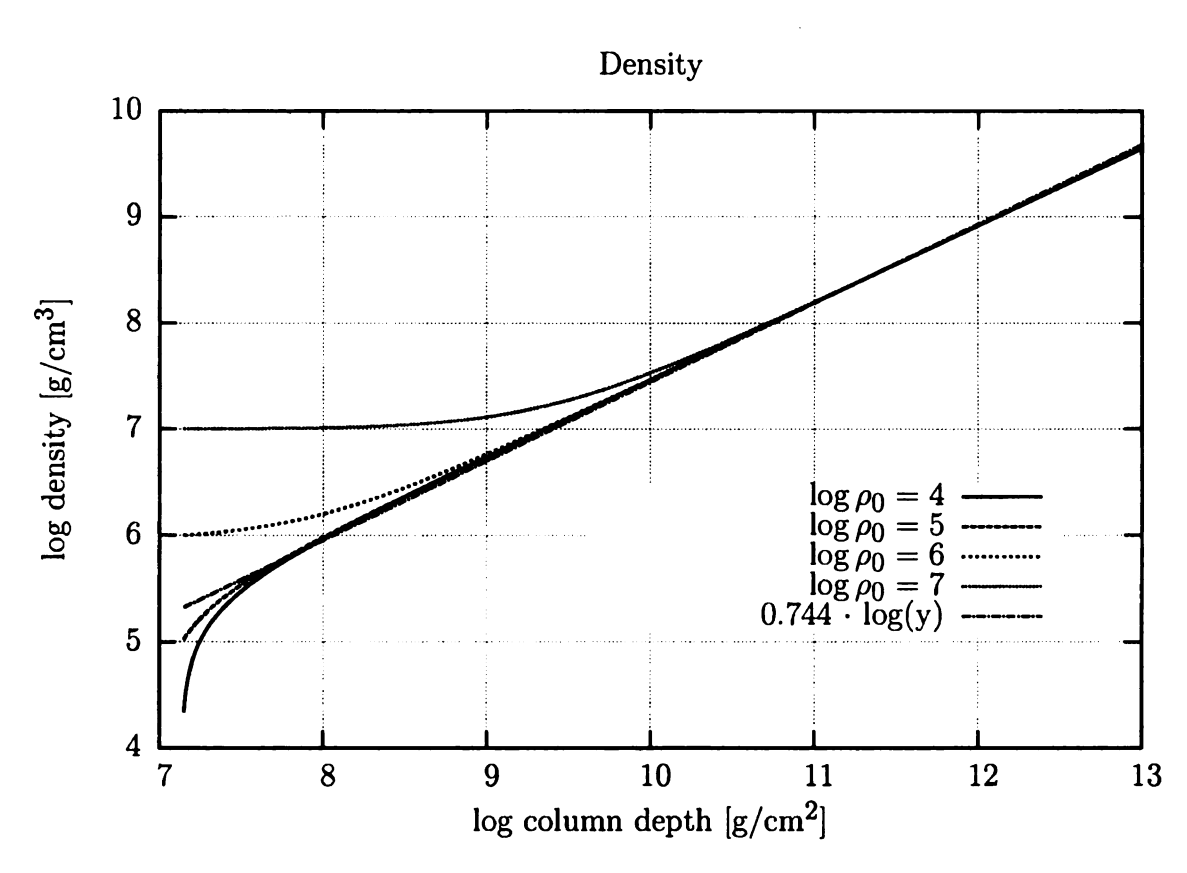


Figure B.1: Relation between column depth and density for various initial conditions

Appendix C

Elements in the Reaction Network

In this thesis a full reaction network is used to determine the elemental abundances. As the temperature and density range is limited and the main focus is on the carbon burning processes only the relevant elements and their reactions are included in the network in order to optimize the computing time. Starting with a very large number of isotopes, this number was reduced by removing elements that change the abundances by less than 10^{-4} . As the released energy is calculated from the abundances, the impact on the energy balance is also very small. The isotopes that are used in the reaction network as well as their mass excess and the total binding energy are tabulated in table C.1.

Element	Mass excess [keV]	Binding energy [keV]
\overline{n}	8071	
$oldsymbol{p}$	7289	
4 He	25930	28296
$^{12}\mathrm{C}$	0	92162
$^{13}\mathrm{C}$	3125	97108
$^{14}\mathrm{C}$	3020	105285
^{12}N	17338	74041
^{13}N	5346	94105
^{14}N	2863	104659
^{15}N	101	115492
¹³ O	23111	75558
¹⁴ O	8006	98733
¹⁵ O	2855	111956
$^{16}\mathrm{O}$	-4737	127619
¹⁷ O	-809	131763
¹⁸ O	-782	139807
$^{17}\mathrm{F}$	1952	128220
18 F	873	137369

Element	Mass excess [keV]	Binding energy [keV]
19 _F	-1487	147801
$^{17}\mathrm{Ne}$	16490	112900
$^{18}\mathrm{Ne}$	5307	132154
$^{19}\mathrm{Ne}$	1751	143781
$^{20}\mathrm{Ne}$	-7042	160645
$^{21}\mathrm{Ne}$	-5732	167406
$^{22}\mathrm{Ne}$	-8024	177770
$^{23}\mathrm{Ne}$	-5154	182971
$^{20}\mathrm{Na}$	6845	145976
$^{21}\mathrm{Na}$	-2184	163076
$^{22}\mathrm{Na}$	-5182	174145
²³ Na	-9529	186564
$^{20}{ m Mg}$	17570	134470
$^{21}{ m Mg}$	10912	149198
$^{22}{ m Mg}$	-397	168578
$^{23}{ m Mg}$	-5473	181725
$^{24}{ m Mg}$	-13933	198257
$^{25}{ m Mg}$	-13193	202535
$^{26}{ m Mg}$	-16214	216681
²² Al	18180	149220
23 Al	6767	168703
²⁴ Al	-55	183596
²⁵ Al	-8916	200528
²⁶ Al	-12210	211894
²⁷ Al	-17197	224952
$^{56}\mathrm{Fe}$	-60601	492254
$\frac{104}{\mathrm{Ru}}$	-88091	893085

Table C.1: List of elements

Bibliography

- [1] Grindlay, J. E. et al. 1976, ApJ, 205, L127
- [2] Belian, R. D., Conner, J. P. & Evans, W. D. 1976, ApJ, 206, L135
- [3] Cornelisse, R., Heise, J., Kuulkers, E., Verbunt, F. & in't Zant, J. J. M. 2000, A&A, 357, L21
- [4] Strohmayer, T. E. 2000, AAS/High Energy Astrophysics Division, 32
- [5] Strohmayer, T. E. & Brown, E. F. 2002, ApJ, 566, 1045
- [6] Kuulkers, E. et al. 2002, A&A, 382, 503
- [7] Wijnands, R. 2001, ApJ, 554, L59
- [8] Strohmayer, T. E. & Markwardt, C. B. 2002, ApJ, 577, 337
- [9] Cornelisse, R., Kuulkers, E., int Zand, J. J. M., Verbunt, F., & Heise, J. 2002, A&A, 382, 174
- [10] Kuulkers, E. 2002, A&A, 383, L5
- [11] Strohmayer, T. & Bildsten, L. 2003 arXiv:astro-ph/0301544v2
- [12] Brown, E. F., Bildsten, L. 1998, ApJ, 496, 915
- [13] Narayan, R. & Heyl, J. S. 2003, ApJ, 599, 419N
- [14] Lewin, W. H. G., van Paradijs, J., & Taam, R. E. 1993,
- [15] Weinberg, N. N. & Bildsten, L. 2007, ApJ, 670, 1291
- [16] Heger, A., Fryer, C. L., Woosley, S. E., Langer, N., Hartmann, D. H. 2003, ApJ, 591, 288
- [17] Haensel, P., Potekhin, A. Y., Yakovlev, D. G. Neutron Stars 1, Equation of State ans Structure, Springer 2006
- [18] Povh, B., Rith, K., Scholz, C., & Zetsche, F., Particles and Nuclei, Springer 2006

- [19] Brown, E. F., & Cumming, A. 2008 in prep.
- [20] Wijnands, R., Nowak, M., Miller, J. M., Homan, J., Wachter, S., & Lewin, W. H. G. 2003, ApJ, 594, 952
- [21] Yakovlev, D., & Urpin, V. 1980, Sov. Astron., 24:3
- [22] Yakovlev, D., & Urpin, V. 1980, Sov. Astron., 24:303
- [23] Potekhin, A. Y., Chabrier, G., Yakovlev, D. G. 1997, A&A, 323, 415
- [24] Salpeter, E. E. 1954, AuJPh, 7, 373
- [25] Narayan, R, & Heyl, J. S. 2003, ApJ, 599, 419
- [26] Woosley, S. et al. 2004, ApJS, 151, 75
- [27] Schatz, H. et al. 2001, Phys. Rev. Lett., 86, 3471
- [28] Hansen, C. J., & van Horn, H. M. 1975, ApJ, 195, 735
- [29] Taam, R. E., & Picklum, R., E. 1978, ApJ, 224, 210
- [30] Narayan, R., & Cooper, R. L. 2007, ApJ, 665, 628
- [31] Fujimoto, M. Y., Hanawa, T., & Miyaji, S. 1981, ApJ, 247, 267
- [32] Shen, K. J., Bildsten, L. 2008, arXiv:0805.2160
- [33] Haensel, P., & Potekhin, A. Y. 2004, A&A, 428, 191
- [34] Pandharipande, V. R.; Ravenhall, D. G. 1989, Nuclear Matter and Heavy Ion Collisions. NATO Advanced Study Institutes Series. Volume B205, 1989, p.103
- [35] Douchin, F., & Haensel, P. 2001, A&A, 380, 151
- [36] Chabrier, G., & Potekhin, A. Y. 1998, Phys. Rev. E, 58, 4941
- [37] Hansen, J. P. 1973, Phys. Rev. A, 8, 3097
- [38] Lamb, D. Q., & Lamb, F. K. 1978, ApJ, 220, 291
- [39] Schatz et al. 1999, ApJ, 524, 1014
- [40] Haensel, P. & Zdunik, J. L. 1990, A&A, 227, 431H

